ANDOR

Spectroscopy Solutions

A Modular Approach

Andor Spectroscopy Product Portfolio

Engineered from the outset with “ease-of-use” in mind, every Andor Spectroscopy system features a combination of market leading detectors and spectral instruments, seamlessly controlled through Andor’s dedicated and intuitive Solis software platform. From configuration of these pre-aligned, pre-calibrated instruments to integration into each unique laboratory set-up, Andor Spectroscopy solutions allow researchers around the world to focus quickly on their own challenges: achieving high quality results and breakthrough discoveries.

Software
Pages 6-7

Solis Spectroscopy and Solis Scanning offer interactive and dedicated graphical interfaces for simultaneous multi-channel or single point detector data acquisition, spectrographs and motorized accessories control.

Cameras
Pages 8-19

Market leading CCDs, InGaAs PDAs, Intensified CCDs and Electron-Multiplying CCDs for VUV to NIR Spectroscopy. Unsurpassed combination of cutting-edge Thermo-Electric cooling, proprietary vacuum technology and ultra-low-noise electronics to extract the very best performance from every Andor camera.

Scanning Accessories
Pages 38-39

Extending Spectroscopy from UV into Short and Long-Wave IR through a range of single point detectors including a PMTs, Si photodiode, InGaAs, PbS, InSb and MCT. Software-controlled data acquisition unit synchronizes simultaneously detectors, monochromators and motorized accessories.

Spectrographs
Pages 20-29

Complete family of rugged, pre-aligned and pre-calibrated Czerny-Turner and echelle spectrographs, for applications ranging from high-resolution UV plasma studies to NIR photoluminescence. The ideal partner for Andor’s high-performance detectors and accessories for ultimate low-light detection.

Accessories
Pages 30-37

From gratings to fibre optics, sample chamber, filter wheel and microscope coupling interfaces, each accessory allows seamless optimization of Andor detection system performance and easy integration into researchers complex experimental setups.

Application and Technical Notes
Pages 40-65

Our experience has enabled us to bring together the latest cutting-edge technology in the fields of sensors, electronics, optics, vacuum technology and software to deliver world-class, market-leading scientific Spectroscopy detection systems.

Andor's experience in manufacturing high-performance Spectroscopy systems spans over 20 years, with thousands of detectors in the field and a proud history of remarkable advances in a wide variety of research areas, truly helping scientists all over the world to "Discover new ways of seeing".

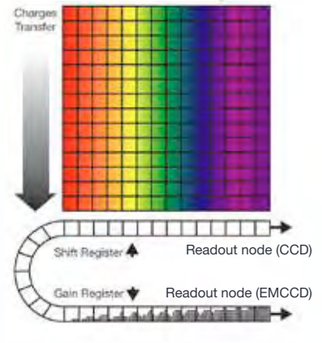

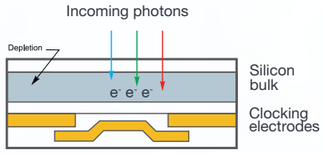

Example of a Back-Illuminated CCD pixel structure

CCD basics

A Charge Coupled Device, or CCD, is a 2D matrix of silicon diode photo-sensors referred to as "pixels". Incident photons with sufficient energy are absorbed in the silicon bulk and liberate an electron which can be stored and detected as part of a readout sequence. Photons with wavelength $\lambda > 1.1\mu m$ do not have enough energy to create a free electron and therefore set the upper detection limit of silicon CCDs.

The probability of detecting a photon at a particular wavelength is known as Quantum Efficiency (QE). QE will vary with depletion depth of the silicon, quality of the CCD structural layers and clocking electrodes "transparency".

At the end of an exposure, the CCD pixel charges are transferred sequentially under a masked area known as the shift register. This serial register connects to an amplifier that digitizes the signal and allows a quantitative readout of the amount of electrons per pixel.

The principal types of high performance CCD-based digital cameras include :

- The Charge-Coupled-Device (CCD)
- The Electron-Multiplying CCD (EMCCD) - with on-chip gain for sensitivity down to single photon
- The Intensified CCD (ICCD) - Image Intensifier provides fast optical shuttering and signal amplification

Ultravac™ – Market-leading vacuum and cooling technology

Cooling sensors reduce thermally generated noise that would otherwise interfere with the useful signal, hence making it a prerequisite for high sensitivity measurements. The sensor must be operated in a vacuum in order to :

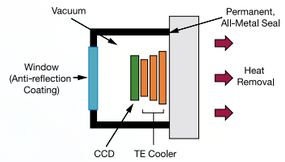

1. Guarantee access to the best cooling performance, hence lowest dark current
2. Increase sensor lifetime by avoiding condensation and sensor degradation

Outgassing is a natural process occurring in any permanent vacuum system, whereby remanent impurities contained in the chamber will be slowly released and potentially affect cooling performance over time. Over 20 years experience in vacuum technology ensures that Andor cameras come with an un-matched warranty on vacuum integrity, guaranteeing cooling performance year after year. Combined with Andor's highly efficient Thermo-Electric cooling interface, temperatures as low as -100ºC will be achieved without the inconvenient use of Liquid Nitrogen (LN_2), see SNR discussion in the technical notes section. Andor's industry-leading vacuum seal design also means that only one window is required in front of the sensor enabling maximum photon throughput, which is especially suited for photon-starved applications.

Making sense of sensitivity – signal-to-noise ratio considerations

A camera Signal-to-Noise Ratio (commonly abbreviated to S/N or SNR) is the true comparison basis between detectors and detector technologies. It takes into account both photon capture capability of the detector and different noise sources along the detection path that can impact on the integrity of the useful signal. The sources of this noise are the following :

- **Readout noise** - inherent sensor electron-to-voltage conversion and amplification noise
- **Thermal noise** - originating from sensor, blackbody radiation (SWIR region) or image intensifier photocathode
- **Photon noise / Shot noise** - statistical incoming photon variation
- **Spurious Charge / Clocking Induced Charge (CIC)** - result of impact ionization during charge transfer

$$Noise_{total} = \sqrt{N_{readout}^2 + F^2.G^2.(N_{darknoise}^2 + N_{photon}^2 + N_{CIC}^2)}$$

CCD sensitivity is shot noise and readout noise limited - typically used at slow digitization speeds
EMCCD sensitivity is shot noise and CIC limited – typically used for photon-starved and ultrafast Spectroscopy
ICCD sensitivity is shot noise and photocathode thermal noise (EBI) limited – typically used for ns time-resolution

Software

"Discover new ways of seeing™" takes its true meaning when the most sensitive Spectroscopy detection solutions on the market combine with Andor's comprehensive software capabilities. From seamless configuration of spectrographs and cameras to actual data acquisition optimization, Andor Solis software and Software Development Kit offer a truly powerful, yet user-friendly modular approach to Spectroscopy.

Solis for Spectroscopy

Modular Raman Spectroscopy, Laser Induced Breakdown Spectroscopy (LIBS) and Plasma diagnostics are only a few examples of applications where Andor Solis Spectroscopy allows researchers to truly focus on their own experimental challenges. With its unique interactive real-time control interface, users can optimize system optical performance through wavelength, gratings and entrance/exit slits selection at the touch of a button, while accessing all key detectors acquisition parameters to optimize the quality of the signal. Solis also features a comprehensive range of acquisition options including ultrafast kinetic series and "Crop mode" operation, simultaneous multi-track recording, photon-counting mode, and time-resolved series capture for lifetime fluorescence studies.

Solis for Scanning

With detection capabilities ranging from UV to the Long Wave IR (LWIR) region through a comprehensive range of single point detectors - including PMTs, PbS and MCT, Solis Scanning offers a dedicated platform for scanning applications. Spectrograph/monochromators, detectors, data acquisition unit, lock-in amplifier / chopper and motorized accessories can all be conveniently synchronised through a series of intuitive interfaces. A single software package features a comprehensive step-by-step experiment building interface for parametring and synchronizing all components of the detection chain. Complex scanning sequences involving multiple gratings, filters and up to 2 monochromators for fluorescence measurements - including a tuneable light source setup - can be seamlessly captured prior to acquisition start and executed without further intervention of the user. Solis Scanning can also handle multiple detectors control and data display for Absorption - Transmission - Reflection Spectroscopy, while offering post-acquisition mathematical data processing ranging from simple ratios and lifetime measurements to fast phenomena analysis.

Software Development Kit (SDK)

Andor SDK features a comprehensive library of camera and spectrograph controls, ideally suited for complex experiments integration including third party hardware control and SDK - i.e. microscope motorized stage or light sources – and user specific data analysis protocols. Available as 32 and 64-bit libraries for Windows (XP, Vista and 7) and Linux, the SDK provides a suite of functions that allow configuration of the data acquisition process in a number of different ways. The dynamic link library can be used with a wide range of programming environments including C/C++, C#, Delphi, VB6, VB.NET, Labview and Matlab.

Spectroscopy cameras

Andor has been taking pride in helping researchers around the world achieve breakthrough discoveries for the last 20 years. By keeping at the forefront of detector technology, Andor is able to offer a range of market leading high-performance, ultra sensitive Spectroscopy detectors. Our CCDs, ICCDs, EMCCDs and InGaAs arrays can operate from the VUV to Near-Infrared spectral regions with a unique combination of high sensitivity (down to single photon in the case of EMCCD technology) and ultrafast acquisition speeds.

CCD

A 2 dimensional silicon-based semiconductor matrix of photo-sensors, with sensitivity ranging from soft X-Ray to NIR (1.1 µm). Spectroscopy CCDs are traditionally a rectangular format with a maximum width of 28 mm and a height up to 13 mm, i.e. matching the focal plane size of the vast majority of high-end spectrographs.

Intensified CCD (ICCD)

Combination of a CCD matrix with a fibre coupled Image Intensifier, which provides optical shuttering capabilities and time-resolution down to the nanosecond regime while also offering a signal amplification up to x1000.

InGaAs

Indium Gallium Arsenide (InGaAs) is a photo-sensitive material used for detection up to 2.2 µm. The typical sensor architecture for Spectroscopy applications is a single row array of up to 25.6 mm.

Electron Multiplying CCD (EMCCD)

Identical architecture to standard CCD sensors, with the addition of an on-chip amplification channel prior to the digitization node, designed to overcome the readout noise limitation of slow-scan CCDs. This revolutionary technology opens the door to ultra-sensitive and ultra-fast Spectroscopy.

Optimum

Applications	Newton	Newton^{EM}	iXon3	iDus	InGaAs	iStar
Absorption - Transmission - Reflection	UV-NIR	UV-Vis	UV-NIR	UV-NIR	NIR-SWIR	UV-Vis
Photoluminescence - Fluorescence	UV-NIR	UV-Vis	UV-NIR	UV-NIR	NIR-SWIR	UV-Vis
Raman (SERS, SORS, CARS, Stimulated)	244-830 nm	244-633 nm	244-830 nm	244-830 nm	1064 nm	244-633 nm
Micro-Raman and Micro-Fluorescence	UV-NIR	UV-Vis	UV-NIR	UV-NIR	NIR-SWIR	UV-Vis
Photon Counting	-	UV-Vis	UV-Vis	-	-	UV-Vis
Single Molecule Spectroscopy	-	UV-Vis	UV-Vis	-	-	UV-Vis
Hyper-Spectral Imaging	-	UV-Vis	UV-Vis	-	-	-
LIBS	-	-	-	-	-	UV-NIR
Plasma Studies	UV-NIR	UV-Vis	UV-NIR	UV-NIR	NIR-SWIR	UV-NIR

Sensor type	Description	
LDC-DD	Back-illuminated, Deep Depletion Low Dark Current CCD with fringe supression	New
BVF	Back-illuminated CCD, VIS optomized with fringe supression	New
BEX2-DD	Back-illuminated, Deep Depletion CCD, Broadband Dual-AR coating with fringe supression	New
BR-DD	Back-Illuminated, Deep Depletion CCD with fringe suppression	
BU	Back-Illuminated CCD, UV-Enhanced, 350 nm optimized	
BU2	Back-Illuminated CCD, UV-Enhanced, 250 nm optimized	
BV	Back-Illuminated CCD, VIS optimized	
FI	Front-Illuminated CCD	
OE	Open-Electrode CCD	
UV	Front-Illuminated CCD with UV coating	
UVB	Back-Illuminated CCD with UV coating	
VP	Virtual Phase CCD (Proprietary technology from Texas Instruments)	

iDus CCD cameras

Workhorse Spectroscopy Cameras

The iDus is Andor's most popular platform for the Spectroscopy research and OEM communities. Boasting sensor QE up to 95%, state-of-the-art Ultravac™, cooling down to -100ºC and a range of 1024 x 127, 1024 x 256 and high resolution 2000 x 256 CCD matrix with UV to NIR optimized options. The iDus series is the camera of choice for everyday Spectroscopy measurements, as well as more advanced, low light detection applications.

Key applications

- Absorption - Transmission - Reflection
- Raman (244, 532, 785 and 833 nm)
- Fluorescence - Luminescence - Photoluminescence
- Plasma studies
- Plasmonics

View our cameras online **www.andor.com**

360° Rotate

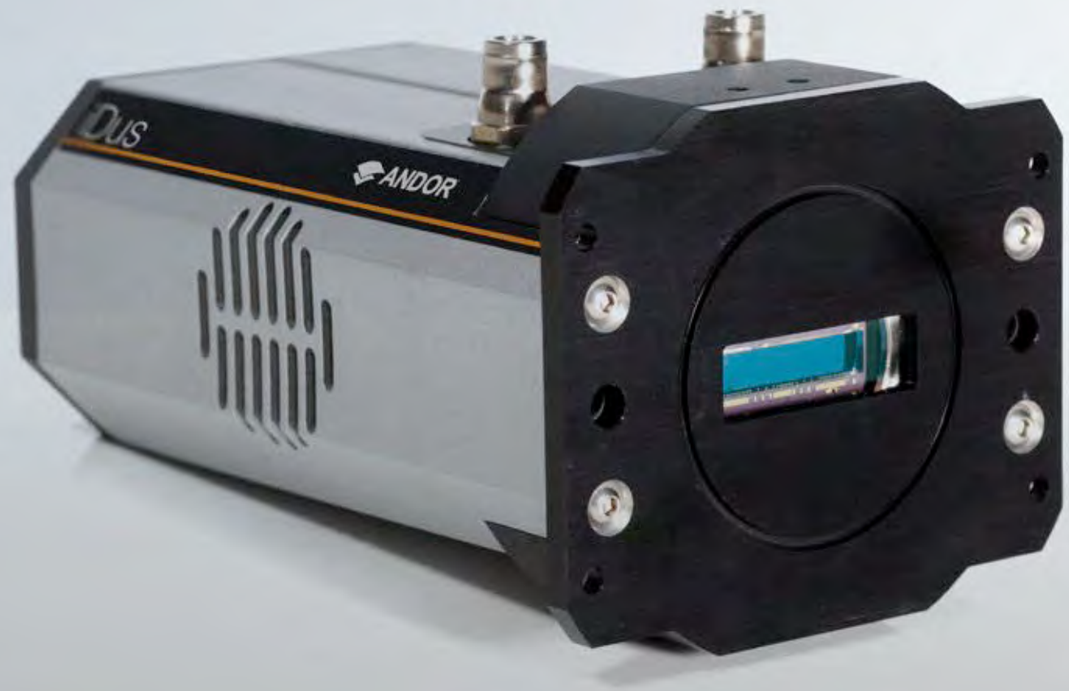

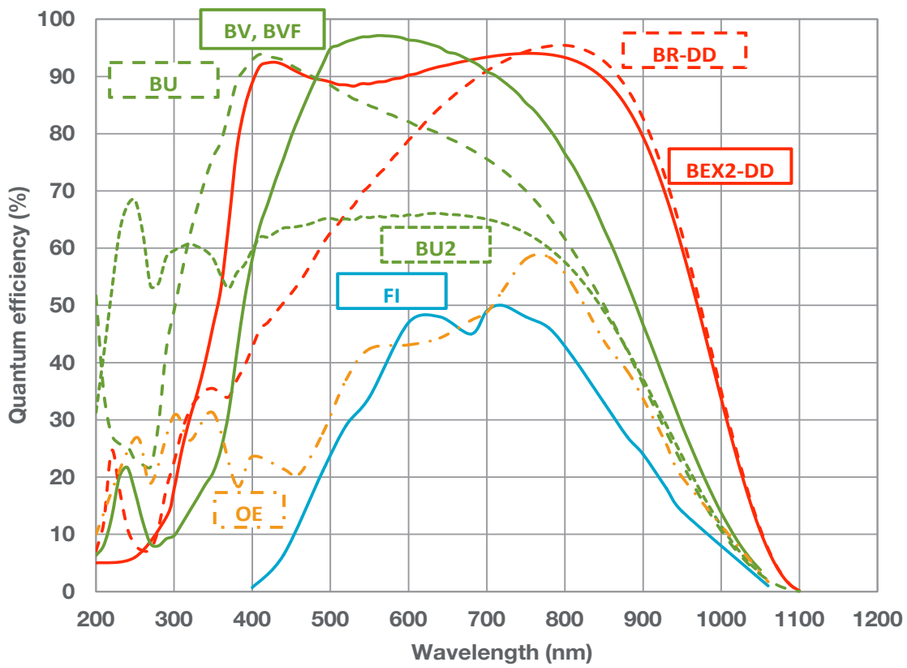

Features

Benefits

Features	Benefits
Peak QE of 95%	High detector sensitivity options both in VIS and NIR regions
TE cooling to -100˚C	Negligible dark current without the inconvenience of LN_2
Ultravac™ – Guaranteed hermetic vacuum seal	Permanent vacuum integrity, critical for deep cooling and best sensor performance
26 or 15 µm pixels	Choice of high dynamic range (401 and 420 models) or high resolution (416 model)
Fringe suppression technology for back-thinned and back illuminated Deep Depletion option	Greatly reduces etalonning effect above 650 nm
Deep-Depletion sensor options	High NIR QE, low etaloning – ideal for NIR Raman or photoluminsecence. Superior broadband detection with Dual-AR technology option (BEX2-DD). Low dark-current (LDC) technology (416 model) - ideal for challenging low light NIR spectroscopy without the need for LN_2 cooling
Simple USB 2.0 connection	User friendly plug-and-play connection directly to the back of the camera

Model	Active pixels (µm)	Pixel size (µm)	Deepest cooling	Sensor options	
DU416	2000 x 256	15 x 15	-95°C	LDC-DD	New
DV416	2000 x 256	15 x 15	-70°C	LDC-DD	New
DU401	1024 x 127	26 x 26	-100˚C	FI, BVF	
DU401-BR-DD	1024 x 128	26 x 26	-100˚C	BR-DD	
DU420	1024 x 255	26 x 26	-100˚C	BU, BU2, BV, OE, BVF	
DU420-Bx-DD	1024 x 256	26 x 26	-100˚C	BR-DD, BEX2-DD	
DV401	1024 x 127	26 x 26	-70˚C	FI, BVF	
DV420	1024 x 255	26 x 26	-70˚C	BU, BU2, BV, OE, BVF	

See Page 62 for technical note – LN_2 vs TE cooling for BR-DD sensors

iDus InGaAs

Andor's iDus InGaAs detector array for Spectroscopy

Andor iDus InGaAs 1.7 and 2.2 array series provide the most compact and optimized research-grade platform for Spectroscopy applications up to either 1.7 or 2.2 µm. The Thermo-Electrically cooled, in-vacuum sensors reach cooling temperatures of -90ºC where the best signal-to-noise ratio can be achieved for the majority of the applications in this spectral region. Beyond this cooling point blackbody radiation from any elements facing the sensor will dominate the dark signal, and since Quantum Efficiency will be impacted with decreasing cooling temperature, TE cooling will allow access to optimum SNR performance.

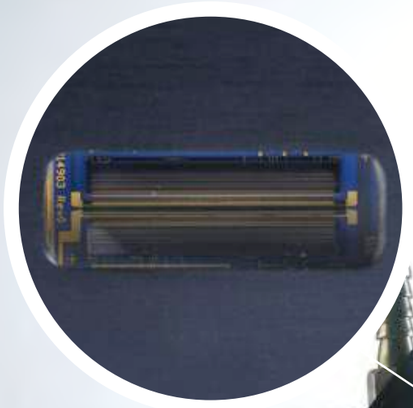

See page 42 for Photoluminescence application note

See page 62 for technical note – LN_2 vs TE cooling for InGaAs sensors

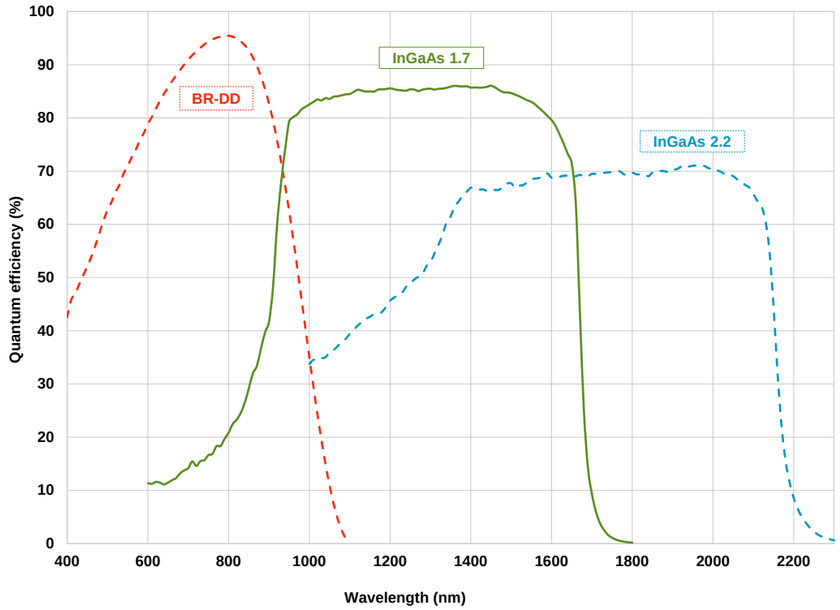

Features	Benefits
High Quantum Efficiency Peak QE >80% for 1.7 µm cut-off Peak QE >70% for 2.2 µm cut-off	Maximum sensitivity in the NIR
Typically attainable TE cooling to -90°C	Minimise dark current efficiently without the inconvenience of LN_2
UltraVac™	Ensures best sensor performance and protection in time
Minimum exposure time of 1.4 µsec	Allows study of fast transient phenomena
25 µm pixel width option	Optimized for high dynamic range and high resolution
25.6 mm wide arrays options	Optimized for Czerny-Turner spectrograph focal plane size
Software selectable output amplifiers	Choice of High Dynamic Range (HDR) or High Sensitivity (HS)
Simple opto-mechanical coupling interface	Readily integrate with Andor Shamrock spectrograph series
Simple USB 2.0 connection	User-friendly plug-and-play connection directly to the back of the camera

Model	Array size (mm)	Array size (pixels)	Pixel size (W x H, µm)	Upper cut-off wavelength (µm)
DU490A-1.7	12.8	512 x 1	25 x 500	1.7
DU490A-2.2	12.8	512 x 1	25 x 250	2.2
DU491A-1.7	25.6	1024 x 1	25 x 500	1.7
DU491A-2.2	25.6	1024 x 1	25 x 250	2.2
DU492A-1.7	25.6	512 x 1	50 x 500	1.7
DU492A-2.2	25.6	512 x 1	50 x 250	2.2

Key applications

- NIR and SWIR Absorption - Transmission - Reflection
- Raman (1064 nm)
- NIR Photoluminescence

Newton CCD

The World's fastest Spectroscopy CCD

When it comes to the best in Spectroscopy detection, the Newton CCD cameras always come first. With a wide range of sensors boasting up to 95% QE, pixels as small as 13.5 µm and the Andor state-of-the-art Ultravac™ platform for everlasting cooling performance to -100˚C, the Newton series offers no compromise when it comes to high sensitivity. Its low-noise, multi-MHz electronics platform enables spectral collection faster than 1600 spectra per second, ideal for transient phenomona studies.

Key applications

- Absorption - Transmission - Reflection
- Raman (244, 532, 785 and 833 nm)
- Fluorescence - Luminescence - Photoluminescence
- Plasma studies
- Plasmonics
- Fast Transient phenomena study

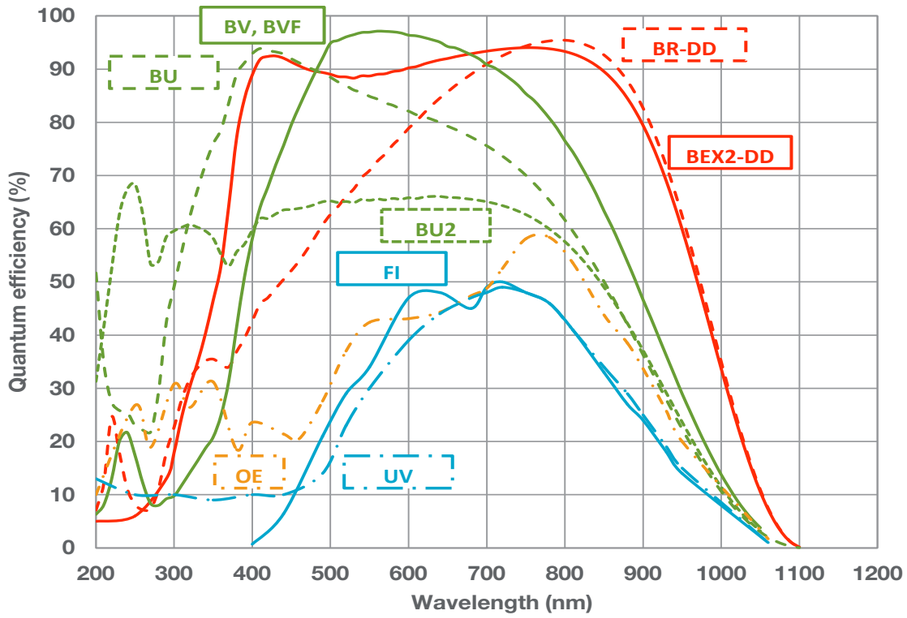

Features

Features	Benefits
Multi-megahertz readout	High repetition rates achievable with low noise electronics - ideal for transient phenomona study
TE cooling to -100°C	Negligible dark current without the inconvenience of LN_2
UltraVac™ - guaranteed hermetic vacuum seal technology	Permanent vacuum integrity, critical for deep cooling and best sensor performance access
Down to 13.5 x 13.5 µm pixel size	Optimized pixel size for achievement of high resolution Spectroscopy
Crop mode operation	Achieve the highest possible spectral rates of over 1,600 spectra per second
Deep-depletion sensor options	High NIR QE, virtually etalon-free - ideal for NIR Raman. Superior broadband detection with Dual-AR technology option (BEX2-DD)
Software-selectable output amplifiers (DU940)	Choice of High Dynamic Range (HDR) or High Sensitivity (HS)
Simple opto-mechanical coupling interface	Readily integrate with Andor Shamrock spectrograph series
Simple USB 2.0 connection	User friendly plug-and-play connection directly to the back of the camera

Model	Active pixels (µm)	Pixel size (µm)	Sensor options	
DU920	1024 x 255	26 x 26	BU, BU2, BV, OE, BVF	New
DU920-Bx-DD	1024 x 256	26 x 26	BR-DD, BEX2-DD	
DU940	2048 x 512	13.5 x 13.5	BU, BU2, BV, FI, UV	

iXon and Newton^{EM}

Speed and Sensitivity with NO compromise

From the pioneers of EMCCD technology the newly released iXon Ultra and Newton^{EM} series have brought low-light Spectroscopy to a new level of performance. Featuring Andor's market leading TE cooling to -100ºC, Ultravac^{TM} vacuum technology, Quantum Efficiency up to 95% and sub-electron read noise with on-chip Electron-Multiplying amplification, Newton^{EM} and iXon cameras offer the absolute combination of sensitivity and acquisition speed.

Professor Michael Morris
Professor of Chemistry
University of Michigan

"In our lab the Andor Newton^{EM} EMCCD has enabled millisecond Raman Spectroscopy and Hyper-spectral Raman imaging in times as short as a minute or two. And the 1600 x 400 format is just right for Spectroscopy".

Key applications

- Absorption - Transmission - Reflection
- Raman (244, 532, 633 nm)
- Raman (785 and 833 nm – VP and FI only)
- Fluorescence - Luminescence
- Plasma studies
- Photon counting
- Single molecule Spectroscopy

See pages 44 and 46 for Raman EMCCD application notes

See page 64 for EMCCD for Spectroscopy technical note

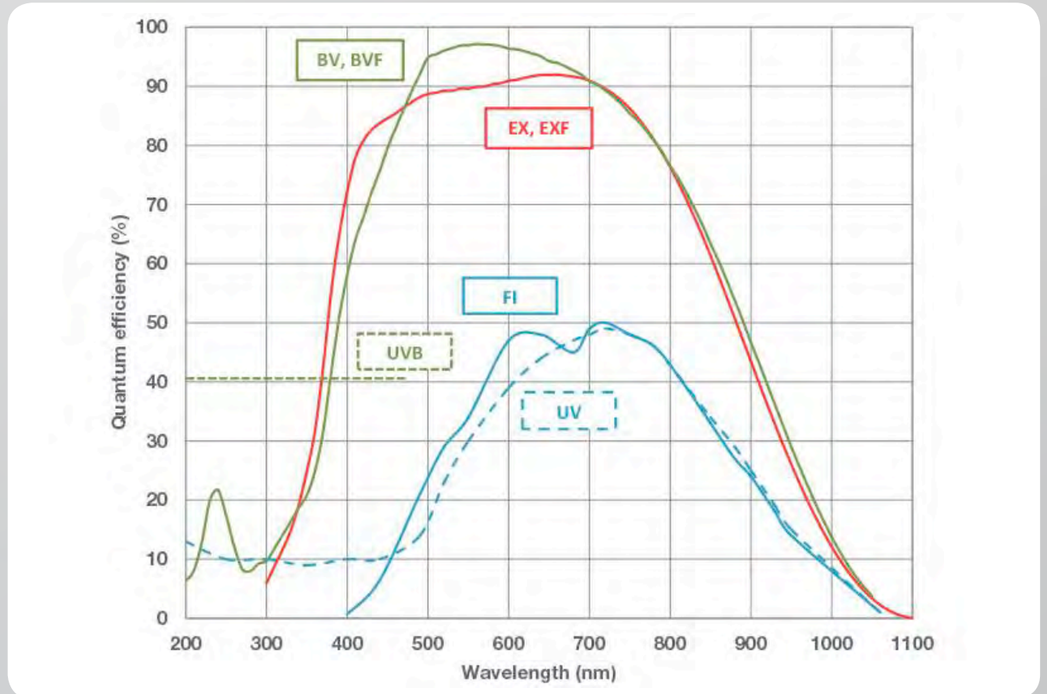

Features

Benefits

Features	Benefits
<1 e$^-$ readout noise and up to 95% QE	'Silent' noise floor, perfectly complements high QE performance for extremely low-light detection
Industry benchmark for fast frame and spectral rate	Full vertical binning up to 650 spectra per second or imaging frame rate up to 35 full-frames per second
Cropped mode option	Boosts spectral rate of Newton cameras up to 1515 spectra per second
Ultravac^{TM} technology and TE cooling down to -100ºC	Permanent vacuum integrity, critical for deep cooling and best sensor performance access
True 16-bits digitization	Lowest internal noise and highest linearity from scientific-grade A/D converters
Software-selectable output amplifiers	Choice of High Sensitivity (low light applications) or Electron Multiplication (ultra-low light applications down to single photon)
Spectroscopy and Imaging sensor formats available	25 mm wide option for maximum spectral information collection, or up to 13 mm tall option for larger vertical field of view, ideally suited for micro-Spectroscopy. Fringe supression options available for minimizing optical etaloning above 650 nm
Seamless integration with Andor spectrographs	Simple opto-mechanical coupling to Andor Shamrock spectrograph series, with all-integrated dedicated software control

Model	Active pixel matrix	Pixel size (µm)	Fastest spectral rate *	Data transfer interface	Sensor options
Newton 970	1600 X 200	16 X 16	1,515 sps	USB 2.0	BV, FI, UV, UVB, BVF
Newton 971	1600 X 400	16 X 16	1,515 sps	USB 2.0	BV, FI, UV, UVB
iXon3 888	1024 X 1024	13 X 13	4,170 sps	PCI	BV, UVB, EXF, EX
iXon Ultra 897	512 X 512	16 X 16	9,921 sps	USB 2.0	BV, UVB, EXF, EX, BVF

* sps = spectra per second

New iStar ICCD

Industry gold standard for high-resolution, high-speed nanosecond time-resolved spectroscopy.

With over 16 years of Excellence in the development of world-class, fast-gated intensified CCD cameras, Andor's iStar detectors are at the forefront of rapid, nanosecond time-resolved Spectroscopy. Launched in 2011, Andor's New iStar USB 2.0 platform extracts the very best from CCD sensor and gated image intensifier technologies, achieving a superior combination of rapid acquisitions rates and exceptional sensitivity down to single photon. The New iStar is the most compact research-grade ICCD on the market, with a a unique software-controlled, ultra-low-jitter on-board Digital Delay Generator (DDG™) and high-voltage, high-speed gating electronics for superior time resolution, shuttering accuracy and ultra-precise synchronisation.

Professor JJ Laserna
Professor of Chemistry
University of Malaga

"The Andor iStar ICCD detectors played a vital role in allowing us to develop this new mobile standoff detection system since their sensitivity allowed us to work with exceedingly low light levels. Furthermore, their refresh rates meant we could analyze spectral information at rates in excess of 10 Hz and, therefore, perform simultaneous Raman and LIBS Spectroscopy in real time".

Key applications

- Laser Induced Breakdown Spectroscopy (LIBS)
- Time-Resolved Raman and Resonance Raman Spectroscopy (TR^3)
- Time-resolved fluorescence - luminescence
- Plasma studies
- Laser flash photolysis
- Single molecule spectroscopy

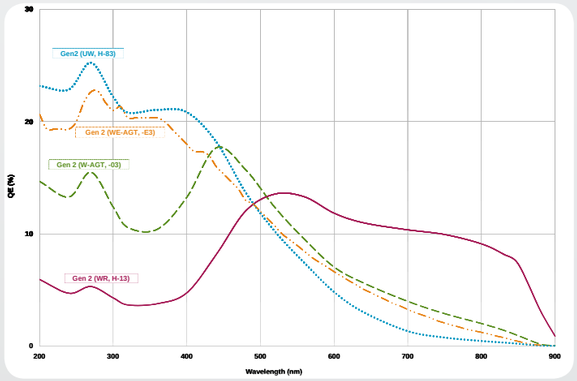

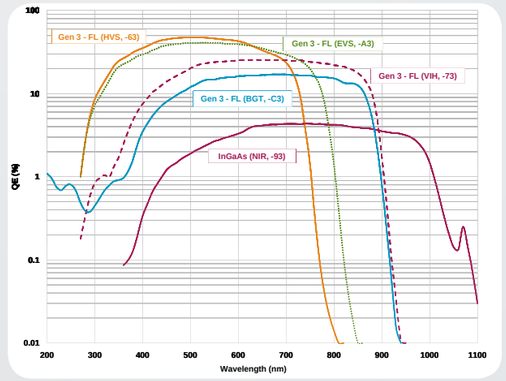

Features	Benefits
USB 2.0 connectivity	Industry-standard plug-and-play, lockable and rugged interface Seamless multi-camera control from single PC or laptop
5 MHz readout platform	Rapid spectral rates for superior dynamic phenomena characterization
Comprehensive binning options - Crop and Fast Kinetic mode	Fully software-customizable binning sequences for highest spectral and image rates. Greater than 3,400 spectra/s continuous rates, up to 29,000 spectra/s in burst mode
High-resolution sensors and image intensifiers	Sharpest images and spectrum definition, 100% fill factor for maximum signal collection efficiency
High QE Gen 2 and 3 image intensifiers	Highest intensifier resolution with QE > 50% and sensitivity up to 1.1 µm
True optical gating < 2 ns	Billionth of a second time-resolution for accurate transient phenomena study
Low jitter, on-board digital delay generator	Highest gating timing accuracy with lowest propagation delay
Insertion delay as low as 19.1 ns	Lowest delay from signal generation to photocathode triggering
Comprehensive triggering interface	Software-controlled 3x triggering outputs with 10 ps setup accuracy
Intelligate™	Intelligent and accurate MCP gating for better than $1:10^8$ shuttering efficiency in the UV
500 kHz sustained photocathode gating	Maximises signal-to-noise in high repetition rate laser-based applications
Photocathode EBI minimization	Dry gas purge interface for further efficient EBI reduction
TE-cooling to -40ºC	Efficient minimization of CCD dark current and pixel blemishes
Real-time control interface	On-the-fly software control of intensifier gain, gating and 3x outputs trigger parameters for real-time detection optimization

Photo-cathode	Type	Coverage	Peak QE (typical)	Minimum gating speed
-03	Gen 2	180-850 nm	18%	< 2 ns
-04	Gen 2	180-850 nm	18%	< 2 ns
-05	Gen 2	120-850 nm	16%	< 5 ns
-13	Gen 2	180-920 nm	13.5%	< 50 ns
-63	Gen 3	280-760 nm	48%	< 2 ns
-73	Gen 3	280-910 nm	26%	< 2 ns
-83	Gen 2	180-850 nm	25%	< 100 ns
-93	Gen 3	380-1,100 nm	4%	< 3 ns
-A3	Gen 3	280-810 nm	40%	< 2 ns
-C3	Gen 3	< 200-910 nm	17%	< 2 ns
-E3	Gen 2	180-850 nm	22%	< 2 ns

Models	Active pixel matrix	Effective pixel size (µm)	Image intensifier choice [fibre optic taper]
DH320T (USB 2.0)	1024 x 256	26 x 26	Ø18 mm [1:1] Ø25 mm [1:1]
DH334T (USB 2.0)	1024 x 1024	13 x 13	Ø18 mm [1:1] Ø25 mm [1.5:1]
DH340T (USB 2.0)	2048 x 512	13.5 x 13.5	Ø18 mm [1:1] Ø25 mm [1:1]

See page 50 for stand-off LIBS application note

Spectrographs

Andor technical know-how extends far beyond market-leading performance detectors with a comprehensive range of high-end Spectrographs. At the heart of this portfolio is the Shamrock family, which offers ultimate flexibility and performance with its “out-of-the-box”, pre-aligned and pre-calibrated approach and seamless combination with Andor’s highly sensitive Spectroscopy cameras. The Mechelle 5000 is Andor’s dedicated detection solution for LIBS, offering a unique combination of 750 nm band-pass with high optical resolution in one single acquisition.

Shamrock 163

Rugged, compact 163 mm focal length manual spectrograph, highly configurable for general, everyday lab Spectroscopy.

Shamrock 303i

Laboratory workhorse platform with plug-and-play USB interface, fully motorized grating turret, slits and filter wheel and imaging-optimized optics for multi-track spectral acquisition.

Shamrock 500i

Ideal combination of high spectral resolution, imaging capabilities for multi-track acquisitions and monochromator capabilities with single point detector use for detection up to 12 µm. With the convenience of a USB controlled, fully motorized platform and accessory range.

Shamrock 750

Delivers the highest spectral resolution of the Shamrock range while also featuring monochromator capabilities and plug-and-play, fully motorized interface.

Holospec F/1.8

High throughput spectrograph with superb high-density multi-track spectroscopy capabilities. Robust and compact design based on low stray-light transmission virtual phase holographic (VPH) grating.

Mechelle 5000

Patented optical echelle design with band-pass ranging from 200 nm to 975 nm and resolution power λ/Δλ of 5000 across the full wavelength range, all accessible in a single acquisition without the need for moving components.

Optimum

Applications	Shamrock 163	Shamrock 303i	Shamrock 500i	Shamrock 750	Holospec F/1.8 (New)	Mechelle 5000
Absorption - Transmission - Reflection	✓	✓	✓	✓	✓	
Photoluminescence - Fluorescence	✓	✓	✓	✓	✓	
Raman (SERS, SORS, CARS, Stimulated)	✓	✓	✓	✓	✓	
Micro-Raman and Micro-Fluorescence	✓	✓	✓	✓	✓	
Photon Counting	✓	✓	✓	✓	✓	
Single Molecule Spectroscopy	✓	✓	✓	✓	✓	
LIBS	✓	✓	✓	✓	✓	✓
Plasma Studies	✓	✓	✓	✓	✓	✓
Multi-track Spectroscopy	✓	✓	✓	✓	✓	

Shamrock 163

Versatile compact benchtop spectrograph

The Shamrock 163 is the most compact research-grade Czerny-Turner spectrograph on the market. Its 163 mm focal length, high F/3.6 aperture and wide range of seamlessly interchangeable gratings, slits and light coupling accessories make it the ideal tool for general benchtop Spectroscopy measurements.

Key applications

- Absorption - Transmission - Reflection
- Fluorescence - Luminescence
- Micro-Fluorescence
- Photon counting
- Single molecule Spectroscopy
- Plasma studies
- Radiometry

See page 33 for accessory tree

Resolution calculator
andor.com/calculators

Features	Benefits
Compact and rugged design with horizontal and vertical mounting positions	Portability and ease of integration
Imaging-configurable platform	Lens-based accessories enable multi-track Spectroscopy
Wide range of interchangeable gratings for optimization of wavelength range and resolution	Simple precision locking mechanism for seamless upgradability
Variety of fixed slits for optimization of resolution	Interchangeable laser-cut precision slits from 10 to 200 µm
Large choice of light coupling interfaces	Includes fibre-optics and C-mount microscope couplers
Calibrated micrometer drive for wavelength tuning	Simple and rapid wavelength adjustment

Spectrograph specifications	
Aperture ratio (F/#)	F/3.6
Focal length (mm)	163
Reciprocal dispersion	4.22 nm/mm
Resolution	0.17 nm†
Band pass	117 nm†
Mechanical range	0 - 1401 nm†
Gratings	Single, interchangeable
Slit sizes	Fixed: 10, 25, 50, 75, 100, 200 µm Adjustable (Manual): 10 µm to 3 mm
Size L x W x H	198 x 216 x 96 mm 7.8 x 8.5 x 3.8 in.
Weight kg [lb]	3.5 [7.71]

† = Nominal values using 1200 l/mm grating, 13.5 µm pixel and 27.6 mm wide sensor, 500 nm central wavelength.

Shamrock 303i, 500i and 750

Research grade high performance spectrographs

The Shamrock 303i, 500i and 750 imaging spectrographs are research-grade, high performance and rugged platforms designed for working with demanding low-light applications, but equally suited to routine measurements. The Shamrock series boasts a range of highly versatile accessories and are seamlessly configurable.

These instruments can be integrated with Andor's world-class range of CCDs, Electron-Multiplying CCDs and Intensified CCDs to offer versatile, yet the most sensitive modular solutions on the market. Andor Solis software offers the most user-friendly and state-of-the-art real-time control of detectors, spectrograph and motorized accessories at the touch of a button.

Features	Benefits
Pre-aligned, pre-calibrated detector and spectrograph systems	Motorized, individually factory-calibrated systems – out of the box operation and seamless integration to experimental set-ups
Image astigmatism correction with toroidal optics (303i and 500i)	Maximum light throughput and optimized multi-track capabilities
USB 2.0 interface	"Plug and play" connectivity, ideal for laptop operation alongside multi USB camera control
Triple exchangeable grating turret	Interchangeable in the field
Double detector outputs	For extended wavelength coverage when combining Andor UV-VIS CCD and InGaAs cameras
Wide range of accessories available	The ultimate in modular set-up and in-field upgradability, including: • Motorized slits and filter wheel • Microscope interfaces • Shutters • Fibre-optic and lens couplers • Multi-way fibre-optic bundles • Light sources and optics
Monochromator capabilities (500i and 750)	Extract best optical resolution while allowing use of single point detectors with sensitivity up to 12 µm
Gold and silver optics coating options	Most efficient for NIR detection when used in conjunction with Andor InGaAs cameras and single point detectors

Resolution calculator
andor.com/calculators

See page 32 for accessory tree

Key applications

- Absorption - Transmission - Reflection (UV-NIR and SWIR)
- Raman (244, 532, 785, 833 and 1064 nm)
- Fluorescence - Luminescence (UV-NIR and SWIR)
- Micro-Raman and Micro-Fluorescence
- Photon counting
- Single molecule Spectroscopy
- Plasma studies
- Laser Induced Breakdown Spectroscopy (LIBS)

Spectrograph specifications comparison*	303i	500i	750
Aperture (F/#)	F/4	F/6.5	F/9.8
Focal length (mm)	303	500	750
Reciprocal dispersion (nm/mm)	2.41	1.44	1.01
Wavelength resolution (nm)	0.10	0.06	0.04
Bandpass (nm)	67	40	28
Multi-track capability	Y	Y	Y

* = Specifications given for a 1200 l/mm grating at 500 nm, 10 µm slit and 13.5 µm pixel size, 27.6 mm wide CCD ; resolution figures assume FWHM of 5x 13.5 µm pixels.

Holospec F/1.8 and F/1.8i

New

On-axis high throughput imaging spectrograph

The Andor Holospec spectrograph series offers a combination of very high light collection efficiency, low stray light and superb high-density multi-track spectroscopy capabilities. It provides a perfect match to Andor's low-noise CCD, EMCCD and ICCDs detectors, offering the most sensitive and versatile detection solution on the market for Visible or Near-Infrared spectroscopy.

This instrument is the ideal platform for collecting more light and achieving better signal-to-noise ratio faster, which is critical for intrinsically photon-starved experiments, time-constraint / transient low-light applications and setups where samples can degrade rapidly with over-exposure to the excitation source.

Its rugged and compact design makes it an ideal tool for challenging industrial or in-the-field applications, while still offering research-grade performance suitable for academic research.

Resolution calculator
andor.com/calculators

Features	Benefits
High collection efficiency ultrafast F/1.8 aperture	Up to 6.5 times better light collection efficiency than traditional 1/3rd m Czerny-Turner designs 100% light collection from NA=0.22 fibre optics
On-axis imaging-corrected design	Superb optical aberration correction across a large focal plane for superior spatial resolution and high density, low crosstalk multi-track (multi-fibres) acquisitions Gather more photons per pixel for superior signal-to-noise ratio
High throughput optical design	High transmission volume phase holographic (VPH) gratings with state-of-the art optics - maximum optical efficiency for visible or near-infrared range
Low scattered light	'Smooth' sinusoidal refractive index VPH gratings profile greatly minimises stray light - maximises detection dynamic range and signal-to-noise
Compact and rugged design	Pre-aligned and pre-calibrated, out-of-the-box operation, excellent thermal stability and easily transportable
Easily interchangeable accessories	'Snap-in' accessories, including precision slits and pre-aligned grating assemblies
Specialized Raman grating options	Optimized for Stokes/Anti-Stokes, Low-frequency or High frequency Stokes operation, 514.5 to 830 nm laser options
Optional integrated Rayleigh filtering unit	Fully-enclosed SuperNotch Plus Kaiser filter compartment with user-friendly external adjustment

Key Applications

- ✓ Raman, Luminescence and Plasmonics micro-spectroscopy mapping - e.g. Bio-samples, carbon nanostructures, light harvesting complex or organic light-emitting diode (OLEDs)
- ✓ Photoluminescence - e.g. Quantum Dots
- ✓ Cathodoluminescence
- ✓ Standoff chemical detection - e.g. explosive or chemical warfare
- ✓ Microfluidics - e.g. flow cytometry
- ✓ On-line process control
- ✓ Real-time medical diagnosis - e.g. cancer screening

Resolution and Bandpass

	F/1.8(i) VIS		F/1.8(i) NIR	
Resolution (nm)*1	0.07*3	0.17*4	0.1*5	0.3*6
Bandpass (nm)*2	32*3	83*4	4.7*5	161*6

*1 With 50 µm input slit and 13.5µm pixel CCD e.g. Newton DU940
*2 With 27.6 mm wide CCD e.g. Newton DU940
*3 With high dispersion "532 nm Stokes / Anti-Stokes" grating
*4 With "532 nm low frequency" grating
*5 With high dispersion "785 nm Stokes / Anti-Stokes" grating
*6 With "785 nm low frequency" grating

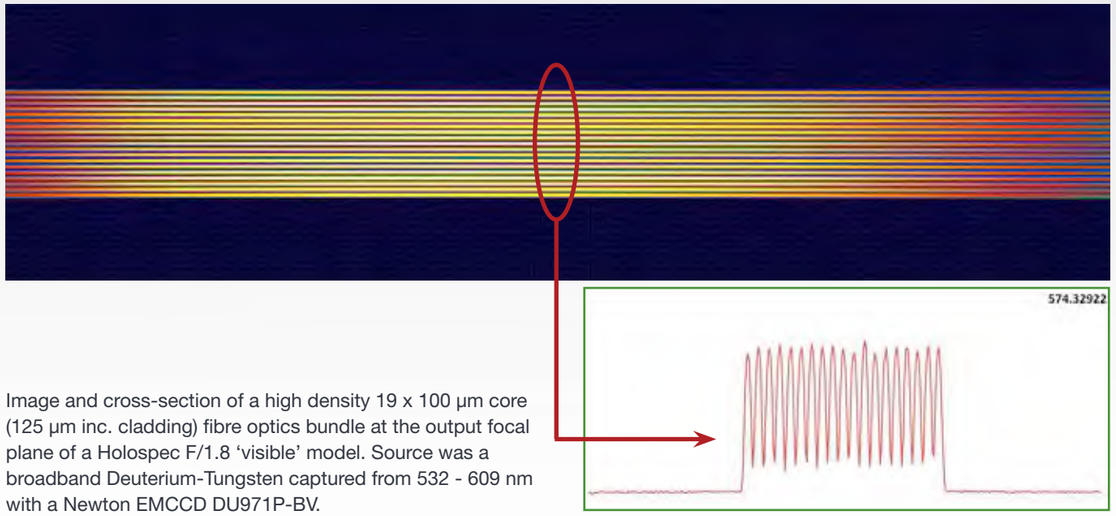

Image and cross-section of a high density 19 x 100 µm core (125 µm inc. cladding) fibre optics bundle at the output focal plane of a Holospec F/1.8 'visible' model. Source was a broadband Deuterium-Tungsten captured from 532 - 609 nm with a Newton EMCCD DU971P-BV.

Mechelle 5000

High band pass echelle spectrograph

Andor's Mechelle 5000 spectrograph has been designed to provide simultaneous recording of a wide wavelength range (200 - 975 nm) in one acquisition. It has no moving components and is available in a pre-aligned detector/spectrograph format.
Based on the echelle grating principle, its patented optical design provides extremely low crosstalk and maximum resolution compared with other spectrographs. It is designed to operate with both Andor's iKon CCD camera and the New iStar DH334T intensified camera in applications such as LIBS and plasma studies.

Key applications

- Laser Induced Breakdown Spectroscopy (LIBS)
- Plasma studies

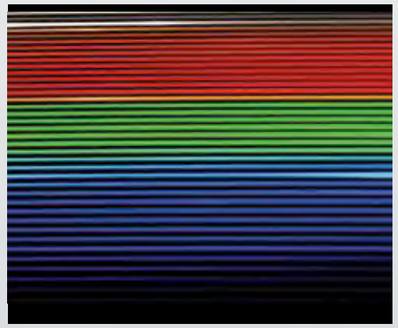

Echellogramme

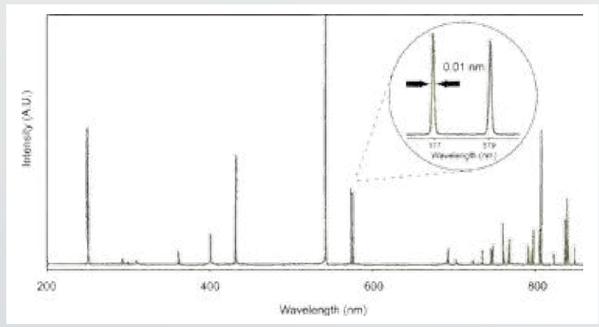

Example of Mercury-Argon spectrum

Features	Benefits
Compact and robust design with no moving components	Ideal for non-lab based applications
Patented optical design	Ensures maximum resolution and extremely low cross-talk
Auto-temperature correction	Corrects for the variation of prisms optical refractive index with temperature
N_2 purged	Enables maximum throughput in the UV region
Pre-aligned detector/spectrograph solution	Enables fast and efficient experimental set-up
Low F/number	Highly efficient light collection
Wide range of accessories available	Including fibre optics, slits, aiming laser, collector/collimator and calibration lamps
Peak labelling with NIST table	Easy tagging of known atomic species at the press of a button

View user publications at
andor.com/publications

Spectrograph specifications	
Wavelength range (nm)	200 - 975
Focal length (mm)	195
Aperture	F/7
Spectral resolution (λ/Δλ) (corresponding to 3 pixels FWHM)	6,000
Wavelength accuracy	Better than ± 0.05 nm
Optical adjacent order cross talk	Better than 1 x 10^{-2}
Stray light	Better than 1.5 x 10^{-4}
Horizontal magnification	0.81
Vertical magnification	1.66

Accessories and systems

“Modularity” is Andor’s ethos when it comes to Spectroscopy systems, because every researcher’s requirements are unique. This translates into the need for an extensive range of state-of-the-art accessories, from light collection to signal analysis and detection. Andor combines over 20 years of expertise in the fields of optics, mechanics and electronics, from designing complex interfaces to extract the very best of its market leading detectors and spectrographs, to working alongside key suppliers worldwide.

The result is Andor’s ability to offer a comprehensive range of high performance dedicated or extremely versatile accessories, ranging from multi-cord fibre optics to sample chamber, light sources, gratings, slits and third party instruments interfaces including microscope and VUV monochromators.

Spectral information tailoring

Selection of low and high density gratings with blazing from UV to NIR, interchangeable fixed, manual and motorized slits, mechanical shutters and filter wheel that accommodate neutral density, Raman edge and long/short pass types.

Signal input coupling interfaces

Range of opto-mechanical couplers including fibre optics X-Y adjusters, F/number matchers, sample chamber and UV to NIR-optimized lenses. Andor’s portfolio for modular Micro-Spectroscopy includes C-mount compatible flanges, wide-aperture slit, modular cage systems and a range of microscope feet for optical height matching.

Fibre optic

Multi-leg fibre ferrules “round-to-line” configurations, for maximum light collection along spectrograph entrance slit and multi-channels simultaneous acquisition with imaging-optimized spectral instruments.

Spectrograph/monochromator accessories

Family of single point detectors used in conjunction with Andor Shamrock 500i and 750 for acquisition from UV with PMTs and silicon photodiode to LWIR (up to 12 µm) region with InSb and MCT sensors.

Light sources

Spectral calibration lamps including “pen-ray” style Mercury, Argon, Neon or Xenon lamps, and Deuterium and Xenon arc lamps for radiometric calibration or absorption measurements.

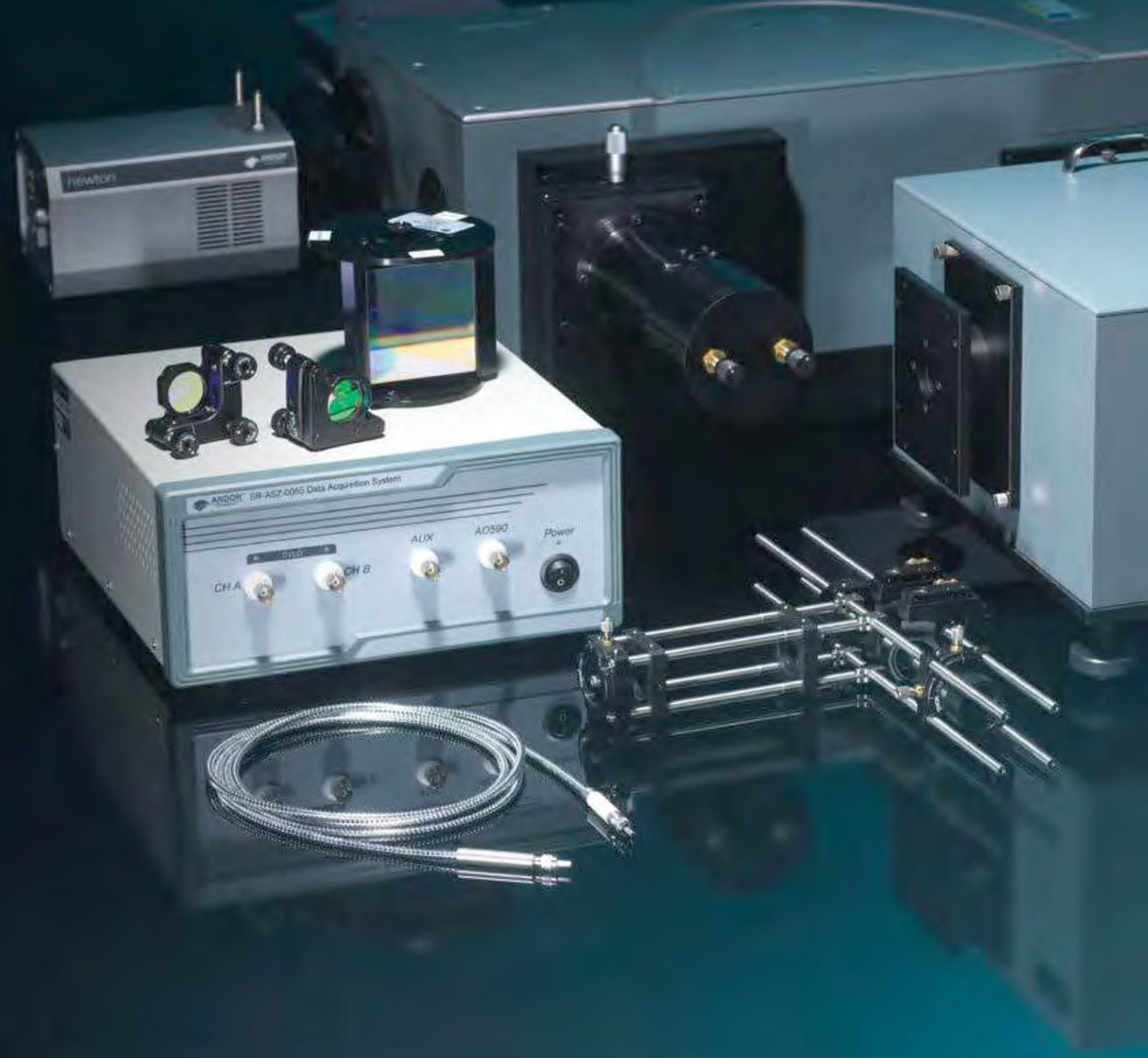

See page 32 for accessory trees

See page 33 for grating selection

See page 34 for fibre optics

See page 36 for Microspectroscopy

Spectrograph accessories configurations

Access to an unlimited range of detection system configurations is the basis of Andor's modular approach to Spectroscopy. That is why Andor is continuously and dynamically expanding its range of field-upgradable accessories to meet the ever-growing demand from researchers. This now includes enhanced options for combining Microscopy and Spectroscopy.

Looking for light coupling interfaces to Andor spectrographs? Have an instant view of all standard accessories and just follow the configuration trees for compatibility check.

Can't see exactly what you are looking for? Want a grating with different groove density or different blaze angle, FC connection instead of SMA or custom light coupling between microscope an spectrograph? Andor's experienced and dedicated Customer Special Request (CSR) team will be eager to discuss your specific needs.

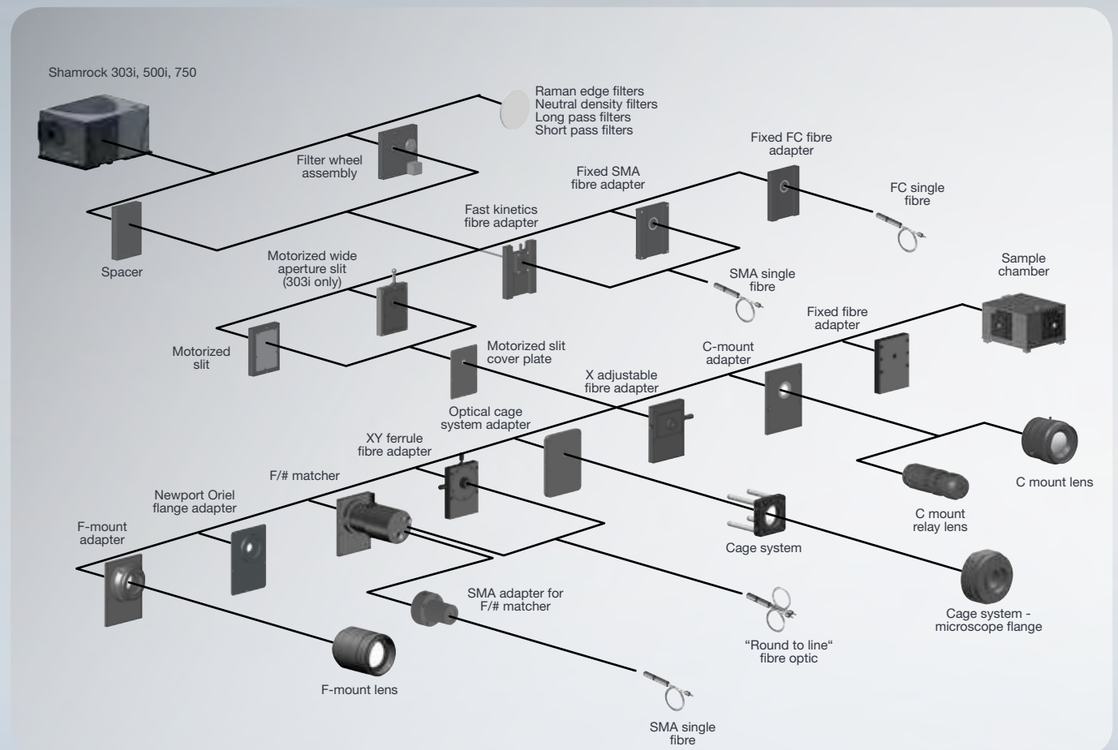

Shamrock 303i, 500i and 750 accessory tree overview

Specification sheets
andor.com/spectroscopy

Resolution calculator
andor.com/calculators

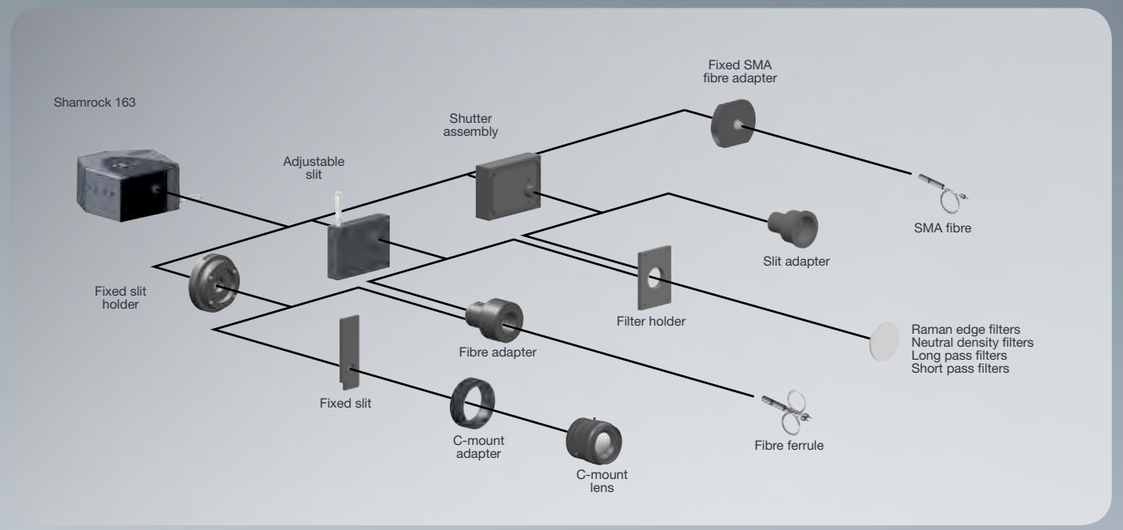

Shamrock 163 accessory tree overview

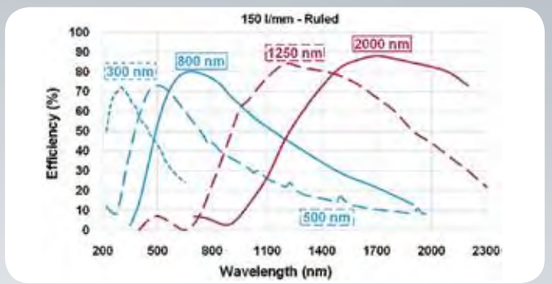

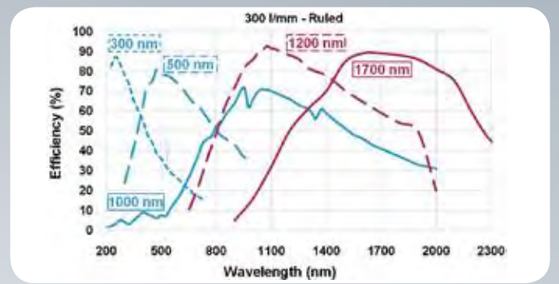

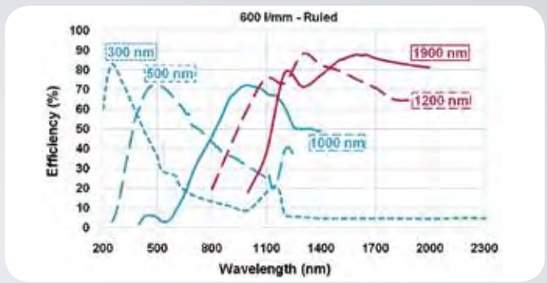

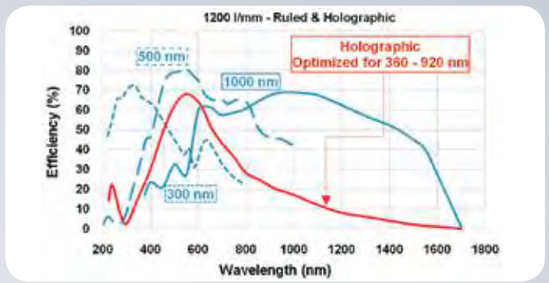

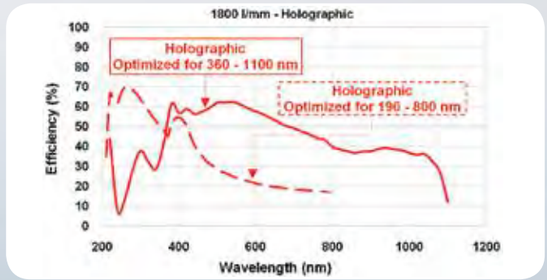

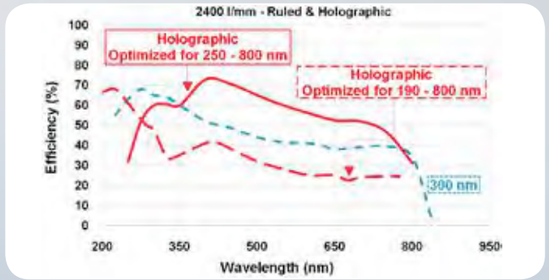

Have you found what you are looking for?

Andor offers a large variety of additional grating options, i.e. groove density and blaze. Please contact your local representative to discuss your specific needs.

Fibre optics solutions

Fibre optic is one of the most convenient ways to collect and transport light from an experimental set-up to a spectrograph-based detection solution. Andor's series of "round-to-line", multi-core fibre optic bundles maximises the signal collection by positioning the multiple cores alongside the spectrograph entrance slit. Andor works with industy leading manufacturers to deliver solutions to meet any user requirements.

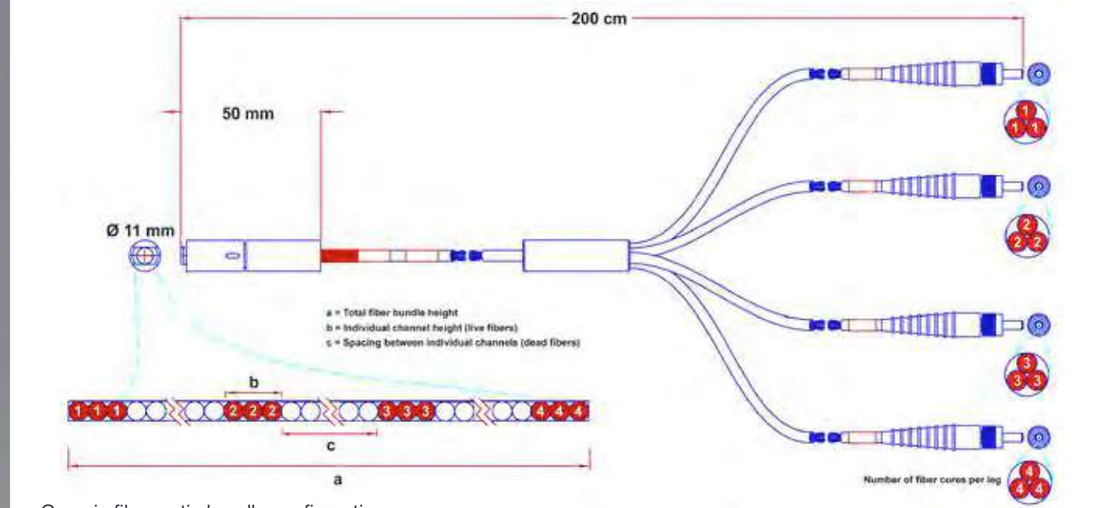

Generic fibre optic bundle configuration

Fibre reference	Number of legs	Fibre core diameter	Optimized wavelength region	Number of fibre cores per leg	a (mm)	b (mm)	c (mm)
SR-OPT-8002	1 way	100 µm	VIS-NIR (LOH)	19	2.38	2.38	-
SR-OPT-8007	2 way	100 µm	VIS-NIR (LOH)	7	2.95	0.875	1.2
SR-OPT-8008	4 way	100 µm	VIS-NIR (LOH)	3	5.625	0.375	1.375
SR-OPT-8009	5 way	100 µm	VIS-NIR (LOH)	3	5.375	0.375	0.875
SR-OPT-8013	3 way	100 µm	VIS-NIR (LOH)	7	5.625	0.875	1.50
SR-OPT-8014	1 way	100 µm	UV-VIS (HOH)	19	2.38	2.38	-
SR-OPT-8015	2 way	100 µm	UV-VIS (HOH)	7	2.35	0.875	1.2
SR-OPT-8016	3 way	100 µm	UV-VIS (HOH)	3	5.625	0.875	1.5
SR-OPT-8017	4 way	100 µm	UV-VIS (HOH)	3	5.625	0.375	1.375
SR-OPT-8018	5 way	100 µm	UV-VIS (HOH)	3	5.375	0.375	0.875
SR-OPT-8019	1 way	200 µm	VIS-NIR (LOH)	19	4.66	4.66	-
SR-OPT-8020	2 way	200 µm	VIS-NIR (LOH)	7	5.43	1.745	2.0
SR-OPT-8021	3 way	200 µm	VIS-NIR (LOH)	3	5.635	0.735	1.715
SR-OPT-8022	4 way	200 µm	VIS-NIR (LOH)	3	5.88	0.735	1.715
SR-OPT-8024	1 way	200 µm	UV-VIS (HOH)	19	4.66	4.66	-
SR-OPT-8025	2 way	200 µm	UV-VIS (HOH)	7	5.43	1.715	2.0
SR-OPT-8026	3 way	200 µm	UV-VIS (HOH)	3	5.635	0.735	1.715
SR-OPT-8027	4 way	200 µm	UV-VIS (HOH)	3	5.88	0.735	1.715

a = Total fibre optic bundle height b = Individual channel height (live fibres)
c = Spacing between individual channels (dead fibres)

Features

- UV-Vis and Vis-NIR optimized options
- Numerical Aperture = 0.22
- 100 and 200 µm fibre core options
- From 1 to 5 leg options as standard
- Standard SMA connectors to Ø 11 mm Andor ferrule
- 2 m overall length – setup convenience and minimum transmission losses
- Re-enforced shield and ruggedised connectors
- Compatible with Andor Shamrock F/number matchers and X-Y adjusters

Have you found what you are looking for?

Need a different fibre core size? A longer overall cable? FC connectors? Additional channels / legs? Please contact your local Andor representative to discuss your specific needs.

Micro-Spectroscopy

Modular approach to combined Microscopy and Spectroscopy

Adding structural and chemical spectral analysis to Microscopy images of bio-samples such as cells and proteins, or materials such as polymers or semi-conductors, is an ever increasing demand amongst the research community. Andor's range of modular interfaces feature cage systems couplers, allowing endlessly configurable connections between Andor Shamrock spectrographs and a wide range of market leading microscopes such as Nikon, Olympus and Zeiss. The Shamrock "wide-aperture" slit opens the door to a single setup with a single detector to image the sample, whilst allowing spectral information collection through the same optical path from the microscope.

"From sample imaging to analytical information"

Key applications

- Micro-Raman
- Micro-Fluorescence - Luminescence
- Micro-LIBS

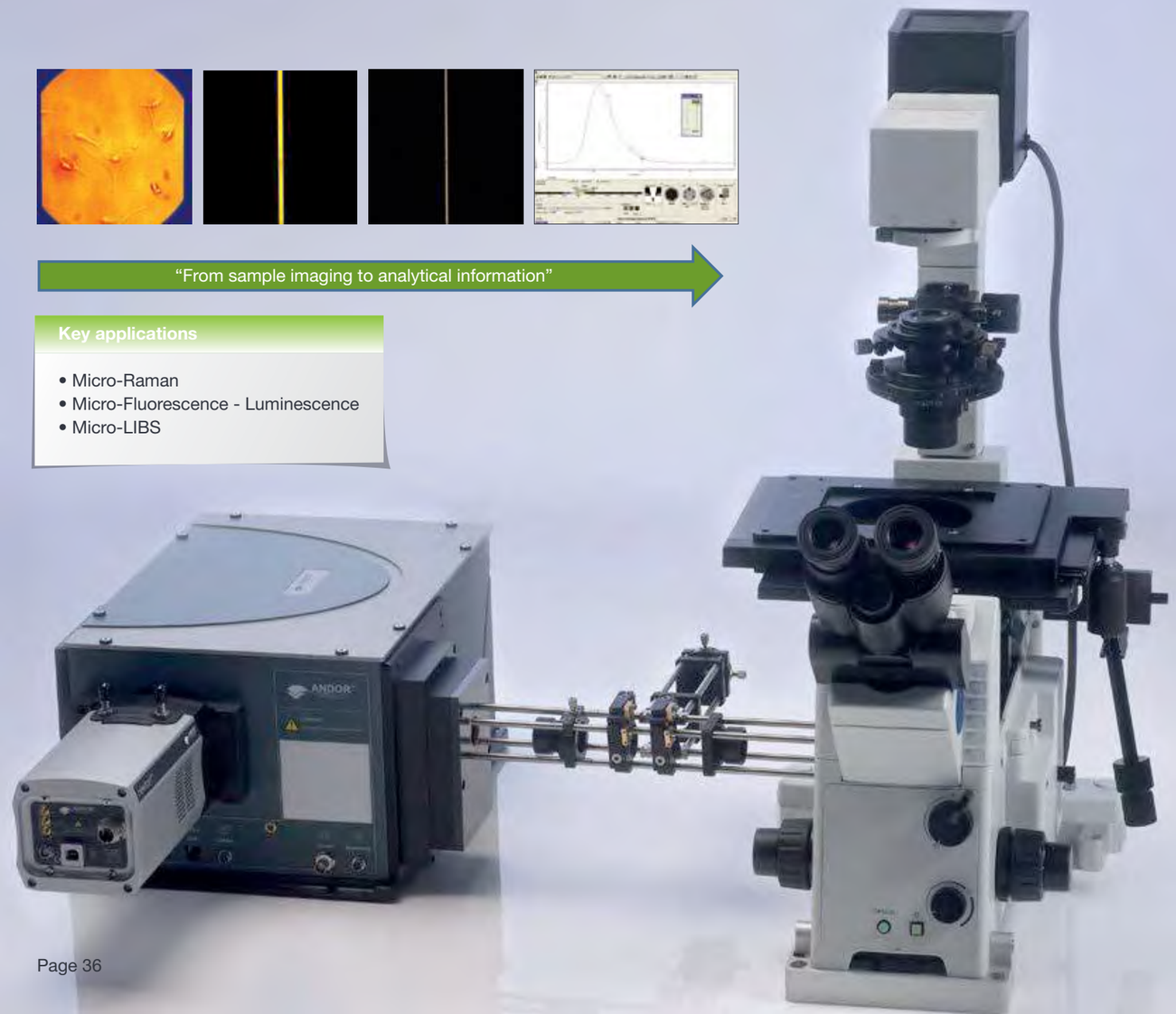

Features	Benefits
C-mount interfaces	Seamless integration of Shamrock spectrograph-based systems to market leading upright and inverted microscopes
Microscope feet	Microscope left or right inverted output options – matches precisely Shamrock spectrograph optical height for accurate opto-mechanical coupling
Wide-aperture slit	Up to 12 mm field of view - Andor's imaging-optimized spectrographs allow high quality sample image relay, without compromise in spectral information collection through the same optical channel
Thorlabs or Linos cage systems compatible interfaces	Fully user-configurable optical setups for Micro-Luminescence and Micro-Raman – compatible with 16, 30 and 60 mm versions
EMCCD compatible	Andor Newton^{EM} and iXon platforms offer a unique combination of single photon sensitivity and high spectral rate and frame rate for challenging low-light Spectroscopy
Software Development Kit	Enables seamless integration with third party hardware and SDK under Labview, C/ C++ and Visual Basic

	Microscope feet for use with Shamrock :		
Microscope configuration	303i based systems	500i and 750 based systems	Microscope to cage system adapter
Leica DMI4000 / 6000 B	TR-LCDM-MNT-127	TR-LCDM-MNT-150	TR-LCDM-CAGE-ADP
Nikon Eclipse Ti-E	TR-NKTI-MNT-127	TR-NKTI-MNT-150	TR-NKTI-CAGE-ADP
Nikon TE-2000	TR-NK2K-MNT-127	TR-NK2K-MNT-150	TR-NK2K-CAGE-ADP
Olympus IX71/81 Left side port	TR-OLIX-MNT-127	TR-OLIX-MNT-150	TR-OLIX-CAGE-ADP
Zeiss Axiovert 200	TR-ZSAV-MNT-127	TR-ZSAV-MNT-150	TR-ZSAV-CAGE-ADP
Zeiss Axio Observer	TR-ZAXO-MNT-127	TR-ZAXO-MNT-150	TR-ZAXO-CAGE-ADP

Scanning Accessories

Perfect complement to Andor's multi-channel detector portfolio

This latest addition to our Spectroscopy portfolio provides a perfect complement to Andor's extensive range of market leading CCD, ICCD, InGaAs and EMCCD detectors. Shamrock spectrograph double detector output configurations allow detection from 180 nm to 12 µm with one single setup. Solis Scanning software platform provides a dedicated single interface for seamless parametring and synchronising of single point detectors, spectrographs, data acquisition unit and lock-in amplifiers, with an intuitive interface for complex experiment acquisition sequences.

Specification sheets
andor.com/spectroscopy

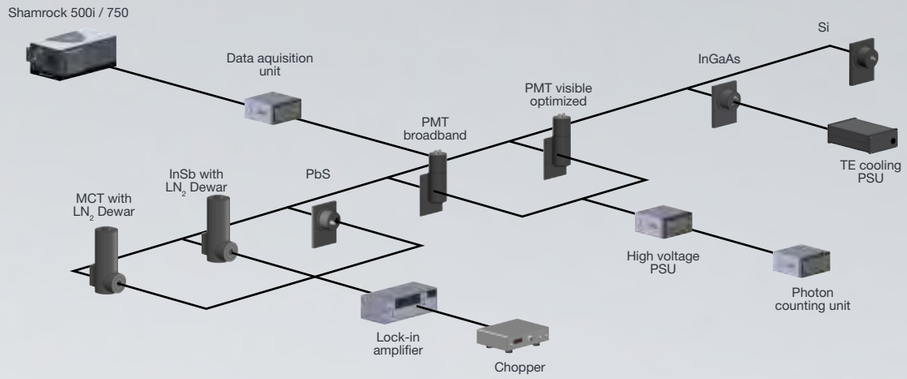

Features	Benefits
Wide range of single point detectors	Selection of PMTs, silicon photodiode, InGaAs, PbS, InSb and MCT detectors for sensitivity up to 12 µm
Seamless integration with Shamrock spectrographs	All detectors include Shamrock flange for easy opto-mechanical coupling
Gold/silver optics coating options	Ensures monochromator maximum throughput in the infrared region of the spectrum – MCT and InSb detectors include gold-coated focusing optics for maximum detection efficiency
Dedicated software interface	Individual set-up interface for SPD, HV power supplies, photon counting and data acquisition units , lock-in amplifiers and monochromators Experiment builder interface for complex experiments involving sequential selection of gratings, filters or monochromators Dedicated GUI for data display and manipulation, including mathematical operators and FFT options
3 acquisition modes	Versatile interface for scanning monochromator, time-resolved and photon counting
USB 2.0 connectivity	Plug-and-play data acquisition unit – allows connection to laptops alongside USB-controlled Shamrock monochromators

Part reference	Detector type	Wavelength coverage	Active area (mm)	Cooling
ACC-SR-ASM-0042	MCT *	2-12 µm	1 x 1	LN_2
ACC-SR-ASM-0043	InSb *	1-5.5 µm	Ø2	LN_2
ACC-SR-ASM-0045	PbS	0.8-2.9 µm	4 x 5	Room temperature
ACC-SR-ASM-0044	InGaAs	0.8-1.9 µm	Ø3	-40°C TE cooling
ACC-SR-ASM-0046	Si	200-1100 nm	Ø11.28	Room temperature
ACC-SR-ASM-0047	PMT (R928)	185-900 nm	8 x 24	Room temperature
ACC-SR-ASM-0048	PMT (R1527P)	185-680 nm	8 x 24	Room temperature

* Including gold-focusing mirror for maximum signal collection

Part reference	Function	Features
ACC-SR-ASZ-0053	HV power supply for PMT	0 to 1.5 kV software-controlled range for PMT gain adjustment
ACC-SR-ASZ-0054	Photon counting unit for PMT	Software-selectable discrimination thresholds
ACC-SR-ASZ-0055	Data acquisition unit	USB 2.0 interface, includes 2x SPD acquisition channels, 2x analog outputs for PMT HV power supply control and connections to lock-in amplifiers **

** Recommended models include SRS SR830 with associated SR540 chopper

Application notes and technical discussions – Andor in action

With over 50,000 users worldwide Andor products are represented in all the major universities, helping researchers to achieve key advances and discoveries by offering cutting-edge Spectroscopy systems based on the latest technologies available. The result is a great breadth of exciting applications, collaborations and testimonials across researchers' publications which Andor is extremely proud to share with the scientific community.

Innovative techniques and cutting edge research:

- Magneto-PL unveils photoluminescence in Si nanocrystals
- NIR micro-photoluminescence characterisation of Single semiconductor Quantum Wires
- Raman Spectral Flow Cytometry
- TERS – Label-free chemical analysis of nanostructures in biofilms
- Stand-off LIBS: a detection technique for explosive residues
- Development of a Raman detector for hyphenation with high-temperature liquid chromatography and isotope ratio mass spectrometry
- Low Dark Current Deep-Depletion (LDC-DD) Technology

Technical discussions – Making sense of sensitivity:

- Detector sensitivity – Key contributing factors and signal-to-noise ratio analysis
- What is the value of LN_2 versus Thermo-Electric cooling for CCDs and InGaAs? Considerations and facts
- Electron-Multiplying CCD technology for Spectroscopy – how to achieve ultra-fast and ultra-sensitive Spectroscopy detection

Application and learning centre
andor.com/learning

View user publications at
andor.com/publications

Have you found what you are looking for?

Cannot see your publications referenced when your work involved Andor equipment? Are you interested to put forward some of your key innovations and results? Do you have spectacular images, movies or posters you would be keen to share? Interested in collaboration work around a particular application? Our team of application specialists will be eager to discuss your ideas.

ANDOR

Application Note

Magneto-PL unveils photoluminescence in Si nanocrystals

Silicon (Si) as a material has dominated the field of microelectronics for quite some time, but when it comes to photonic devices it has had little impact due to its poor light emitting properties. However, nano-structured Si shows a marked increase in light emission efficiency; this was initially observed in porous Si, and more recently in Si nanocrystals.

Explanation of the source of this light emission has been strongly debated over the last two decades, with two possible sources being suggested – a) the influence of localized structural defects and b) the effects of Quantum Confinement (QC) within the nanostructure. Work reported by Dr Manus Hayne and co-workers in Nature Nanotechnology [1, 2], has given much insight into the underlying mechanisms. Using an elegant technique based around magneto-photoluminescence (magneto-PL), they were able to distinguish between the two mechanisms by a cycle of measurements on as-crystallized samples. This was followed by passivation of defects with hydrogen, and the subsequent reintroduction of defects by removal of the hydrogen. A key enabler to their work was the ability to measure the very weak PL signals using the high sensitivity detection capability offered by Electron Multiplication (EM) technology.

The quest for silicon-based photonic devices continues unabated with the ultimate goal of seamless integration of photonic devices, such as sensors or light emitters, and the associated digital data-processing electronics. Currently most photonic devices are based on III-V and II-VI semiconductors, whilst all digital electronics are silicon based. This leads to challenges and limitations when it comes to the integration of the different technologies in one system. One example is the use of optical interconnects from chip-to-chip and board–to-board in electronic systems. The emission of light from silicon nanocrystals has given hope to the developments of fully integrated systems based on one material technology. Hayne and co-workers at Lancaster University, Albert Ludwigs University in Freiburg, the Katholieke Universiteit Leuven, and the University of Antwerp set out to understand the fundamental mechanisms underlying this light emission.

A schematic of the experimental set up used by the team is shown in figure 1. The samples consisted of Si nanocrystals – typical diameter of ~3 nm – embedded in SiO_2, formed by annealing of SiO/SiO_2 layers on Si substrates. Characterization was carried out using high resolution TEM (HR-TEM) imaging, electron spin resonance (ESR) analysis and magneto-PL. PL spectra consisted of broad Gaussian emissions, typically peaked around 1.61 eV (~770 nm with FWHM bandpass of ~130 nm) (see figure 2 inset). Samples were mounted in a cryostatic stage to enable cooling down to 85 K, and a magnetic field, of varying peak field up to 50 T, was applied perpendicular to the plane of the sample (figure. 1). Excitation light in the UV was delivered to the sample via optical fibres which included a bandpass filter to reduce background fluorescence from the fibres. The emitted light was collected into a bundle of fibres and delivered to a 0.3 m (Shamrock 303i) spectrograph with an EMCCD camera (iXon3 DV897-FI). EM gain was set on the camera to enable and optimize measurement of the signal, with a typical exposure time of 5 ms.

In their magneto-PL technique, the application of a high magnetic field is used to manipulate the confinement effects on the free carriers within the nanocrystal [3]. As a consequence of this field-induced 'squeezing' of the electrons, a characteristic shift in the wavelength of the light emitted from quantum confinement states should be observed; the higher the field, the higher the PL energy. However, electrons associated with highly localized defects with a characteristic confinement <1 nm should be unaffected by the magnetic field; the light emitted from these sources is expected to exhibit no shift in PL energy. Hence the method has the ability to distinguish between those states confined to a few nanometers and those associated with defects.

The first set of magneto-PL measurements were carried out on an as-crystallized sample; the PL emission was observed to be insensitive to the application of the magnetic field. The sample was then passivated in pure hydrogen at 400ºC, which served to de-activate the defect sites. The emission from the passivated sample was then observed to give the expected shift in the emission wavelength with variation in the magnetic field strength; there was a shift of ~1.5 meV with the application of a 50 T field. This is illustrated in figure 2. It was also observed that the overall intensity of the emission increased. A characteristic parabolic shift was observed (figure 2) with field increase, consistent with a wavefunction extent of ~5 nm. This confirmed that the emission was dominated by QC effects in this case. The researchers then went on to reactivate the defects by exposing the sample to intense UV illumination, which removed the 'passivating' hydrogen from the defect sites. The PL data again reverted back to showing no sensitivity to the application of the magnetic field, indicative that the emission was again dominated by it due to the localized defects. The results confirmed that when present, defects are the origin of the bulk of the emission within Si nanocrystals, and when there are no defects the emission is dominated by quantum confinement effects within the nanostructure.

EM technology as implemented on the iXon3, successfully met the major challenges posed by such an experiment, namely the sensitivity to measure extremely weak PL signals, and the speed to allow for averaging over a large number of spectral acquisitions.

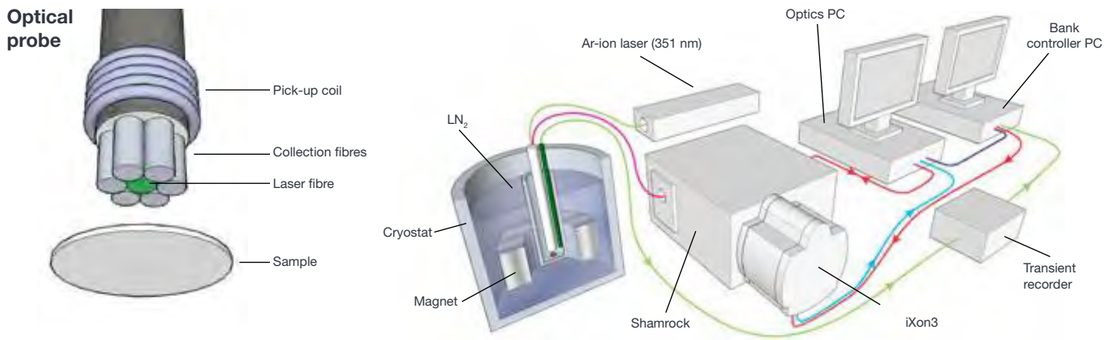

Figure 1: Schematic of experimental set-up at Katholieke Universiteit Leuven, Belgium. The samples were mounted in a cryostat (middle) where they were cooled to 85K. High magnetic fields were applied across the samples as illustrated in the typical characteristic (lower right). The acquisition of the PL signal was timed to coincide with the peak of the applied magnetic field illustrated by the grey bar. The excitation laser was delivered through an optical fibre (top left) and the resultant PL signal was fed via collection fibres into a remotely located Shamrock spectrograph with iXon3 detector.

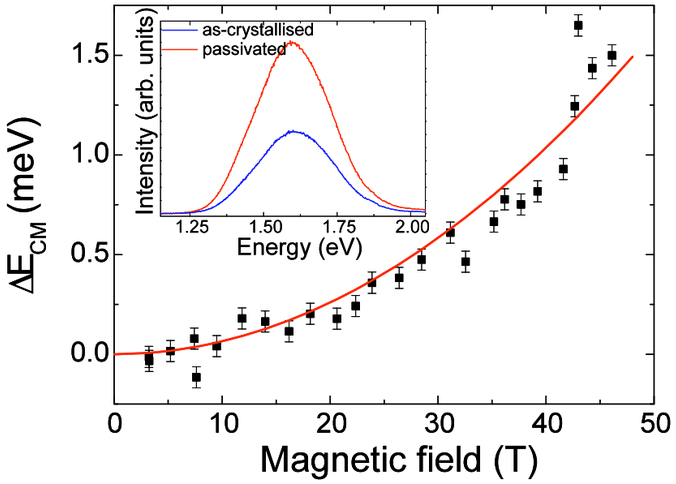

Figure 2: Shift of the photoluminescence (PL) energy for the passivated sample in which there is quantum confinement. The inset shows typical spectrum before (as-crystallized) and after passivation. Note that the PL shift with field is only 1.5 meV and the line width is 300 meV (Courtesy Dr M Hayne, Lancaster University).

Acknowledgement: Graphs courtesy of Dr Manus Hayne, Lancaster University, England.

Reference material:

1) S. Godefroo, M. Hayne, M. Jivanescu, A. Stesmans, M. Zacharias, O. I. Lebedev, G. Van Tendeloo and V. V. Moshchalkov, 'Classification and control of the origin of photoluminescence from Si nanocrystals', Nature Nanotechnology,Vol. 3, March 2008, 174-178.

2) U. Gosele, 'Shedding new light on silicon', Nature Nanotechnology, Vol. 3, March 2008, p134.

3) M. Hayne, J. Maes, S. Bersier, M. Henini, L. Müller-Kirsch, R. Heitz, D. Bimberg and V.V. Moshchalkov, 'Pulsed magnetic fields as a probe of self-assembled semiconductor nanostructures', Physica B, 346-347 (2004), p421-427.

Application Note

NIR micro-photoluminescence characterisation of Single semiconductor Quantum Wires

Nanoscale structures (quantum dots and quantum wires) are being studied extensively with a view to building ever more exotic devices, such as more efficient lasers and LEDs, or quantum information processing components. One type of material under investigation consists of semiconductor quantum wires based on InAs.

These are being explored because of their near-infrared optical properties. Work reported by Dr Benito Alén and co-workers [3] on fundamental studies of isolated InAs nanowires (QWRs) identifies novel behaviour based around the metal-insulator transition in correlated electron systems. They made use of NIR photoluminescence (NIR-PL) to explore the transition dependencies on both excitation power and temperature.

The analysis of the photoluminescence of individual semiconductor quantum wires is an invaluable tool to investigate the role played by attractive and repulsive Coulomb interactions among electrons and holes confined to one dimension. In these systems, the electronic and optical properties change dramatically depending on the number of trapped carriers, but the effect on the emission spectrum can be obscured if many QWRs with different sizes contribute to the emitted light. To ascertain the physics behind and confront the experimental data against existing theories, the photons emitted from just one QWR must be examined using high spatial resolution techniques and high sensitivity light detectors. This approach has been demonstrated for InAs/InP QWRs emitting at 1.5 µm, by researchers in Spain at the Consejo Superior de Investigaciones Científicas (CSIC) and the Universidad de Valencia.

The prediction of low threshold for laser emission, reduced temperature sensitivity, and slow surface recombination velocity has largely motivated the research on III-V semiconductor QWRs for optoelectronic applications in recent years. Among them, self-assembled InAs/InP QWRs can get their spontaneous emission tuned beyond 1.6 µm and their areal density reduced down to a few QWRs per square micron [1]. They are therefore ideal candidates for the fabrication of advanced light sources in the telecom spectral region [2], and for the study of novel semiconductor physics. As for the latter, collective phenomena of one-dimensional excitons have been directly investigated in these nanostructures using NIR microphotoluminescence (µ-PL) techniques at low temperature, at the Universidad de Valencia and published by B. Alén et al. in Physical Review Letters [3].

The system consisted of a fibre-based confocal microscope arrangement inserted in the exchange gas chamber of an immersion liquid He cryostat. Excitation light from a 950 nm diode laser was brought into the microscope through a single mode optical fibre whose core acted as the excitation pinhole. The laser light was focused onto the sample through an objective lens (NA=0.55) producing a diffraction limited spot at the excitation wavelength. Light emitted by the few QWRs present in the excitation spot (see AFM image in figure 1) was collected by the same objective and focused onto a different optical fibre which in turn was connected at its opposite end to a spectrometer equipped with a TE cooled Andor iDus InGaAs (DU490A-1.7) camera. The faint light emitted from the individual QWRs could be detected using exposure times of 10 to 100 seconds thanks to the multichannel detection capabilities of the iDus InGaAs array and low dark current of the cooled array. The samples were made using self-assembly methods of epitaxially growing InAs structures on InP (001) substrates under conditions which preferentially led to the formation of QWRs rather than quantum dots (QDs). Reflection high-energy electron diffraction (RHEED) and Atomic Force Microscopy (AFM) analyses were used to characterize the morphology and aspect ratio of the individual QWRs. These structures were typically 20 nm wide and 200 nm long, corresponding to aspect ratios of ~1:10. Experiments were carried out to investigate how the samples behaved with variation in the excitation power, with powers as low as 8 mW up to 260 mW. They also investigated the temperature dependence.

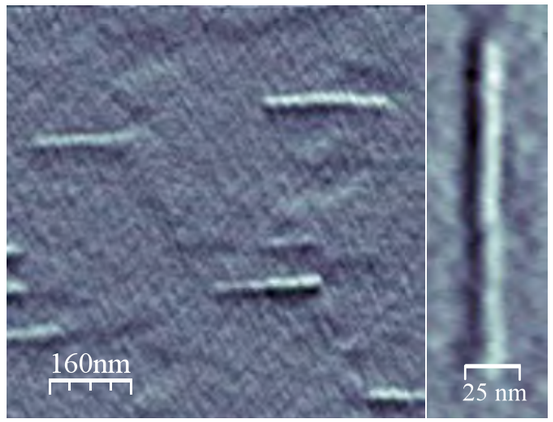

Fig 1: AFM image of the investigated QWRs (Courtesy Dr B Alén, CSIC, Madrid)

Typical examples of µ-PL spectra collected on a single QWR as a function of excitation power density are depicted in figure 2. Due to the quantum confinement size effect, the different sized QWRs can emit at different energies, but they show a similar trend with the increasing photo-generated carrier density. The analysis of the lineshape of several spectral features observed at low and high excitation allowed a detailed study of the metal-insulator transition governed by enhanced Coulomb correlations in these systems. At low powers the sharp spectral feature at ~0.812 eV (~1528 nm) dominated whilst at high powers the broad spectral feature centred at ~0.807 eV(~1538 nm) dominated. This change in PL emission, induced by changes in carrier density, was indicative of the metal-insulator transition. The spectra show that the insulating excitonic gas (associated with high energy peaks – blue) condenses into a metallic-like electron-hole liquid phase (associated with the low energy band - red), with an increase in carrier density.

Novel behaviour on the metal-insulator transition within a correlated electron system, as realized in single InAs/InP QWRs emitting in the NIR, was clearly demonstrated by Alén and co-workers. They developed techniques based on µ-PL, which allowed exploration of the carrier interactions and its dependence on photo-excitation powers and temperature. These fundamental studies will underpin future developments of ever more exotic devices such as high efficiency micro-/nano- lasers and LEDs.

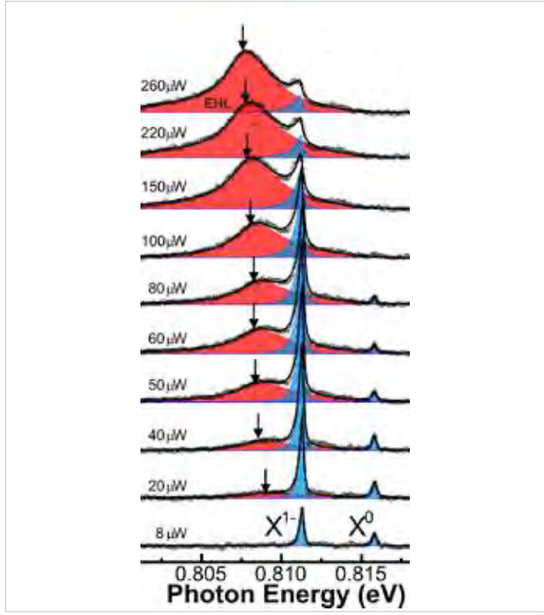

Figure 2. Typical single QWR emission spectra measured at 5 K with increasing excitation power . (Courtesy Dr B Alén, CSIC, Madrid)

Acknowledgement: Appreciation is gratefully extended to Dr Benito Alén, IMM-CSIC, Madrid and Prof. Juan Martinez Pastor, Universidad de Valencia, Spain.

Reference material:

1) D. Fuster, B. Alén, L. González, Y. González and J. Martínez-Pastor, "Initial stages of self-assembled InAs/InP(0 0 1) quantum wire formation". Journal of Crystal Growth 301 (2007), 705.
2) L. J. Martínez, B. Alén, I. Prieto, D. Fuster, L. González, Y. González, M. L. Dotor, and P. A.Postigo, "Room temperature continuous wave operation in a photonic cristal microcavity laser with a single layer of InAs/InP self-assembled quantum wires", Optics Express 17 (2009), 14993.
3) B. Alén, D. Fuster, G. Muñoz-Matutano, J. Martínez-Pastor, Y. González, J. Canet-Ferrer and L. González, "Exciton Gas Compression and Metallic Condensation in a Single Semiconductor Quantum Wire", Phys. Rev. Lett. 101 (2008) 067405.

ANDOR

Application Note

Raman Spectral Flow Cytometry

A key and continuing goal in the development of flow cytometry techniques is the ability to measure ever more parameters for each particle under test. Work carried out by Prof John Nolan's group at La Jolla Bioengineering Institute, and reported by Watson et. al. [1] in Cytometry A, outlines the development and operation of a Raman Spectral Flow Cytometer (RSFC), which is perhaps the most radical and challenging approach to current efforts in spectral flow cytometry.

In their 'proof of principle' system, Watsons' team bring together Raman Spectroscopy, via Surface Enhanced Raman (SERS), and conventional flow cytometry, by substituting a dispersive-optic spectrograph with multichannel detector (CCD), in place of the traditional mirrors/beam splitters, filters and photomultipliers (PMT) of conventional flow cytometers. They demonstrate a system of sufficient sensitivity to acquire and analyze SERS spectra with good spectral resolution from samples consisting of nanoparticle SERS tags bound to microspheres. The functionality and power of the system is illustrated using two analytical methods, virtual bandpass filtering and principal component analysis (PCA), to distinguish between the different Raman species within their test samples.

A significant motivation for the group's work is to increase the multiplexing capability of cell and particle-based flow cytometry applications. This requires the ability to access more parallel data channels from the same sample at the same time. Conventional systems have been developed to offer higher numbers of simultaneously measureable parameters. Specially configured systems with up to 19 parameters are available (direct scatter, side scatter and multiple fluorescence channels) but this requires multiple PMTs, filters, several lasers, multiple fluorophore labels and wavelength selective mirrors. The problem that arises with trying to extend such systems to more channels, apart from the expense and the operating challenges, is the inherently broad fluorescence characteristics of the fluorophores. As the number of fluorophore fluorescent bands is increased, the more overlapping of bands takes place and it becomes increasingly difficult to distinguish the individual signal channels. This limits the number of possible data channels.

Having a dispersive-optic based system provides a simpler setup configuration and the potential for high resolution Spectroscopy. The La Jolla group has chosen Surface Enhanced Raman Spectroscopy (SERS), with its characteristically information-rich narrow band spectral features, as a route to accessing a higher number of measureable parameters. Two key technologies are being drawn upon in the development of fresh approaches to flow cytometry. The first, a), takes advantage of the ability of silver nanoparticles to enhance the Raman scattering intensity of an active species by many orders of magnitude, or as in other work, the use of fluorescent nanocrystals, with their relatively narrow emission bands, as markers of the species of interest. The second, b), is the development of Electron Multiplication CCD detectors (EMCCD), with their enhanced sensitivity which is advantageous when fast spectral rates and short exposure times are a requirement. Other groups working on spectral flow cytometry are focusing on fluorescence signatures [2] to characterize the sample. Some of these groups use multianode PMTs or avalanche photodiodes (APD) rather than CCDs for the detectors.

Figure 1 illustrates the flow cell and the interaction region where the laser excites the sample particles or cells. A schematic of the RSFC instrument is shown in figure 2. It shows the main components used: the laser and its delivery into the flow cell (FC) with focusing optics (A); the detection of the Rayleigh side scattered signal, collected by lens optics (C) into an optical fibre (OF) and delivered to a photomultiplier (PMT); the SERS signal collected (B) and coupled into an optical fibre connected to a spectrograph with long pass filter (LP) to eliminate the Rayleigh scatter at the laser wavelength; a Newton EMCCD camera captured the spectral data; the forward scattered data was detected with a photodiode (not shown), which also acted to deliver triggering for acquisitions by the camera.

Their test samples consisted of glass-encapsulated SERS tags (Ag nanoparticles of ~67 nm diameter, with an absorbed Raman reporter molecule and encapsulated in glass), bound to the surface of polystyrene microspheres (3.3 µm diameter with ~8000 nanoparticles per microsphere). Four different Raman reporters were used in the preparations, each giving its own characteristic Raman signature: each microparticle was tagged with one out of the four Raman reporters. Data was captured for each particle as it passed through the interaction region (figure 1) in the form of a Raman spectrum, typical examples of which are shown in figure 3. Clearly there is potential for a wealth of information from the sharp and highly resolved spectral features of these spectra compared with the broadband data attainable with the traditional filter systems or indeed spectral techniques using fluorescent markers.

Watson et.al. then proceed to demonstrate two powerful methods for analyzing their data to discriminate between the four different types of microparticle. The first approach, referred to as 'virtual bandpass filtering', is analogous to the real-time filtering bandpass techniques of conventional flow cytometry. It offers the possibility to define 'optical filters' to select regions from the SERS spectra to emphasize differences between the four types of particle, leading to the derivation of a new set of parameters for comparison purposes. A particularly nice aspect of this method is the flexibility for optimization, by both readjustment of the virtual bandpass regions and defining the number of new parameters to be used. However, Watson et.al. point out that this approach becomes complex and cumbersome, as the number of SERS tags increases, with their associated density and overlap of spectral features.

The second method they used to distinguish the four SERS tags was that of Principal Component Analysis (PCA). PCA was applied to the first order derivative that was calculated from the smoothed and normalized SERS spectra; the ability to discriminate between different SERS tags, with this advanced and well established analysis technique, was clearly demonstrated.

The use of a spectrograph with spectral deconvolution algorithms has the potential for a more comprehensive and flexible approach to multi-color or multiparameter analysis. The La Jolla group has developed such a system as a new addition to the tools of flow cytometry, the Raman Spectral Flow Cytometer (RSFC). Challenges remain in terms of speed and sensitivity whilst maintaining good resolution. Advances in camera acquisition rates and digital processing speeds will enable faster analysis rates – a key requirement of modern flow cytometry. The coming years will see these challenges being addressed; the potential benefits as regards biological applications are immense.

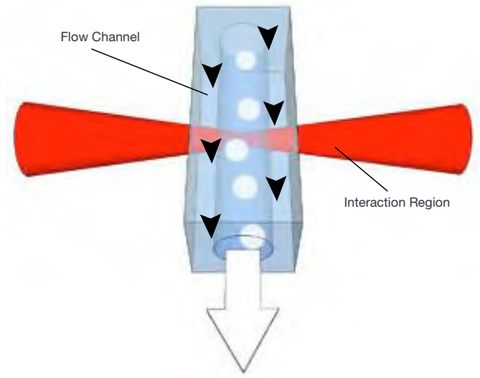

Figure 1: Schematic of the particles in the fluid flow and interaction region of the laser within the flow cell.

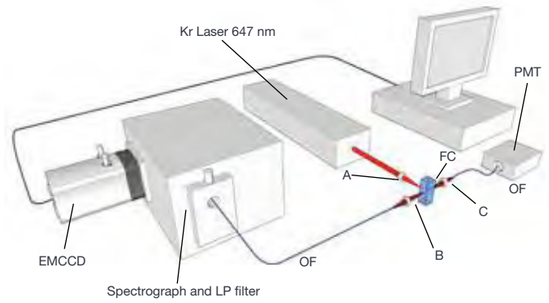

Figure 2: Schematic of RSFC instrument

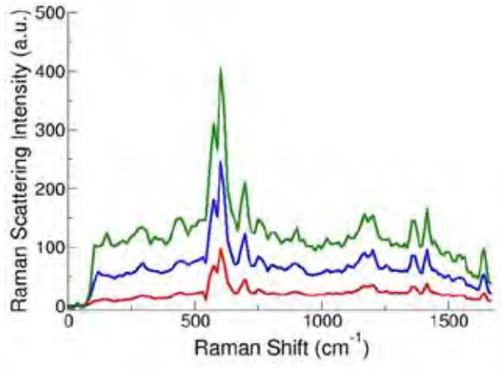

Figure 3: Sample SERS spectra from SERS tag-labelled microparticles. (D. Sebba and J. Nolan, unpublished data)

Acknowledgment: Appreciation is gratefully extended to Prof John Nolan and his group at La Jolla Bioengineering Institute, CA, USA.

Reference material:

1) Dakota A Watson, Leif O Brown, Danial F Gaskill, Mark Naivar, Steven W Graves, Stephen K Doorn and John P Nolan, 'A Flow Cytometer for the Measurement of Raman Spectra', Cytometry Part A, Vol 73A, p119-128, (2008)
2) Gregory R Goddard, J P Houston, John C Martin, Steven W Graves, James P Freyer, 'Cellular discrimination based on spectral analysis of intrinsic fluorescence', Proc. Of SPIE, Vol. 6859 685908-1, (2008)
3) John P Nolan, 'Raman Spectroscopy Meets Flow Cytometry', www.photonics.com/content/bio/2008/April/bioFeatures

Application Note

TERS – Label-free chemical analysis of nanostructures in biofilms

Tip-Enhanced Raman Spectroscopy (TERS) is developing into a powerful technique for the characterization of bio-molecules at the nanoscale level [1,2,3,4,5]. It facilitates chemical imaging on the scale of single molecules, extending well established techniques such as surface enhanced Raman Spectroscopy (SERS) and Raman mapping.

Work by Dr Thomas Schmid and co-workers from Prof. Renato Zenobi's group at the Dept of Chemistry and Biosciences, ETH Zurich, demonstrates the use of TERS for label-free chemical characterization of nanostructures in biological specimens [1]. The biofilm system chosen for the investigation was based on calcium alginate fibres. TERS provides detailed chemical information at very high spatial resolutions (<50 nm), with one key advantage being label-free characterization. A TERS system essentially brings together scanning probe, microscopy and Spectroscopy technologies.

Prof Zenobi's group set out to test the feasibility of using TERS to carry out label-free chemical characterization of nanostructures within biofilms. Label-free techniques remove the challenges of labeling samples using dyes or tags. Calcium alginate fibres were considered a good representative model for the extracellular polysacharrides of biofilms.

A schematic of the setup used is shown in figure 1. It essentially consisted of three main subsystems – an Atomic Force Microscope - AFM (Veeco Instruments), an inverted confocal laser scanning microscope – CLSM (Fluoview, Olympus), and a Raman Spectroscopy system consisting of a Holospec F/1.8i spectrograph (Kaiser Optical Systems) and an iDus 420 CCD camera (Andor Technology). The excitation laser (532 nm) was delivered via a single mode fibre. The CLSM unit delivered the light into the microscope, where it was focused onto the sample with an oil immersion objective (60x and NA=1.4). The scattered Raman signal was collected by the same objective and passed back through the CLSM unit and a beam splitter to be focused into a multimode fibre, which delivered the signal to the entrance port of the spectrograph. An edge filter placed in front of the spectrograph was used to reject the Rayleigh scattered light from entering the spectrograph. The sample could be scanned in 2D by control of the x-y stage upon which the sample was mounted. A folding mirror in the system allowed for rapid switching between confocal imaging and spectral acquisitions modes.

There are number of key challenges when attempting TERS with such materials. These include:

- the probe tip quality - its shape, size and cleanliness
- carbon contamination - either from ambient or photodecomposition
- heating effects
- oxygen-mediated photobleaching
- the weak Raman activity offered by these particular macro-molecules [3]
- the complexity of the molecules - a large number of functional groups

Generally one is operating in a low light regime when collecting TERS spectra from a sample consisting of a few molecules. By carefully coating the silicon tip with silver, significant enhancements in the Raman signal are possible; typical enhancements of ~10^4 can be achieved. This enhancement is attributed to two main mechanisms:

- the excitation of surface plasmon modes between the tip and sample resulting in a multifold increase in the electric field intensity localized at the tip
- chemical enhancement due to the Charge Transfer (CT) mechanism when the molecules' functional groups are in direct contact with the metal tip

Illustrative data is shown in figure 2. An AFM image is on the left and background corrected TERS spectra on the right. The latter were produced when the tip was a few nanometers from the surface (near-field). In contrast, when the tip was the order of microns from the surface (far-field), it had no effect and no spectral signature was evident even with very long exposures (10 mins). Schmid and coworkers identified characteristic marker bands for the macromolecules studied. They observed shifts in the Raman band positions for these complex macromolecules, in contrast to observations for the corresponding bulk samples of the same material which showed no shifts. It also contrasts with less complex molecules where there was no observed shift in the bands for the TERS spectra. They attributed the shifting in large part to the influence of chemical enhancement (CE) processes occurring at the tip interface.

In the first application of TERS on alginates, the group successfully demonstrated the collection of weak Raman spectra at high spatial resolutions from extracellular polymeric substances (EPS) without the need for labeling. Such materials include polysaccharides, nucleic acids and proteins. This work represents a significant step forward in the development of the TERS technique as a reliable, accessible, and robust analytic technique for many applications in the life science, medical and materials fields.

Low photon signals place increased demands on the sensitivity of the detector used and the collection efficiency of the optical system. Only high performance cameras can give the required signal to noise ratios to make such measurements possible. The ideal system will be capable of single photon detection - an area where Electron Multiplying (EM) technology is of a definite benefit. High sensitivity facilitates the use of lower excitation fluences; this minimizes thermal effects and damage to the sample.

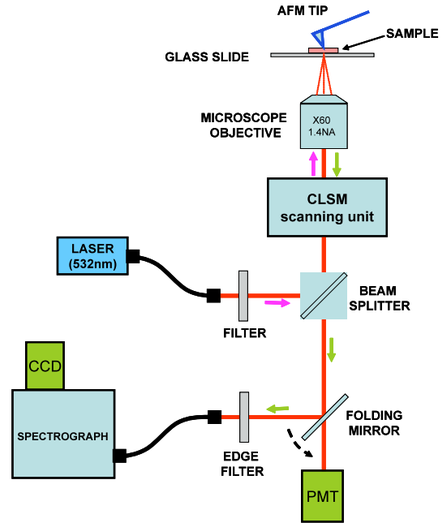

Figure 1: Schematic of the set-up used by Schmid and co-workers for acquisition of TERS spectra.

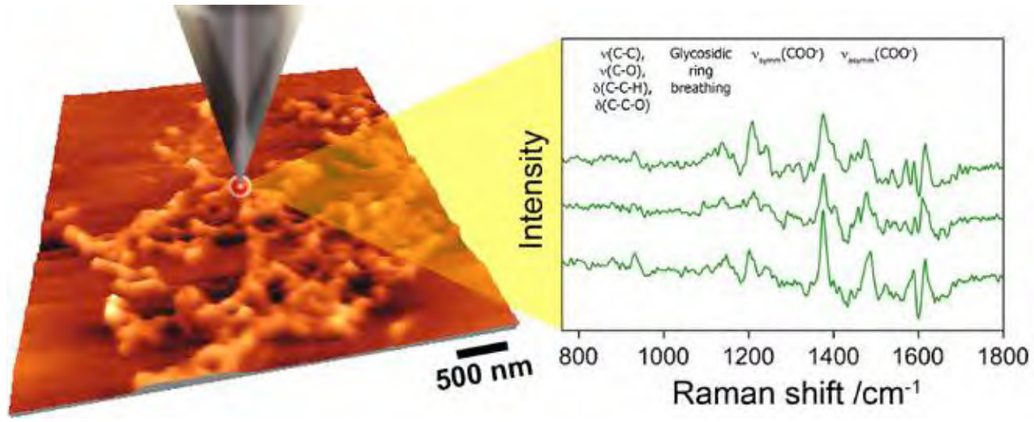

Figure 2: The TERS concept – a metallized tip is used to enhance the Raman response. An AFM image is shown to the left and sample Raman spectra taken from biofilm material is shown to the right. (Courtesy of Prof Zenobi's group, ETH, Zurich)

Acknowledgement: Appreciation is extended to Prof. Zenobi's group, Dept. of Chemistry and Applied Biosciences, ETH Zurich, Switzerland.

Reference material:
1) T Schmid, A Messmer, Boon-Siang Yeo, Weihua Zhang, and R Zenobi. 'Towards chemical analysis of nanostructures in biofilms II: tip-enhanced Raman Spectroscopy of alginates'. Anal Bioanal Chem, 391, pp1907–1916 (2008)
2) C Vannier, Boon-Siang Yeo, J Melanson, and R Zenobi. 'Multifunctional microscope for far-field and tip-enhanced Raman Spectroscopy'. Review of Scientific Instruments 77, 023104(1-5) (2006)
3) Boon-Siang Yeo, J Stadler, T Schmid, R Zenobi, and Weihua Zhang. 'Tip-enhanced Raman Spectroscopy – Its status, challenges and future directions'. Chemical Physics Letters 472, 1–13 (2009)
4) APD Elfick and AR Downes. 'Development of tip-enhanced optical Spectroscopy for biological applications: a review'. Anal. Bioanal. Chem. 396, pp45-52 (2010)
5) J Steidtner and B Pettinger. 'Tip-Enhanced Raman Spectroscopy and Microscopy on Single Dye Molecules with 15nm Resolution'. Physical Review Letters, 100, 236101 (2008)

Application Note

Stand-off LIBS: a detection technique for explosive residues

Stand-off techniques have received increasing attention as valuable methods for material analysis at remote distances. This is particularly relevant when looking at hazardous contaminants in the environment or residual explosive material, where it is desirable for the analyst to remain at a safe distance from the material being investigated.

Work carried out by Prof JJ Laserna's group at the Dept of Analytical Chemistry in the University of Malaga, reported by González et.al [1], explores the use of stand-off Laser Induced Breakdown Spectroscopy (stand-off LIBS) for the detection of explosive residues in situations simulating 'real environment' scenarios. They looked at the feasibility of detecting the likes of improvised explosive materials (IEM) through windows such as those in cars or buildings or within various types of container. A telescopic system was used to focus a high power pulsed laser to a spot on the material to produce a micro-plasma. The same telescope collected the light emission from this plasma which was then analyzed in a spectrograph using the advanced time-gating of an intensified CCD camera.

The ability to detect dangerous contaminants, improvised explosives (IED), home made explosives (HME), or nuclear by-products, has become of increasing importance due to heightened risks in recent decades. In their work, Gonzalez and co-workers set out to test the feasibility of making such measurements with their TELELIBS sensor, and to assess the influences that the barrier position and its composition might have on the quality of those measurements. In allied work the group looked at the influence of atmospheric turbulence on beam propagation to and from the target [2], where they showed that measurements over several tens of meters could be significantly affected by atmospheric turbulence.

A schematic of the typical experimental set up used by the Malaga group is shown in figure 1. It consists of a telescope which takes the light from a laser and focuses it on to a target at a distance of typically 30 m. Two Nd:YAG lasers were used at the fundamental wavelength of 1064 nm, delivering 5 ns long pulses at 10 Hz, and energy of 800 mJ. The two laser outputs were arranged to be overlapped in space and time so that the overall irradiance on target was doubled.

The emission light from the micro-plasma was collected by the same telescope and delivered into a 600 µm core diameter fibre via a dichroic mirror. The excitation source was reflected by the dichroic mirror into the telescope whilst the returning atomic emission light was transmitted through the mirror, where it was then coupled into the optical fibre for delivery to the spectrograph. A Czerny-Turner spectrograph (Shamrock 303i) with an intensified CCD camera (iStar DH740-25F-03) was used to detect the emission. In any LIBS experiment one of the main challenges in attempting to collect discernible atomic emission line spectra is to reject the broad band continuum which occurs during the incidence of the laser pulse and immediately afterwards as the plasma plume evolves. This broad continuum tends to dominate the emission early in time resulting in little or no atomic line data being evident. However, an ICCD allows the acquisition by the camera to be delayed for a time in order to reject this early continuum. In this work a delay of 400 ns was used along with an exposure or integration time of 9 µs.

Among the substances investigated were sodium chlorate ($NaClO_3$), dinitrotoluene (DNT), trinitrotoluene (TNT), and some plastic explosives (C2 and H15). A number of barrier materials, including clear glass, some tinted glasses, and colorless PMMA (a polymer material) were placed in the beam path. The team investigated the influence of the target-to-barrier distance on the measured signal to background (S/N) ratios, along with the influence of the optical characteristics of the barrier material, thus accounting for the transmittance of excitation laser light and the returning plasma emission. A suite of chemometric tools were used to analyze the spectral data for the presence or absence of explosive residues.

A number of spectral bands and atomic/ionic emission lines were chosen for fingerprinting and subsequent identification of the explosive substances: examples of such features included the CN band (388.3 nm), the C2 band (471.5 nm, 516.5 nm and 563.5 nm), and the Al (I) line (469.4 nm) among others. The ability to detect a residue was determined by the 'sensitivity' and 'specificity' of the measuring system. Sensitivity is related to the system's ability to identify the presence of an explosive material if it is present i.e. the system flags up the presence of the material when it should. Specificity is related to its ability to identify explosives only if they are present i.e. the system doesn't flag up the presence of explosive when it shouldn't. González and co-workers assessed the capability of their system by measuring the sensitivity for the different residues with the different barrier materials. By increasing the number of laser shots it was possible to increase the detection to 100% sensitivity without impacting on specificity.

Gonzalez and co-workers successfully demonstrated the feasibility of using the stand-off or TELELIBS technique for detection of explosive materials through different types of window or interposed barriers, as long as there was a clear line of sight from the sensor system to the target. They also demonstrated that relatively few laser shots were required to ensure a high level of detection capability and means of distinguishing different residues and that the position of the barrier relative to the target and sensor was unimportant to the analysis. A key enabler for this type of work is the high sensitivity and gating versatility offered by the iStar ICCD camera. Research and validation on stand-off analysis techniques has gained much momentum as demands grow for safe, convenient and quick ways of testing for improvised explosives devices and other hazardous contaminants in the environment.

More recently the group have demonstrated the simultaneous use of both stand-off LIBS/stand-off Raman to analyse such materials [4].

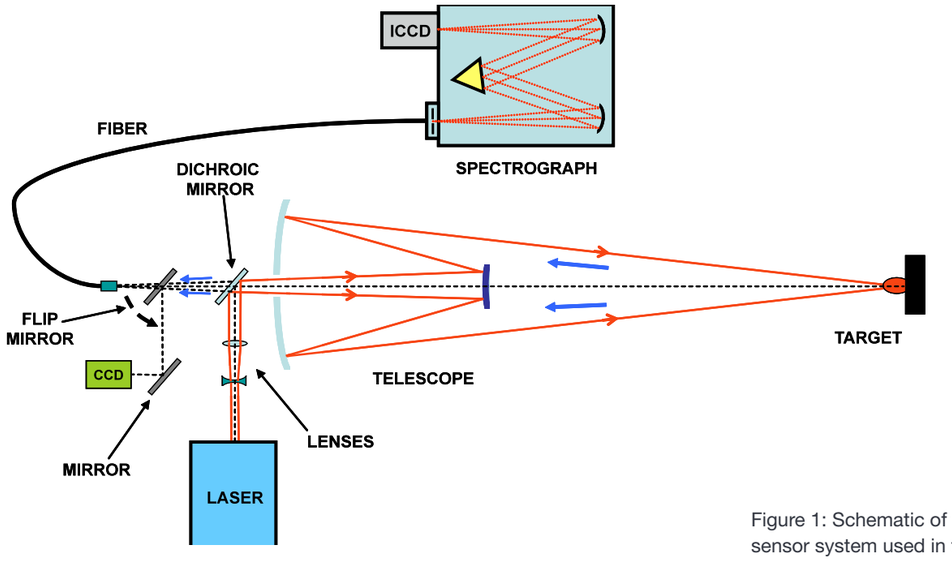

Figure 1: Schematic of the TELELIBS sensor system used in the experiments

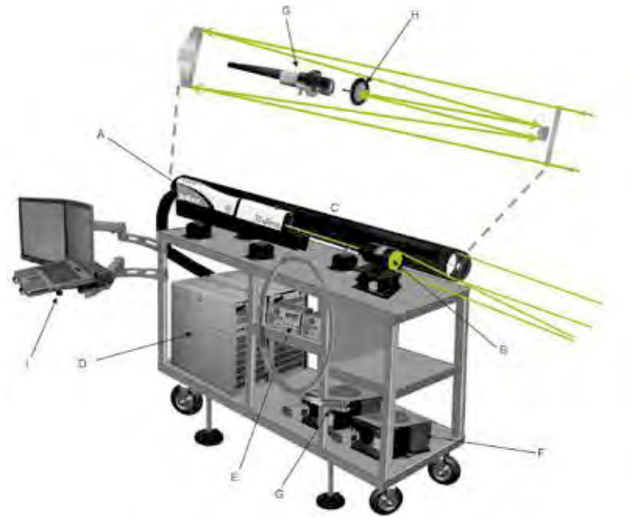

Figure 2: Schematic picture of combined LIBS-Raman system used by the Laserna group.
A – laser, B - focusing optics,
C – telescope, D - power supplies,
E – delay generators, F - spectrographs,
G – fibres, H – notch filter, I – laptop.

Acknowledgement: Appreciation is gratefully extended to Prof JJ Laserna and his group, University of Malaga, Spain.

Reference material:

1) González R, Lucena P, Tobaria LM and Laserna JJ. 'Standoff LIBS detection of explosive residues behind a barrier'. J. Anal. At. Spectrom., 24, 1123–1126 (2009)

2) Laserna JJ, Fernández Reyes R, González R, Tobaria L, and Lucena P. 'Study on the effect of beam propagation through atmospheric turbulence on standoff nanosecond laser induced breakdown Spectroscopy measurements'. Optics Express, 17, No. 12, pp 10265-10276 (2009)

3) Luis Alonso Alvarez-Trujillo, Alejandro Ferrero and J. Javier Laserna. 'Preliminary studies on stand-off laser induced breakdown Spectroscopy detection of aerosols'. J. Anal. At. Spectrom., 23, pp 885–888 (2008)

4) J Moros, JA Lorenzo, P Lucena, LM Tobaria, and JJ Laserna. 'Simultaneous Raman Spectroscopy-Laser-Induced Breakdown Spectroscopy for Instant Standoff Analysis of Explosives Using a Mobile Integrated Sensor Platform'. Analytical Chemistry, 82 (4), pp 1389–1400, (2010)

Application Note

Development of a Raman detector for hyphenation with high-temperature liquid chromatography and isotope ratio mass spectrometry

Due to criminal statistics, product and trademark piracy have raised dramatically in recent years. The critical numbers of fake articles in foodstuffs, pharmacy and cosmetics exhibit potential risks for public health. Product piracy can be identified by determining the origin and authenticity of the chemical compounds that are part of fake articles.

After applying a separation by high-temperature high performance liquid chromatography (HT-HPLC) origin and authenticity of analytes are revealable by isotope ratio mass spectrometry (IRMS). The sole linkage of HT-HLPC and IRMS can be used if the composition of samples is known. The analysis of samples with unknown composition additionally requires the identification of the separated compounds. Especially for this experimental approach we developed a detector based on Raman spectroscopy. The principle of measurement is shown in Figure 1:

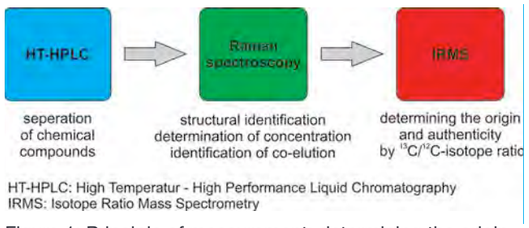

Figure 1: Principle of measurement; determining the origin and authenticity of chemical compounds by linking different analytical techniques.

Experimental Setup

The hyphenation of HT-HPLC, Raman detector and IRMS is displayed in Figure 2. The Raman device was set between HT-HPLC and IRMS and operated like a flow cell for online detection. The laser light was guided by the optical fibre 1 to the T-piece 1 which coupled the HT-HPLC capillary tubing, the liquid core waveguide and the optical fibre 1.

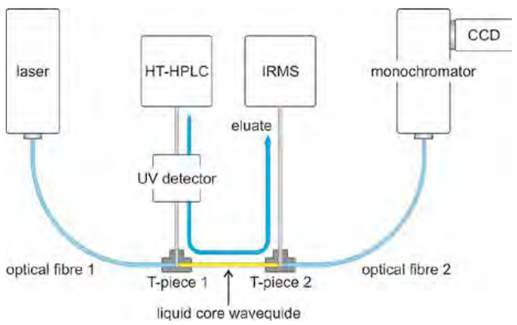

Figure 2: Experimental setup; hyphenation of HT-HPLC/ Raman/IRMS.

Raman signals were generated within the liquid core waveguide. The Raman light was collected by optical fibre 2 that directed the scattered light to the monochromator and CCD detector (HoloSpec f/1.8i from Kaiser Optical Systems and Newton DU920P-BV from Andor Technology, Figure 3) for the spectral analysis.

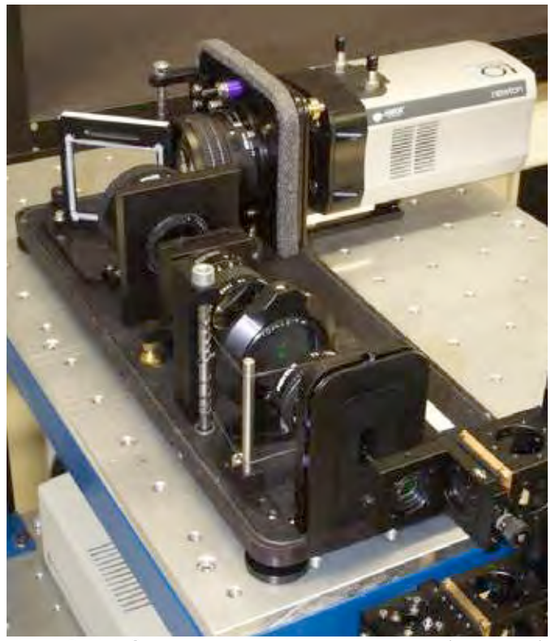

Figure 3: HoloSpec spectrograph monochromator (open view) and Andor Newton CCD detector.

Figure 4 shows a photo of the flow cell device and the liquid core wavequide during Raman measurement.

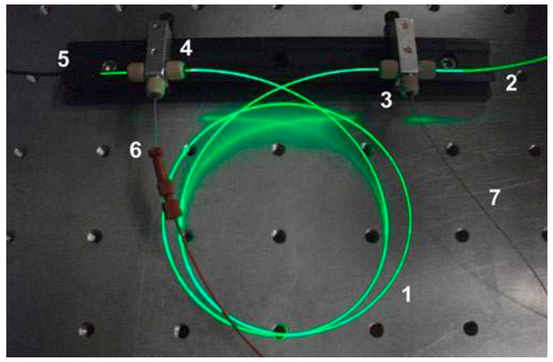

Figure 4: Flow cell device during Raman measurement, excitation wavelength: 532nm, 1: Liquid core waveguide with ID=250µm, length=1m, 2: Optical fibre 1, 3: T-piece 1, 4: T-piece 2, 5: Optical fibre 2, 6: Capillary tubing from HTHPLC, 7: Capillary tubing to IRMS.

Results

The applicability of the described setup was tested with a mixture of sulfathiazole and sulfamerazine. The analytes were solved in a 50:50 mixture of water and methanol with a concentration of 100 mg·L-1 for each substance. The injection volume on column was 20 µL. With a laser power of 2 W and a detection time of 10 s we could observe Raman spectra that are displayed in Figure 5.

Conclusion

Raman spectroscopy is ideally suited as a novel on-line detection technique for the hyphenation of high-temperature liquid chromatography with isotope ratio mass spectrometry. Analytes can be unambiguously identified by their characteristic Raman spectra. Addicted to the Raman scattering cross section of the analysed substance we currently achieved a limit of detection between 1 - 4 mg·L-1 (< 10-5 M).

Acknowledgement

This work is part of a close cooperation with the Institute of Energy and Environmental Technology e.V., IUTA (working group of Dr. T. Teutenberg) and the University Duisburg-Essen, Instrumental Analytical Chemistry (working group of Prof. Dr. T. C. Schmidt).
The authors would like to thank for financial support from the German Federal Ministry of Economics and Technology within the agenda for the promotion of industrial cooperative research and development (IGF) based on a decision of the German Bundestag. The access was opened by the Verein zur Förderung der Energie- und Umwelttechnik e.V., VEU, Duisburg and organised by the AiF, Arbeitsgemeinschaft industrieller Forschungsvereinigungen e.V., Köln, (IGF-Project No. 16120 N/2).

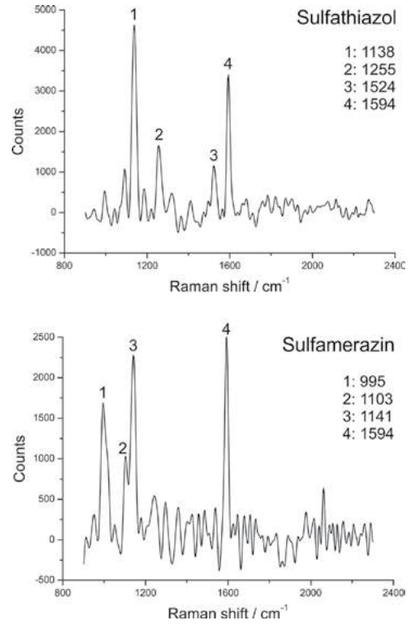

Figure 5: Online Raman measurement of sulfathiazole and sulfamerazine after separation by HT-HPLC.

References

Schmidt T. C. et al., Kopplungsverfahren zur Authentizitätskontrolle - Neuartige Kombination innovativer Detektionstechniken auf Basis der Isotopenverhältnismassenspektrometrie und Ramanspektroskopie, GIT Labor-Fachzeitschrift, 54-3 (2010), p. 182-185.

Teutenberg T. et al., Do We Really Need Chromatography?
– The Role of Chromatography and Different Detection Techniques in Context of Mass Spectrometry, Separation, 33-1 (2013) p. 8-12.

Fischer B., Teutenberg T., Development of a Raman Detector for hyphenation with high-temperature liquid chromatography and isotope ratio mass spectrometry, HTC-12, Site Oud Sint-Jan, Bruges (Belgium), Feb 1-3 (2012).

Fischer, B., Entwicklung eines empfindlichen Raman-Detektors für die Flüssigchromatographie, ANAKON 2013, Essen (Germany), Mar 4-7 (2013).

Technical Note

Low Dark Current Deep-Depletion (LDC-DD) Technology

A new standard for low-light NIR Spectroscopy

Standard back-illuminated, deep-depletion (BI-DD) CCDs offer quantum efficiencies (QE) up to 95% in the near-infrared (NIR) This makes them the detector of choice for photoluminescence, Raman or plasmonics spectroscopy in the 700 - 1,100 nm range. One disadvantage of deep-depletion devices has been a significant associated increase in dark current (~100 times) compared to standard back-illuminated, visible-optimized CCDs. A new generation of Low Dark-Current, Deep-Depletion (LDC-DD) CCDs now overcomes this limitation, and challenges the need for liquid-nitrogen (LN_2)-cooling for photon-starved NIR spectroscopy.

Introduction

Dark current is a source of noise inherent to CCDs. It arises from thermally generated charges in the silicon lattice over time. Cooling is the most efficient means of reducing dark current in CCDs, and there are a number of methods (incl. combinations) traditionally used, such as air, liquid coolant, liquid nitrogen (LN_2) and thermoelectric (TE).
A new generation of back-illuminated, deep-depletion CCDs (LDC-DD) now offers excellent dark-current characteristics whilst offering >95% QE in the NIR. This technical note analyses the benefits of this technology by considering the influence of temperature on quantum efficiency (QE) and dark current. It also aims to show that 'cooler is not necessarily better', and that the combination of LDC-DD and TE-cooling obsoletes the need for LN_2 cooling technology for BI-DD CCDs.

Back-illuminated, deep-depletion (BI-DD) – the attraction of high NIR QE

The QE of a CCD is governed by its ability to absorb incoming photons in the photosensitive silicon region. It is only in this region that photons are converted into electron-hole pairs, which are then confined by means of electric fields into a 'pixel'. The charges held in those pixels can then be transferred and detected.

Shorter wavelength photons (blue light) are absorbed close to the silicon surface, while longer wavelength photons can travel deeper into the silicon matrix before being absorbed. Photons above 1.1 µm do not have enough energy to create a free electron-hole pair that could be detected: a silicon CCD is effectively transparent at these longer wavelengths.

Fig. 1 shows the absorption depth of photons as a function of wavelength in crystalline silicon.

In front-illuminated CCDs, incoming photons must first transverse a polysilicon electrode structure and a silicon oxide (SiO) insulating layer (see Fig. 2). The electrode structure can absorb and reflect part of the incoming photon flux before it reaches the ~ 15 µm thick photosensitive region. This absorption is extremely pronounced in the ultraviolet (< 350 nm), but also limits the peak QE of such devices to around 50% in the visible.

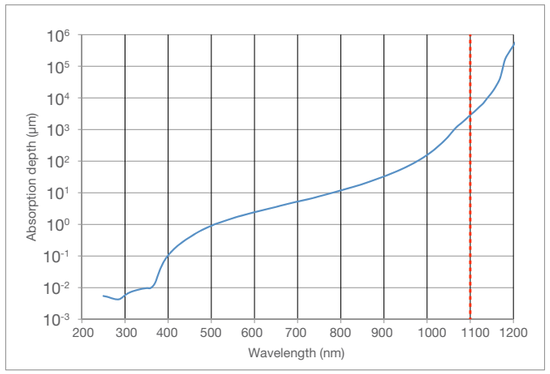

Figure 1: Absorption depth in Silicon at 300K as a function of incident photon wavelength[1]

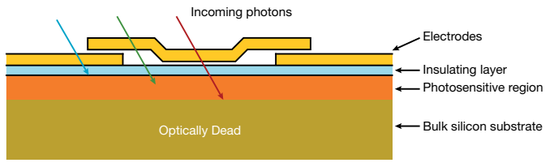

Figure 2: Typical front-illuminated CCD (cross section)

In order to eliminate the losses incurred at the front surface, a back-illuminated (BI, Back-thinned) configuration can be adopted. When a device is back-thinned, the bulk substrate is removed by mechanical grinding and chemical etching so that light can enter from the back surface directly into the active photosensitive region. These devices can exhibit peak QE of up to 95% with appropriate anti-reflection (AR) coatings.

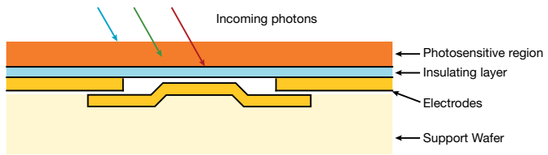

Figure 3: Typical back-illuminated CCD (cross section)

NIR QE of standard back-illuminated CCDs can be further enhanced by the use of a thicker photosensitive region (typ. 30-50 µm) and higher resistivity material.

- The thicker photsensitive region offers a greater absorption path to longer wavelength photons, and subsequently lowers the probability for these photons transversing the whole way across the active region (refer to Fig. 1).

- The higher resistivity material allows the electric fields, created by applying voltages to the electrodes, to penetrate the entire depth of the now thicker photosensitive region and hence better collect and confine photoelectrons within the pixels.

These devices are known as back-Illuminated, deep-depletion (BI-DD) CCDs.

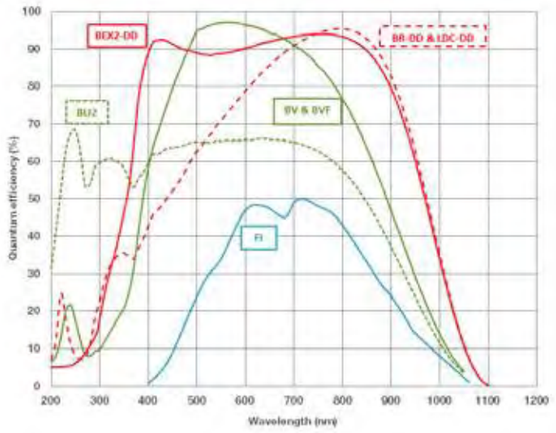

Figure 4: Typical QE performance at +25ºC of front-illuminated ('FI'), back-illuminated visible-optimized ('BV'), UV-enhanced silicon back-illuminated ('BU2') and back-illuminated deep-depletion CCDs with NIR AR-coating ('BR-DD') and broadband dual AR-coating ('BEX2-DD'). The new BI 'LDC-DD' and 'BR-DD' have identical QE characteristics.

Influence of CCD cooling on QE

The absorption depth of photons in the silicon can increase with cooling[1]. This is especially pronounced in the near-infrared, and effectively means that the CCD becomes increasingly transparent to NIR photons. This lower probability of absorbing a NIR photon translates into a decrease in QE (see Fig. 5).

BI-DD CCDs present the best QE in the 750 – 1,100 nm region, up to 95%, but this also means that they are the most prone to QE variation with cooling temperature. This is a consequence of band-gap shifting. At an illustrative wavelength of 950 nm, the probability of an incoming photon generating a detectable photoelectron in the photoative layer of a CCD can drop by up to 50%.

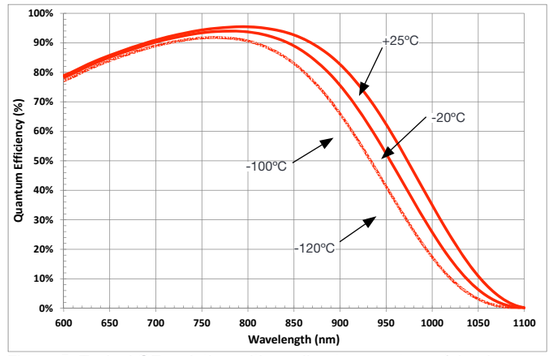

Figure 5: Typical QE variation with cooling temperature of back-illuminated, deep-depletion CCD with NIR-optimized AR coating. Data supplied by sensor manufacturer [2]

	-20°C	-70°C	-100°C	-120°C
Relative QE drop from +25°C	16%	34%	44%	50%

Since a CCD must first collect the incoming photons before detecting the associated photo-electron(s) generated in the active silicon region of the sensor, any decrease in QE must therefore be weighed against the actual dark current improvement benefit for a given experimental scenario.

The following section will focus on the impact of cooling on dark current alone for both standard BI-DD and the new BI LDC-DD technology. The effect on signal-to-noise performance – combining the influence of both QE and dark current variation influence - will be examined subsequently.

Dark current in back-illuminated, deep-depletion CCDs: 'NIMO' vs 'IMO' design

In order to better understand the limitation in dark current for current deep depleted devices it is first necessary to understand some concepts regarding CCD structure and how these influence dark current behaviour.

Scientific CCDs are usually manufactured on epitaxial silicon with a thickness of the order of ~15 µm. A typical CCD is made up of pixels which are defined by the permanent channel stops in one direction and by the image phases in the perpendicular direction. (see Fig. 6).

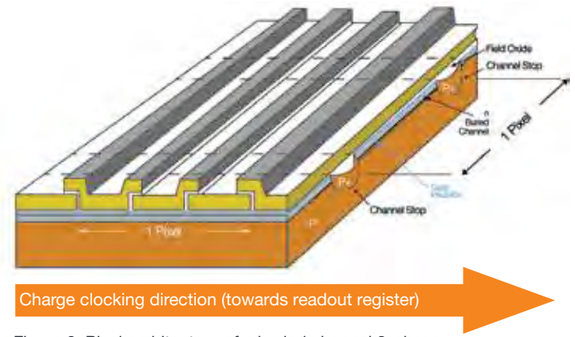

Figure 6: Pixel architecture of a buried channel 3-phase

The image phases are electrode gates that run across the outer surface with the photosensitive region below. Applying a voltage to an electrode gate depletes the region below of electrons producing a potential well often referred to as the 'depletion region'. It also causes any charge to gather under the nearest most positive (in voltage) phase and by controlling when this voltage is applied, we can define individual pixels and transfer them, on mass, accross the CCD area and into the readout register.

Non-inverted mode operation (NIMO) CCDs

At all times at least one of the gate electrodes must be low while the other(s) are high, even during transfer. This is to ensure that charge in one pixel is not mixed with charge from its neighbouring pixels. Electronically this is not a problem to arrange, and is generally referred to as 'clocking'. This configuration is referred to as Non Inverted Mode Operation (NIMO) (see Fig. 7)

However it turns out that about 100 times more dark current is generated when any image clock is held high compared to low. This can lead to a substantial build-up of dark signal during long integrations.

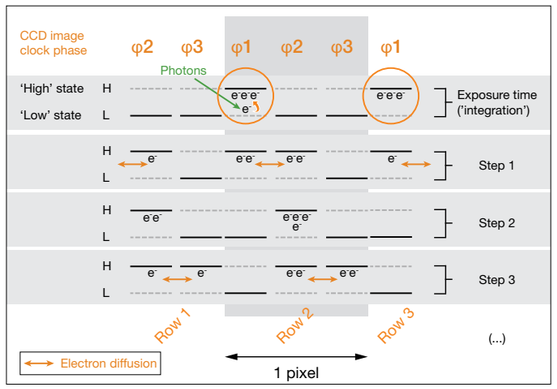

Figure 7: Electron signal shifting in 3-phase 'NIMO' CCDs (image area row clocks). Most of the dark current is generated when the image clock (**φ**1) is held high during CCD exposure (circled). Photoelectron transfer is achieved by 'toggling' sequentially the image clocks **φ**1, **φ**2, **φ**3)

The origin of this dark current are defects in the interface between the oxide insulating layer and the silicon. These defects are a source of electrons into the conduction band. These electrons are trapped but can be thermally excited, making dark current very temperature dependent.

Inverted mode operation (IMO) CCDs

By keeping the clock level sufficiently low, holes from the channel stops can be attracted into this interface and 'neutralize' the electron sources. When this state is reached it is referred to as 'pinning'.. Further lowering of the phase potential will have no effect inside the silicon simply because more holes arrive to pin the voltage, hence the name.

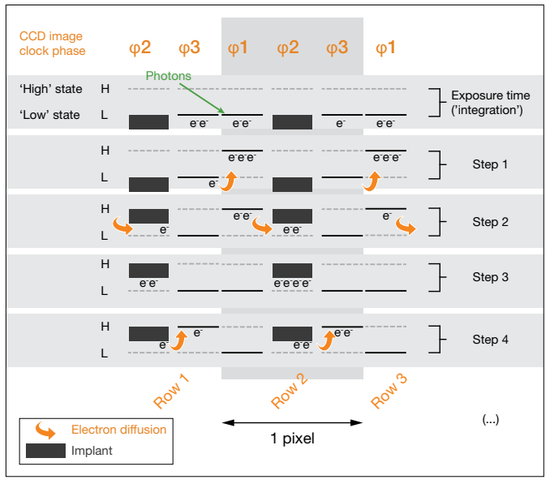

Figure 8: Electron signal shifting in 3-phase 'IMO' CCDs (image area row shift). Implants are inserted below one of the image clocks (**φ**2) to allow setting of image phases voltage low during CCD exposure time and keep dark current under control

Adding an implant below one of the electrode gates will generate a small voltage step which acts as a barrier between pixels even when all the electrodes are low, i.e. during the integration period. The device can still be clocked successfully, as the large clock amplitudes can easily overcome the smaller implant offset and thus the charge can still be read out (see Fig 8). This technology is referred to as Inverted Mode Operation (IMO) or Multi Phase Pinning (MPP), another version of this which has the same effect is called Asymmetric IMO (AIMO).

Low Dark-Current Deep-depletion (LDC-DD) Technology

Fig. 9 shows the dark current characteristics versus cooling temperature of a standard back-illuminated, deep-depleted CCD (dotted orange line) and the new BI LDC-DD CCD (red line).

At an equivalent pixel size of 15 µm, the LDC-DD shows a significant 10 times dark current performance improvement when compared to a standard deep-depletion CCD.

LDC-DD dark current performance at the lowest cooling temperature is almost identical to standard 'AIMO' CCDs.

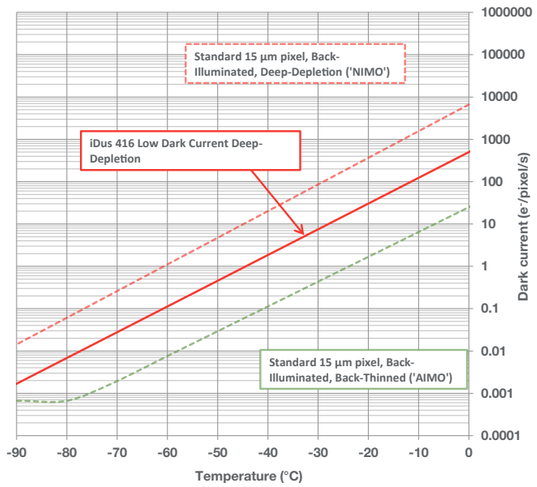

Figure 9: Dark current versus temperature for traditional back-illuminated, deep-depletion CCD (dotted orange), standard back-illuminated visible-optimized CCD (dotted green) and the new back-illuminated LDC-DD CCD (solid red)

The disadvantage of the elevated dark current on standard deep-depleted devices has meant a compromise has to be made: either improved NIR QE response and higher dark current or lower QE response and low dark current.

The reason for this higher dark current has been the inability to 'pin' a deep-depleted CCD device. To date neither IMO nor AIMO have been available in conjunction with deep depletion, since inverting (or pinning) the surface during integration reduces the voltage available. This therefore restricts depletion, limiting the advantage of a high resistivity substrate.

However we at Andor have partnered with E2V in order to overcome this restriction, and bring the groundbreaking back-illuminated LDC-DD technology to the Academic and Industrial world to greatly facilitate photon-starved spectroscopy acquisition in the NIR. This virtually obsoletes the very inconvenient and unpractical LN_2 cooling approach (compared to maintenance-free thermo-electric (TE) cooling).

Signal-to-noise (S/N) – true basis for detector sensitivity assessment

Signal-to-noise is an essential tool for assessing the combined effect of QE and noise variation in CCDs. It is the achievable signal-to-noise which is of key importance when assessing the performance of any detector in terms of its sensitivity. For CCDs, it can be defined as follow:

(a) $$S/N = \frac{S}{\sqrt{N_{RN}^{\ 2} + N_{DN}^{\ 2} + N_{CIC}^{\ 2} + N_{SN}^{\ 2}}}$$

Where S is the photon signal, NRN the readout noise, NDN the dark noise, NCIC the spurious charge noise or clocking-induced discharge and NSN the incoming signal shot noise. It can also be expressed as:

(b) $$S/N = \frac{QE.I.t}{\sqrt{N_{RN}^{\ 2} + DC.t + N_{CIC}^{\ 2} + QE.I.t}}$$

Where QE refers to the sensor quantum efficiency (%), I the incoming photon flux (photons/s), t the exposure time (s) and DC the dark current (e-/pix/s or e-/CCD column/s).

Since CCD cooling impacts both dark current and sensor QE, one must consider the following:

1. Is there some temperature point in cooling beyond which further cooling may be detrimental to the overall performance in terms of S/N, i .e. is there a point where the reduction in QE is more influential than further reduction in the dark current ?
2. What is the trade-off between the influences of the reduction in QE and the reduction in dark current noise, with cooling for a given sensor?

LDC-DD technology - achieving high signal-to-noise for much shorter exposures

The following scenarios look at a SNR performance in the context of spectroscopy, where the signal is vertically binned in a number of rows on the CCD. The impact of the lower dark current of the LDC-DD technology on SNR is shown on Fig. 10.

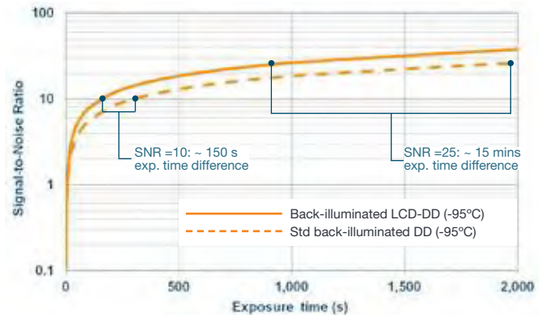

Figure 10: SNR performance of back-illuminated LDC-DD vs standard back-illuminated, deep-depletion. Very low photon flux scenario of 1 photon per binned area per second (or 1 photon per 15 µm pixel every 2 minutes) at a wavelength of 850 nm. Binned area is 15 µm wide x 2 mm high, and cooling temperature is -95ºC for both CCDs

Both technologies can achieve good SNR performance. However, the back-illuminated LDC-DD provides equivalent SNR at much shorter CCD exposure times.

In the scenario above, the back-illuminated LDC-DD CCD will achieve a good SNR of 10 with an exposure time of nearly 2 minutes shorter. For a SNR of 25, this difference is ~15 minutes.

TE-cooling and LDC-DD technology: achieving the best performance without the inconvenience of LN_2

Liquid nitrogen-cooled CCDs typically operate at -120°C, and have been considered as the standard for photon-starved NIR spectroscopy applications for decades.

Modern TE-cooled CCDs can achieve -100°C, while offering great advantages:

- Maintenance-free operation - no need for regular LN_2 refilling and associated safety concerns - ideal for 24/7 industrial applications
- Transportability - ideal for integration into modular instrumentation
- Lasting performance – sensor sits in vacuum and is protected from any degradation that could result in loss of QE
- Low cost

Fig. 11 shows a very challenging photon regime, and compares the SNR performance of an LN_2-cooled BI-DD CCD at -120ºC with a back-illuminated LDC-DD CCD TE-cooled to -95ºC.

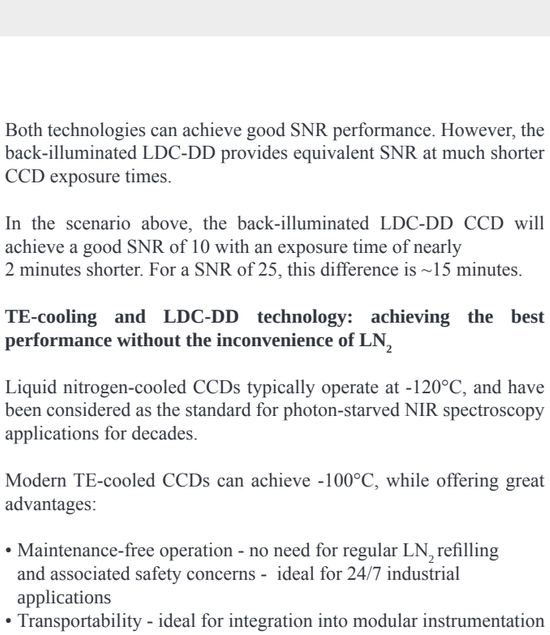

Figure 11: (a) SNR performance of back-illuminated LDC-DD (TE-cooled at -95ºC) vs standard back-illuminated, deep-depletion (LN_2-cooled at -120ºC). Very low photon flux scenario of 1 photon per binned area per second (or 1 photon per 15 µm pixel every 2 minutes) at a wavelength of 850 nm. Binned area is 15 µm wide x 2 mm high (b) Details of the lower CCD exposures region.

In this extreme light level scenario, SNR performance between the two technologies is identical for exposure times greater than ~ 30 s). At shorter exposure times, the difference in SNR at a given exposure time is less than 10%, which is minimal.

At higher photon flux, the trend is even more pronounced, with an even closer match at the shortest exposure times.

Conclusion

In conclusion: with the combination of -95ºC TE cooling and back-illuminated LDC-DD technology, the highest detection performance in the NIR can be achieved even at an extremely challenging photon flux. At higher photon flux, this technology combination will exceed the performance of standard -120ºC, LN_2-cooled back-illuminated BI-DD CCDs. So when looking for the best NIR sensitivity and the most convenient cooling means, Andor's iDus 416 -95ºC TE-cooled platform with back-illuminated LDC-DD CCD technology has no equivalent.

LCD-DD optical etaloning

Optical etaloning is an important point to be mindful of when working with back-illuminated CCDs in the NIR. The back-illuminated LDC-DD CCD benefits from a fringe-suppression process implemented during sensor manufacturing, which helps to 'break' the Fabry-Pérot étalon formed by the reflections in the CCD depletion region. The maximum peak-to-peak fringing modulation typically varies from 1-5%: these variations are inherent to the manufacturing process at CCD batch level. Refer to Andor technical note "Optical Etaloning in Charge Coupled Devices (CCDs)" [3] for further details on optical fringing in CCDs.

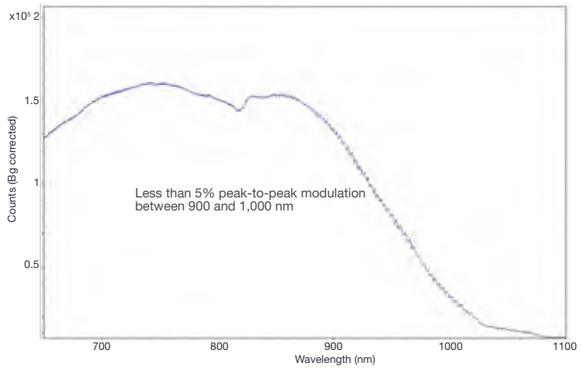

Figure 12: Full Vertically Binned (FVB) spectra of a broadband tungsten source acquired with an iDus 416A-LDC-DD and a Shamrock 750 spectrograph

References

[1] Green, M.A. and Keevers, M. "Optical properties of intrinsic silicon at 300 K ", Progress in Photovoltaics, p.189-92, vol.3, no.3 (1995)

[2] e2v website link: http://www.e2v.com/products-and-services/high-performance-imaging-solutions/imaging-solutions-cmos-ccd-emccd/qe-curves/

[3] Andor Technology application note, "Optical Etaloning in Charge Coupled Devices (CCDs)" www.andor.com

LDC-DD technology in summary

- >95% peak QE in NIR
- 10x lower dark current than traditional BI-DD CCDs – achieves high SNR at shorter exposure times
- Less cooling required = better NIR QE
- Same dark current than standard back-illuminated, visible-optimized CCDs
- Superb MTF performance due to the full depletion of the entire photosensitive area
- Low optical fringing

Andor's iDus 416A-LDC-DD also offers:

- 2000 x 256 array - 30 mm wide sensor for extended band-pass capture
- 15 µm pixels for high resolution spectroscopy
- -95ºC Thermo-Electric cooling –maintenance-free
- Ultravac™ vacuum technology for lasting superb detection performance

Appendix A

Key spectroscopy sensor flavours and platforms by Andor Technology

Andor sensor code	Description	Wavelength range (nm)	Peak QE	Fringe supression process	Peak modulation amplitude	Dark current	Andor platform
FI	Front-illuminated	400 -1,100	58% @ 770 nm	Not necessary	0%	Very low	iDus 401, Newton 940, Newton^{EM} 970, Newton^{EM} 971
OE	Open electrode	<200 – 1,100	58% @ 770 nm	Not necessary	0%	Very low	iDus 420, Newton 920
BV	Back-illuminated, Visible-optimized AR coating	<200 – 1,100	97% @ 550 nm	No	20-40% (850 – 900 nm)	Low	iDus 420, Newton 920, Newton 940, Newton^{EM} 970, Newton^{EM} 971
BVF	Back-illuminated, Visible-optimized AR coating	<200 – 1,100	97% @ 550 nm	Yes	10-20% (850 – 900 nm)	Low	iDus 401, iDus 420, Newton 920, Newton^{EM} 970
BR-DD	Back-illuminated, deep-depletion NIR-optimized AR coating	<200 – 1,100	95% @ 800 nm	Yes	1-5% (~ 950 nm)	High	iDus 420, Newton 920
BEX2-DD	Back-illuminated, deep-depletion Broadband, dual AR coating	300 – 1,100	93% @ 800 nm 92% @ 420 nm	Yes	1-5% (~ 950 nm)	High	iDus 420, Newton 920
LDC-DD	Back-illuminated, deep-depletion NIR-optimized AR coating	<200 – 1,100	95% @ 800 nm	Yes	1-5% (~ 950 nm)	Low	iDus 416

Appendix B

Estimates for cost/time analysis with Liquid N_2 cooling.

LN_2 cooling does involve added overheads in terms of raw material and handling costs, as well as the inconvenience with handling and associated health and safety considerations. Outlined here is a simple estimate of the costs for supply of LN_2 to cool the CCD camera over a period of five years.

	Estimates
Liquid nitrogen volume to fill the detector	1L
Volume requirements per week (incl evaporation wastage)	10L
Volume requirements per year (over 10 months)	400L
Nitrogen Dewar 25 litre – Monthly rental	€ 28
Cost per litre – small volumes (<50 L)	€ 2.90
Cost per litre – large volumes (>50 L)	€ 2.30
Cost for 25 litre liquid nitrogen Dewar refill + delivery cost	€ 120
Cost of liquid nitrogen per year based on 16 x 25 litre refill	**€ 1,920**
Costs of liquid nitrogen supply over 5 year period	**€ 9,600**
Initial capital expenditure on 25 litre Dewar, handling/protective tool	€ 1,500
Estimated cost of LN_2 over a period of 5 years	**€11,000**

As can be seen from the estimates in the table the costs of supply and handling of liquid nitrogen will be quite substantial over the working life of any LN_2 cooled camera.

Technical Note

Sensitivity of CCD cameras – some key factors to consider

Sensitivity is a key performance feature of any detection system. When assessing the sensitivity of any CCD sensor it is the achievable Signal-to-Noise Ratio (SNR) which is of key importance. This encapsulates the capacity to have the signal stand out from the surrounding noise.

The approach to ensure the best possible SNR ratio is to a) develop a sensor with the highest possible quantum efficiency and b) reduce the various sources of noise to a minimum. Quantum Efficiency (QE) is related to the ability of the sensor to respond to the incoming photon signal and the conversion of it to a measurable electron signal. Clearly the greater the number of photoelectrons produced for a given photon signal the higher the QE. QE is usually expressed as a probability – typically given in percentage format – where for example a QE of 0.6 or 60% indicates a 60% chance that a photoelectron will be released for each incident photon. QE is a wavelength or photon energy dependent function, and a sensor is generally chosen which has the highest QE in the wavelength region of interest. Various means have been employed to improve the quantum efficiency of CCD sensors. These include:

- Back Illumination – where the sensor is back-thinned and the light is delivered through the back making it easier for the incident photons to reach and be absorbed in the active layer of the sensor
- Anti-reflection coatings – optimized for the particular wavelength region of interest
- Deep-depletion – where the active layer is increased in extent to increase probability of absorption of photons in the near-infrared (NIR) part of the spectrum
- Lumogen coatings – to enhance the sensitivity in the UV region by the absorption and conversion of UV photons to visible photons which are more readily detected by the CCD
- Micro-lenses – more relevant to imaging sensors than Spectroscopy – allows more light to be collected into the sensitive area of the sensor leading to an increase in the fill-factor

The next key challenge is reducing the overall noise to its minimum (the latter is often referred to as the noise floor). Shot noise within the photon generated (electronic) signal (S) is an intrinsic contribution to the overall noise and is related to fundamental quantum physics; it will always be part of any signal. If the number of photons in the incident signal is denoted by P and the quantum efficiency by QE, the photoelectron signal generated will be given by S = (QE.P). Next to consider is the system or camera noise which has three main contributors, the dark current (DC) of the sensor, spurious charge such as clock induced charge (CIC), and the readout noise from the output electronics (pre-amp and A/D node). The sources of noise and the means of dealing with them are summarized below:

- Signal Shot Noise (N_{SN}) – fundamentally intrinsic to any signal $N_{SN} = \sqrt{S} = \sqrt{(QE.P)}$
- Dark noise (N_{DN}) – associated with the thermally generated dark current $N_{DN} = \sqrt{(DC.t)}$ – where 't' corresponds to the exposure time: dark current (DC) is reduced by cooling of sensor
- Clock Induced Charge Noise (N_{CIC}) – spurious noise generated during the clocking of the pixels when moving the charge out of the sensor; this is minimised by implementation of fine tuned and well controlled clocking voltages, in particular fine control over clocking edges down to nanosecond resolutions
- Readout Noise (N_{RN}) – this arises in the readout electronics before the digitized signal is sent to the PC and may be reduced by using lower readout rates and clean clocking pulses

Usually a high performance camera is operated at certain temperatures and clocking speeds such that the detection limit is determined by the readout noise. The various sources of noise may be added in quadrature to give the overall system or camera noise which may be expressed as:

$$System_Noise = \sqrt{N_{RN}^{\ 2} + N_{DN}^{\ 2} + N_{CIC}^{\ 2}}$$

The system noise characteristics for a typical iDus – BRDD CCD camera are shown in figure 1. Clearly the dark noise will rise with increase in exposure times such that for long exposures the overall system noise (and consequently the detection limit) will become dominated by the dark noise contribution. With cooling, the dark noise contribution is reduced significantly and with sufficient cooling can be reduced to an insignificant level. This shows up as the plateau region where the system noise is now readout-noise limited. The advantage of cooling is evident when extremely long exposure times (>10's, if not 100's of seconds) are required in a given experiment. However, if short exposure times are being used, then it is clear that there is little benefit in using ultra deep cooling. As an illustration, consider exposure times less than 1000 seconds (a long exposure time). There is little or no advantage cooling the sensor below -75ºC, where the system is operating on the low plateau corresponding to the read out noise limited regime. Similarly, if exposures less than 10s are being used, there is little or no benefit to be gained by cooling below -50ºC. When the temperature dependence of the QE is considered then one has to be careful when choosing the best operating point or temperature for optimum performance particularly if working in the NIR region (see Technical note page 52-53).

The overall signal to noise (SNR) for a given CCD system may be expressed in the form:

$$SNR = \frac{QE.P}{\sqrt{N_{RN}^{\ 2} + N_{DN}^{\ 2} + N_{CIC}^{\ 2} + N_{SN}^{\ 2}}}$$

This function enables the performance of any conventional CCD to be assessed given the values for the key parameters – usually contained in the specification or performance sheets.

A number of points worth noting are,

- the QE has some temperature dependence which has particular implications when working in the NIR region – simply cooling a sensor to the lowest possible temperature does not necessarily ensure optimum performance of the camera
- the demands on cooling are somewhat reduced when using short exposure times (<1 s)
- deep-cooling is required for longer exposures (>10 s)

Advanced detectors have been developed to extend sensitivity to the level of detecting a single photon. These systems amplify the initially detected signal using a multiplication process leading to an enhanced S/N at the read out of the CCD. The two main technologies are:

- ICCD – intensified charge couple devices where an intensifier tube is added in front of a standard CCD camera; the intensifier uses a Micro-Channel Plate (MCP) to provide the amplification of the signal before detection on the CCD
- EMCCD – Electron Multiplication (EM) charge coupled device which uses a sensor with a special read out register; the EM register amplifies the electronic signal using a process know as ion impact ionisation

The degree by which a basic signal is amplified or multiplied is referred to as the gain factor. This can be selected through the software and leads to alteration of the voltages across the MCP in the case of the ICCD and the clocking voltages applied in the EM read out register of the EMCCD.

When an EMCCD or ICCD is being used an additional source of noise must be taken into account which is associated with the amplification process itself; this variation is intrinsic to any multiplication process. This is quantified by what is termed the Noise Factor (F). For EMCCD cameras the noise factor is √2 or ~1.41. The noise factor in ICCDs depends on the type and quality of intensifier tube used: these can have values from ~1.6 to ~3.5. Taking the noise factor (F) and the actual or real gain (G) into account, the total noise for systems offering gain may be expressed as:

$$Noise(EM, ICCD) = \sqrt{N_{RN}^{\ 2} + G^2.F^2.\left(N_{DN}^{\ 2} + N_{CIC}^{\ 2} + N_{SN}^{\ 2}\right)}$$

The SNR ratio for an EMCCD or ICCD may be written as:

$$SNR = \frac{QE.P}{\sqrt{\left(\frac{N_{RN}}{G}\right)^2 + F^2.\left(N_{DN}^{\ 2} + N_{CIC}^{\ 2} + N_{SN}^{\ 2}\right)}}$$

When high performance systems are operated in a deep cooled low-noise regime, where dark and spurious noise are negligible compared with the read out noise, this expression for the SNR may be simplified to:

$$SNR = \frac{QE.P}{\sqrt{\left(\frac{N_{RN}}{G}\right)^2 + F^2.\left(N_{SN}^{\ 2}\right)}}$$

It can be seen here that by increasing the gain G, the term involving the read-out noise, N_{RN}, becomes insignificant compared with the intrinsic shot noise of the signal, leading to ultra-sensitive detection capability. EMCCD and ICCD systems operated with appropriate configurations with sufficiently high gain can be used for single photon counting type experiments.

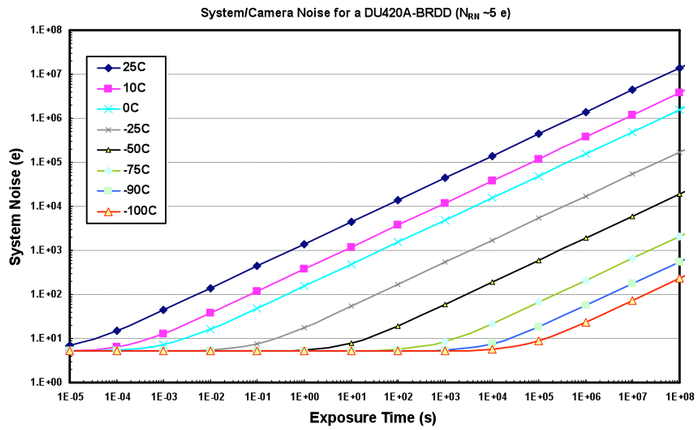

Figure 1: The detection limit as a function of exposure time for single pixel (imaging mode) which are read out at 33 kHz with readout noise of 4.6 electrons.

Technical Note

LN_2 versus TE cooling for BRDD and InGaAs sensors

A widely made assumption when looking for the best performance from a CCD detector is 'the cooler the better'. An intrinsic source of noise within all CCD detectors is that associated with thermally generated 'dark current'. Cooling is clearly the means of reducing this particular noise source.

However, it is also very important to remember than the quantum efficiency (QE) has a temperature dependence, and in this case the QE actually gets worse with cooling. This is a very important consideration for some detectors when operated in certain spectral regions, where extending the deep cooling to ever lower temperatures can lead to non-optimized operation of the system; that it to say there exists some temperature beyond which further cooling can be a disadvantage. One such case is a back-illuminated deep-depletion (BRDD) sensor used in the NIR region from 750 nm to 1000 nm.

The sensitivity of the fall-off in QE with cooling is depicted in figure 1 for a BRDD sensor. As can be seen the fall-off is quite dramatic and at the illustrated wavelength of 950 nm, the QE falls in relative terms by ~40%. This clearly arises a question around the trade-off between cooling to minimize dark noise and the desire to have QE as large as possible. To assess if there is an optimum temperature region for a given set of experimental conditions and what that temperature might be, it is useful to assess the SNR ratio possible at different temperatures of the sensor. The SNR ratio is the key parameter in any discussion on sensitivity.

If we consider the system or camera noise as summarized in the equation below and illustrated for a typical BRDD sensor in figure 1 on page 51, then it is desirable to be operating at the noise floor (plateau at base of curves). But if we are working with exposures <1 s, as an illustrative example, we could work at a range of temperatures between -50ºC and -100ºC and still be operating at the detection limit.

$$System \quad Noise = \sqrt{N_{RN}^{\ 2} + N_{DN}^{\ 2} + N_{CIC}^{\ 2}} \ .$$

However, when the QE is considered, it will be found that a better SNR will be possible for these exposures when operating at temperatures towards the upper end of this range i.e. around -50ºC.

The SNR is shown in figure 2 for a low level photon flux of 10 photons/pixel/second at wavelengths around 950 nm falling on a BRDD sensor. Generally as the sensor is cooled the SNR improves but interestingly at the lower temperatures the SNR is better at -75ºC than at -90ºC. This is indicative of the influence of the fall in QE and consistent with a transition point in the region of -70ºC to -90ºC where further cooling is disadvantageous to the overall sensitivity.

The SNR characteristic is shown for this particular sensor being read out at the slowest rate of 33 kHz but the same trends apply for the characteristics if operating with the higher readout speed of 100 kHz with readout noise of ~16 e^-. It is also important to note that even with longer exposure times the same trend is maintained and at no point does the deeper-cooled SNR exceed that at -75ºC. In addition, when dealing with stronger photon fluxes the SNR characteristics will be even more favourable to that of -75ºC compared with -100ºC. The inset in figure 2 shows in greater detail the SNR curves for short exposure times.

From this example of working in the NIR region the degree of cooling must be considered carefully to ensure optimum performance in terms of SNR. In the case of the silicon-based BRDD sensor, ultra deep cooling as provided by liquid nitrogen can be a clear disadvantage when compared with deep-cooling in the -70ºC to -90ºC region. Thermo Electric (TE) cooling not only satisfies these requirements in a well controlled manner, but also avoids the inconvenience, cost and safety implications of working with liquid nitrogen systems.

Deep cooling InGaAs sensors – important implications

Just as ultra deep cooling does not guarantee optimum performance for a conventional silicon based CCD sensor, there are analogous implications for the ultra deep cooling of InGaAs sensors. As InGaAs sensors tend to be thermally noisier than their silicon counterparts, deep cooling, as supplied by TE and LN_2 cooling systems, is of more critical importance. However, there are two key factors which are often overlooked when deciding on the requirements for the optimum performance of an InGaAs system. These are:

a) influence of the background ambient blackbody radiation
b) shift in the bandgap edge with cooling

Figure 3 shows dark signal characteristics for the cooling of an iDus InGaAs (DU490A-1.7) array. These curves show the expected decrease in dark signal as the sensor gets cooler but they tend to flatten out into a plateau region beyond which further cooling of the sensor produces little or no improvement in the dark signal. A TE Peltier cooler is used to cool the sensor for the reduction of the thermally generated dark signal and a liquid coolant flowing through a copper block is used to remove heat from the warm end of the Peltier cycle. Consequently for these test measurements the coolant determines the ambient temperature i.e. the temperature of the camera housing (including window) surrounding the sensor. The characteristic curves for different coolant temperatures show that the dark charge becomes limited by the ambient blackbody radiation from the surroundings. In practice the blackbody radiation which can enter directly through the window from the surroundings will also be added to the overall background radiation.

There is a limit to which the camera body and window can be cooled. It has to remain above the dew point, otherwise moisture will condense on the window and camera electronics. The dew point is typically between 10ºC and 15ºC (depends on climate/lab conditions) and as can be seen from the characteristic for coolant at 10ºC, the sensor needs cooled to just below -70ºC to enter the plateau region; this is well within the capacity of TE cooling. To ensure optimum performance from these InGaAs cameras, it is strongly recommended that liquid coolant is used to enable operation just above the dew point.

Secondly, one has to be careful when measuring signals near the upper cut-off wavelength. As for silicon, cooling causes a shift in the energy of the bandgap edge; this leads to a shift in the cut-off wavelength. In InGaAs, increased cooling causes a striking shift of this cut-off towards shorter wavelengths. Figure 4 shows relative QE curves at several temperatures for the InGaAs sensor as used in the iDus DU490A-1.7 camera. This effect results in a shift dependence of ~0.6 nm/K that leads to a shift of ~70 nm to shorter wavelengths when cooling down to -100ºC. This effect is of extreme importance if one is working in the wavelength region around 1.6 µm.

As with BRDD sensors working in the NIR region, one must consider carefully the degree of deep-cooling and the ability to control it, when ensuring optimum performance of an InGaAs system in terms of SNR. If using short to medium exposure times then TE cooling is more than adequate as long as the system is operating in a regime where the background dark signal is 'ambient-blackbody-radiation' limited. The latter is ensured with liquid coolant such that the camera is operated just above the dew point. If working at the upper end of the sensor's wavelength sensitivity, e.g. around 1.6 µm, the accurate controllability of temperature will be a distinct advantage for optimization of sensitivity.

Figure 1: The relative change in QE for the BRDD sensor between 25°C and -90°C.

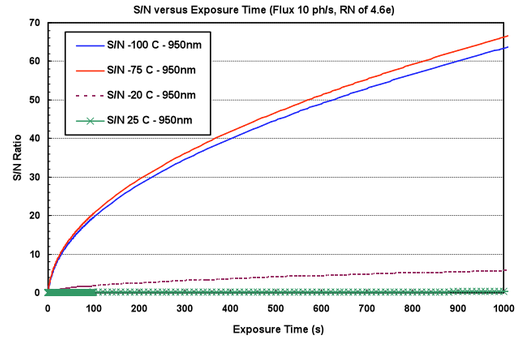

Figure 2: SNR versus exposure time for a low light photon flux of 10 ph/pix/s (950 nm) incident on the pixels of a BRDD sensor. The readout noise corresponds to the slowest rate of 33 kHz with a readout noise of 4.6 e^-.

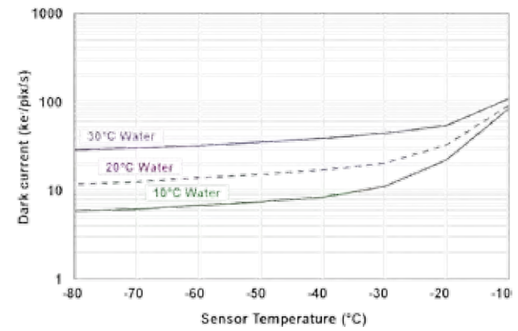

Figure 3: Dark signal characteristics for an InGaAs iDus camera where the dark signal depends on both the sensor temperature and the ambient blackbody radiation. The dark signal of the sensor is plotted at different temperatures for different ambient temperatures i.e. temperatures of the front end of the surrounding camera housing. The flat plateau regions correspond to background blackbody radiation limited detection.

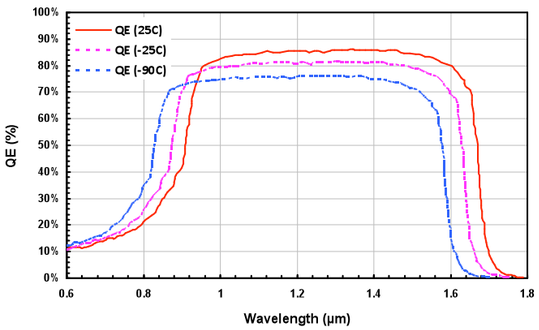

Figure 4: Variation of the relative QE of an InGaAs sensor with cooling. The solid curve is experimentally measured data at ambient (25ºC). The broken curves are modelled data based on both experimental measurements and theory, which indicated a shift in the band edge towards higher energies of ~0.75 nm/K and a drop in peak QE of the order of 0.1 %/K, with fall in temperature.

Technical Note

EMCCD technology for Spectroscopy

Electron Multiplication (EM) technology has been one of the most important developments in light detection over the last decade. It has revolutionized the whole area of low-light Spectroscopy and imaging, enabling research that hitherto would not have been possible. EM on the CCD chip allows for the amplification of the captured electron signal before it is ever read out through the camera electronics resulting in reduction of the effective readout noise to sub-electron levels.

Sensors implementing EM amplification offer ultra-sensitive detection down to the single photon level. The first and most powerful EMCCD camera for Spectroscopy – the Newton^{EM} – was introduced by Andor in 2005.

Other Andor cameras which implement EM sensors are the iXon3 and Luca^{EM} families which are used primarily for imaging applications though some are being used for Spectroscopy particularly where fast spectral rates are a prime requirement. The Newton^{EM} has the added versatility and flexibility of being usable as both a conventional CCD and as an EMCCD; it is effectively 'two-cameras-in-one' with one simple click in the software to switch between them.

EM technology comes into its own when operating in a low-light regime (typically <100 photon per pixel), where the added sensitivity offers obvious benefits. Such scenarios may arise when dealing with an intrinsically weak signal, when fast spectral rates are required with minimal exposure times, or in situations where the excitation energy has to be kept low to avoid damage to the sample under investigation. Figure 1 illustrates a comparison of a conventional CCD with an EMCCD where the spectral intensity has been deliberately delivered in a low photon regime with the use of neutral density filters. The experimental conditions were exactly the same apart from the application of EM gain. Increasing the gain pulls the spectral features out of the noise to be clearly visible (figure 1. bottom), features that would otherwise have remained buried in the noise floor of the conventional system (figure 1. top).

EM technology is implemented on the CCD sensor with the inclusion of a special readout register which takes the rows of pixel charge packets from the active area of the sensor and delivers them to the readout node electronics, whilst in the process causing the charge packets to be amplified i.e. the numbers of signal electrons is multiplied. The readout node consists of the pre-amplifier (Pre-Amp) and analog-to-digital (A/D) electronics which converts the analog signal to the digital representation in 'counts'. This digitized signal can then be sent to the computer for analysis. It is this readout node which gives rise to one of the most important sources of noise in the overall system – the readout noise (N_{RN}) – and in the highest performance detection systems often determines the ultimate detection limit or sensitivity of the camera. It is the effective overcoming of this readout noise where EM gain delivers its benefit.

The basic principle of EM technology is illustrated in figure 2. The sensor has two readout registers, a normal or conventional register and the EM register. The clocking voltages used on the EM register are higher than for conventional clocking. These higher voltages cause the electrons to acquire sufficient energy such that extra electrons are released by a process know as impact ionization; the increased charge package is stored in the next pixel along the chain. There is a small probability of this process actually creating additional electrons within the packet but with multiple elements or stages within the readout register significant overall gains are possible. Gains in the number of electrons up to factors of x1000 are possible – hence the term Electron Multiplication (EM).

The key advantage of on-chip-amplification before the readout node is to ensure the signal is not readout noise limited. Gain raises the signal well above the noise floor; the latter is largely determined by the readout noise of the system. An alternative way to think of this effect is in terms of the 'effective' readout noise. With increasing gain the effective readout noise can be decreased to the sub-electron level. Reduction in the overall noise is reflected in improved signal-to-noise (SNR) ratios and enhanced sensitivity. It is worth noting that further increase of the gain above the point where the effective readout noise is at its minimum level (< 1 electron), produces no improvement in the sensitivity. Indeed with very high gains it may serve to decrease the dynamic range of the system. The application of different gains is easily implemented through the software and results in fine adjustments of the clocking voltages in the readout register – higher voltages resulting in higher gain.

The SNR ratio is the key parameter in determining when EM gain will offer its advantages over the conventional CCD. There are four types of noise to be considered when considering the optimum SNR performance of any camera, those associated with the camera – dark current (N_{DN}), spurious or CIC (N_{CIC}) and readout noise (N_{RN}), and that associated with the signal itself – namely the signal shot noise (N_{SN}). An additional noise source must be taken into account when dealing with any multiplication or gain system such as with the EMCCD. This is encapsulated within what is called the noise factor (F) and for the EMCCD has a value of ~1.4, a value that is consistent with both theory and experimental observation. Denoting the EM gain by G, the quantum efficiency of the sensor by QE, the photon flux per pixel by P, and taking into account the noise factor, F, the SNR for the EMCCD can be expressed as:

$$SNR = \frac{QE.P}{\sqrt{\left(\frac{N_{RN}}{G}\right)^2 + F^2\left(N_{DN}{}^2 + N_{CIC}{}^2 + N_{SN}{}^2\right)}}$$

This reduces to the basic SNR equation for the conventional sensor with the gain G=1 and the noise factor F=1. Figure 3 shows SNR curves for the Newton^{EM} with low photon signals. The ideal curve corresponds to the ultimate noise limit of the signal shot noise. Several curves for different gains are included which show that increasing the gain is beneficial for the lower photon signals. The characteristic for the conventional CCD crosses over that of the EMCCD – with gain x 100 - at a signal of ~53 photons per pixel. This means that weaker signals below this transition point will benefit from EM gain, whereas for stronger signals above this level there is a better SNR with the conventional system. When the systems are operated at the fastest readout speed of 3 MHz, the readout noise is greater and the benefits of EM gain would be seen for even stronger photon signals up to just under 100 photons/pixel. It will be noted that as the photon signal increases, the SNR ratio for the conventional CCD approaches that of the ideal curve i.e. the noise becomes limited by the intrinsic shot noise of the signal. However, in the case of the EMCCD the SNR ratio approaches the ideal but will always have a systematic offset towards lower SNR; this offset is associated with the noise factor (F) of the gain register.

Application areas which benefit from EM technology

- Raman Spectroscopy
- Micro-Spectroscopy
- Multi-spectral Imaging
- Hyper-spectral Imaging
- Fast reaction processes
- FRET
- Single molecule Spectroscopy
- Transient (Pump-Probe) Spectroscopy
- Nano-dot Photoluminescence
- Organic Luminescence
- Atomic emission Spectroscopy
- Flow cytometry
- Electroluminescence

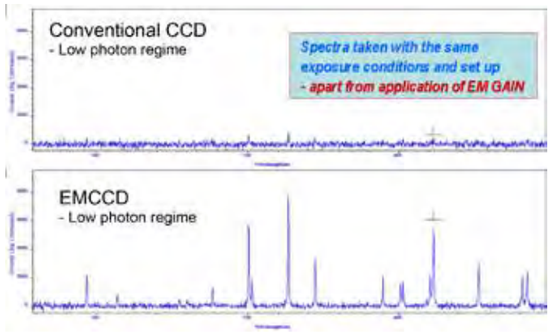

Figure 1: Comparison of the EMCCD with the conventional CCD for low light levels. Even the weakest spectral features can be observed with the application of EM gain which would otherwise remain obscured in the background noise of the conventional CCD. Both spectra taken under the same conditions apart from the application of gain. Data captured for a Newton DU971N-BV camera on a Shamrock 500i spectrograph using single scans with Full Vertical Binning (FVB).

When operated with very high gain and signals with ultra-low levels, an EMCCD can be used in 'photon counting mode'. This is a special mode of detection where the camera can count single photon events and build up a spectrum over time based on the discrete counting of these events. It is this ultra-high sensitivity and extremely fast spectral readout rates, along with a full featured, versatile and easy-to-use configuration platform that make the Newton^{EM} the ideal choice for the most challenging Spectroscopy applications.

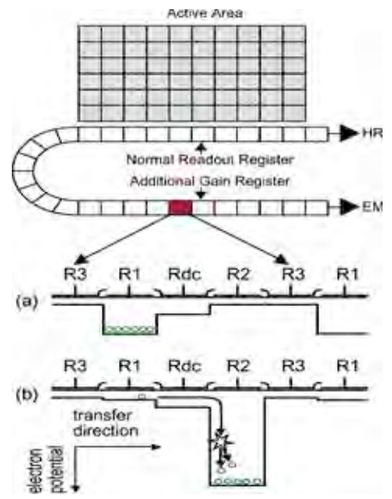

Figure 2: Signal amplification by electron impact ionization – EM gain. Schematic shows charge being clocked through the EM register and being amplified in the process.

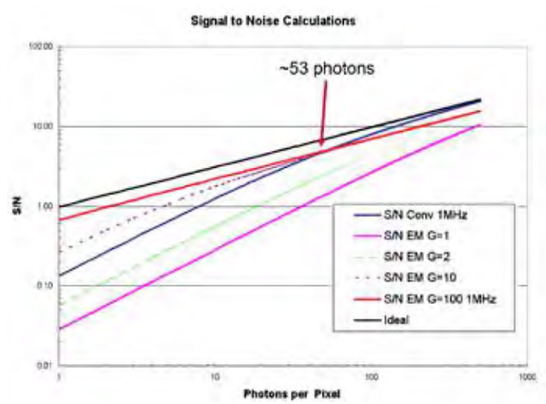

Figure 3: Signal to Noise ratios (SNR) for the EM and conventional CCDs operating in the low photon regime. SNR ratios here are based on a Newton^{EM} (DU970N) EMCCD operating at 1 MHz readout rate. The conventional, ideal and curves for several values of gain are included.

Part Numbers

Accessories

Fibre optics assemblies

ME-OPT-8004	1 way fibre, single 50um core, UV/VIS, SMA-SMA, 2 m
SR-OPT-8002	1 way fibre bundle, 100 um core, LOH-VIS/NIR, 2 m
SR-OPT-8007	2 way fibre bundle, 100 um core, LOH-VIS/NIR, 2 m
SR-OPT-8008	4 way fibre bundle, 100 um core, LOH-VIS/NIR, 2 m
SR-OPT-8009	5 way fibre bundle, 100 um core, LOH-VIS/NIR, 2 m
SR-OPT-8013	3 way fibre bundle, 100 um core, LOH-VIS/NIR, 2 m
SR-OPT-8014	1 way fibre bundle, 100 um core, HOH-UV/VIS, 2 m
SR-OPT-8015	2 way fibre bundle, 100 um core, HOH-UV/VIS, 2 m
SR-OPT-8016	3 way fibre bundle, 100 um core, HOH-UV/VIS, 2 m
SR-OPT-8017	4 way fibre bundle, 100 um core, HOH-UV/VIS, 2 m
SR-OPT-8018	5 way fibre bundle, 100 um core, HOH-UV/VIS, 2 m
SR-OPT-8019	1 way fibre bundle, 200 um core, LOH-VIS/NIR, 2 m
SR-OPT-8020	2 way fibre bundle, 200 um core, LOH-VIS/NIR, 2 m
SR-OPT-8021	3 way fibre bundle, 200 um core, LOH-VIS/NIR, 2 m
SR-OPT-8022	4 way fibre bundle, 200 um core, LOH-VIS/NIR, 2 m
SR-OPT-8024	1 way fibre bundle, 200 um core, HOH-UV/VIS, 2 m
SR-OPT-8025	2 way fibre bundle, 200 um core, HOH-UV/VIS, 2 m
SR-OPT-8026	3 way fibre bundle, 200 um core, HOH-UV/VIS, 2 m
SR-OPT-8027	4 way fibre bundle, 200 um core, HOH-UV/VIS, 2 m

Filters Neutral Density

TN-0300-001-#UV	ND 0.3, UV-Vis
TN-0300-001-NIR	ND 0.3, Vis Nir
TN-0400-001-#UV	ND 0.4, UV-Vis
TN-0500-001-#UV	ND 0.5, UV-Vis
TN-0600-001-#UV	ND 0.6, UV-Vis
TN-0600-001-NIR	ND 0.6, Vis Nir
TN-0700-001-#UV	ND 0.7, UV-Vis
TN-0800-001-#UV	ND 0.8, UV-Vis
TN-0900-001-#UV	ND 0.9, UV-Vis
TN-1000-001-#UV	ND 1.0, UV-Vis
TN-1000-001-NIR	ND 1.0, Vis Nir
TN-1500-001-#UV	ND 1.5, UV-Vis
TN-2000-001-#UV	ND 2.0, UV-Vis
TN-2000-001-NIR	ND 2.0, Vis Nir
TN-3000-001-#UV	ND 3.0, UV-Vis
TN-3000-001-NIR	ND 3.0, Vis Nir

Filters Long and Short pass

TL-0400-001	400 nm cut-on, 400-2000 nm trans., Ø25.4 mm
TL-0450-001	450 nm cut-on, 450-2000 nm trans., Ø25.4 mm
TL-0500-001	500 nm cut-on, 500-2000 nm trans., Ø25.4 mm
TL-0550-001	550 nm cut-on, 550-2000 nm trans., Ø25.4 mm
TL-0600-001	600 nm cut-on, 600-2000 nm trans., Ø25.4 mm
TL-0650-001	650 nm cut-on, 650-2000 nm trans., Ø25.4 mm
TL-0700-001	700 nm cut-on, 700-2000 nm trans., Ø25.4 mm
TL-0750-001	750 nm cut-on, 750-2000 nm trans., Ø25.4 mm
TL-0800-001	800 nm cut-on, 800-2000 nm trans., Ø25.4 mm
TL-0850-001	850 nm cut-on, 850-2000 nm trans., Ø25.4 mm
TL-0900-001	900 nm cut-on, 900-2000 nm trans., Ø25.4 mm
TL-0950-001	950 nm cut-on, 950-2000 nm trans., Ø25.4mm
TL-1000-001	1000n m cut-on, 1000-2000 nm trans., Ø25.4 mm
TS-0400-001	400 nm cut-on, 240-400 nm trans., Ø25.4 mm
TS-0450-001	450 nm cut-on, 270-450 nm trans., Ø25.4mm
TS-0500-001	500 nm cut-on, 300-500 nm trans., Ø25.4 mm
TS-0550-001	550 nm cut-on, 330-550 nm trans., Ø25.4 mm
TS-0600-001	600 nm cut-on, 360-600 nm trans., Ø25.4 mm
TS-0650-001	650 nm cut-on, 390-650 nm trans., Ø25.4 mm
TS-0700-001	700 nm cut-on, 420-700 nm trans., Ø25.4 mm
TS-0750-001	750 nm cut-on, 450-750 nm trans., Ø25.4 mm
TS-0800-001	800 nm cut-on, 480-800 nm trans., Ø25.4 mm
TS-0850-001	850 nm cut-on, 510-850 nm trans., Ø25.4 mm
TS-0900-001	900 nm cut-on, 540-900 nm trans., Ø25.4 mm
TS-0950-001	950 nm cut-on, 570-950 nm trans., Ø25.4 mm
TS-1000-001	1000 nm cut-on, 600-1000 nm trans., Ø25.4 mm

Accessories cont.

Light sources

ACC-OCE-HG-1	Hg-Ar calibration lamp and power supply
LK-##AR-PEN	Ar pen ray calibration lamp
LK-##KR-PEN	Kr pen ray calibration lamp
LK-##NE-PEN	Ne pen ray calibration lamp
LK-##XE-PEN	Xe pen ray calibration lamp
LK-DHRD-OCE	Deuterium-Halogen lamp, radiometrically calibrated
LK-HGAR-PEN	Hg-Ar pen ray calibration lamp
LK-HGNE-PEN	Hg-Ne pen ray calibration lamp
LM-PENA	Pen Ray shield type A, 1.02 mm pinhole
LM-PENB	Pen Ray shield type B, 7.78x16 mm aperture
LM-PENC	Pen Ray shield type C, 4.8x38.1 mm aperture
LM-PENF-#SW	Pen Ray Shield with G-275 converter (264 nm)
LM-PENF-#LW	Pen Ray Shield with G-278 converter (365 nm)
LP-0220-006	Pen Ray power supply (LK-##XE-PEN)
LP-0220-010	Pen Ray power supply (LK-##AR-PEN, KR, NE)
LP-0220-018	Pen Ray power supply (LK-HGAR-PEN, HGNE)

Single point detectors and Scanning accessories

ACC-SR-ASM-0042	MCT detector with LN_2 Dewar and Au focusing mirror
ACC-SR-ASM-0043	InSb detector with LN_2 Dewar and Au focusing mirror
ACC-SR-ASM-0044	InGaAs detector + TE cooler and power supply
ACC-SR-ASM-0045	PbS with built-in amplifier
ACC-SR-ASM-0046	Si photodiode, UV-enhanced
ACC-SR-ASM-0047	PMT type R928
SR-ASM-0048	PMT type R1527P (Photon counting)
ACC-SR-ASZ-0053	HV power supply for PMT
ACC-SR-ASZ-0054	Photon counting unit for PMT
ACC-SR-ASZ-0055	Data acquisition unit

Microscope accessories

TR-LCDM-CAGE-ADP	Cage system adapter to Leica DMI4000/6000B
TR-LCDM-MNT-127	Feet set for Leica DMI4000/6000B, SR303i
TR-LCDM-MNT-150	Feet set for Leica DMI4000/6000B, SR500i/750
TR-NKTI-CAGE-ADP	Cage system adapter to Nikon Eclipse Ti-E
TR-NKTI-MNT-127	Feet set for Nikon Eclipse Ti-E, SR303i
TR-NKTI-MNT-150	Feet set for Nikon Eclipse Ti-E, SR500i/750
TR-NK2K-CAGE-ADP	Cage system adapter to Nikon TE2000
TR-NK2K-MNT-127	Feet set for Nikon TE2000, SR303i
TR-NK2K-MNT-150	Feet set for Nikon TE2000, SR500i/750
TR-OLIX-CAGE-ADP	Cage system adapter to Olympus IX71/81
TR-OLIX-MNT-127-LP	Feet set for Olympus IX71/81 left port, SR303i
TR-OLIX-MNT-150-LP	Feet set for Olympus IX71/81 left port, SR500i/750
SR-ASZ-0079	C-mount to C-mount 1:1 infinity extender
TR-ZSAV-CAG-ADP	Cage system adapter to Zeiss Axiovert 200
TR-ZSAV-MNT-127	Feet set for Zeiss Axiovert 200, SR303i
TR-ZSAV-MNT-150	Feet set for Zeiss Axiovert 200, SR500i/750
TR-ZAXO-CAG-ADP	Cage system adapter to Zeiss Axio Observer
TR-ZAXO-MNT-127	Feet set for Zeiss Axio Observer, SR303i
TR-ZAXO-MNT-150	Feet set for Zeiss Axio Observer, SR500i/750

Cameras

Accessories

ACC-XW-CHIL-160	Oasis 160 ultra compact chiller unit with hose
CCI-010	PCI card MHz for ICCD
CCI-23	PCI card iXon3
IO-160	Input/Output and synchronization box
OPTION-C1-AR1	AR coated window (400-900 nm) for Spectroscopy CCD
OPTION-C1-MGF2	MgF_2 window for Spectroscopy CCD

PS150	ICCD power supply for deep cooling
P25 Shutter	Prontor 25 mm standalone shutter
PS25	CCD power supply for deep cooling
SD-166	P25 Prontor 25 mm shutter control
XU-RECR/TRANS	USB 2.0 fibre optic extender - emitter and receiver
XW-RECR	Koolance Exos II recirculator with mains power supply

iDus and iDus InGaAs

DU401A-BR-DD	1024x128, 26 µm, BI Deep Depletion, 100 kHz, -100ºC , FS
DU401A-BVF	1024x127, 26 µm, BI + Vis AR coating, 100 kHz, -100ºC, FS
DU401A-FI	1024x127, 26 µm, Front-Illuminated, 100 kHz, -100ºC
DU420A-BEX2-DD	1024x256, 26 µm, BI Deep Depletion Broadband Dual-AR, 100 kHz, -100ºC, FS
DU420A-BR-DD	1024x256, 26 µm, BI Deep Depletion, 100 kHz, -100ºC
DU420A-BU	1024x255, 26 µm, BI 350 nm-optimized, 100 kHz, -100ºC
DU420A-BU2	1024x255, 26 µm, BI 250 nm-optimized, 100 kHz, -100ºC
DU420A-BV	1024x255, 26 µm, BI + Vis AR coating, 100 kHz, -100ºC
DU420A-BVF	1024x255, 26 µm, BI + Vis AR coating, 100 kHz, -100ºC, FS
DU416A-LDC-DD	2000x256, 15 µm, BI Low Dark Current Deep Depletion, 100 kHz, -95ºC
DV416-LDC-DD	2000x256, 15 µm, BI Low Dark Current Deep Depletion, 100 kHz, -70ºC
DU420A-OE	1024x255, 26 µm, Open Electrode, 100 kHz, -100ºC

DU490A-1.7	512x1, 25x500 µm, InGaAs 1.7 µm cuttoff, 100 kHz, -85ºC
DU490A-2.2	512x1, 25x250 µm, InGaAs 2.2 µm cuttoff, 100 kHz, -85ºC
DU491A-1.7	1024x1, 25x500 µm, InGaAs 1.7 um cuttoff, 100 kHz, -85ºC
DU491A-2.2	1024x1, 25x250 µm, InGaAs 2.2 um cuttoff, 100 kHz, -85ºC
DU492A-1.7	512x1, 50x500 µm, InGaAs 1.7 um cuttoff, 100 kHz, -85ºC
DU492A-2.2	512x1, 50x250 µm, InGaAs 2.2 um cuttoff, 100 kHz, -85ºC
DV401A-BVF	1024x255, 26 µm, BI + Vis AR coating, 100 kHz, -70ºC, FS
DV401A-FI	1024x255, 26 µm, Front-Illuminated, 100 kHz, -70ºC
DV420A-BU	1024x255, 26 µm, BI 350 nm-optimized, 100 kHz, -70ºC
DV420A-BU2	1024x255, 26 µm, BI 250 nm-optimized, 100 kHz, -70ºC
DV420A-BV	1024x255, 26 µm, BI + Vis AR coating, 100 kHz, -70ºC
DV420A-BVF	1024x255, 26 µm, BI + Vis AR coating, 100 kHz, -70ºC, FS
DV420A-OE	1024x255, 26 µm, Open Electrode, 100 kHz, -70ºC

iStar

DH320T-18F-03	1024x255 CCD, Ø18 mm, Gen 2 Broad, 5 ns, Intelligate
DH320T-18U-03	1024x256 CCD, Ø18 mm, Gen 2 Broad, 5 ns, Intelligate
DH320T-18F-04	1024x255 CCD, Ø18 mm, Gen 2 Broad, 5 ns, P46 , Intelligate
DH320T-18U-04	1024x255 CCD, Ø18 mm, Gen 2 Broad, 2 ns, P46 , Intelligate
DH320T-18F-05	1024x255 CCD, Ø18 mm, Gen 2 Broad, 10 ns, MgF2 , Intelligate
DH320T-18U-05	1024x255 CCD, Ø18 mm, Gen 2 Broad, 5 ns, MgF2 , Intelligate
DH320T-18H-13	1024x255 CCD, Ø18 mm, Gen 2 Red, 50ns , Intelligate
DH320T-18F-63	1024x255 CCD, Ø18 mm, Gen 3 Vis, 5 ns , Intelligate
DH320T-18U-63	1024x255 CCD, Ø18 mm, Gen 3 Vis, 2 ns , Intelligate
DH320T-18F-73	1024x255 CCD, Ø18 mm, Gen 3 Nir, 5 ns , Intelligate
DH320T-18U-73	1024x255 CCD, Ø18 mm, Gen 3 Nir, 2 ns , Intelligate

DH320T-18H-83	1024x255 CCD, Ø18 mm, Gen 2 UV, 100 ns , Intelligate
DH320T-18F-93	1024x255 CCD, Ø18 mm, Gen 3 InGaAs, 5 ns , Intelligate
DH320T-18U-93	1024x255 CCD, Ø18 mm, Gen 3 InGaAs, 2 ns , Intelligate
DH320T-18F-A3	1024x255 CCD, Ø18 mm, Gen 3 Vis-Nir, 5 ns , Intelligate
DH320T-18U-A3	1024x255 CCD, Ø18 mm, Gen 3 Vis-Nir, 2 ns , Intelligate
DH320T-18F-C3	1024x255 CCD, Ø18 mm, Gen 3 Nir + UV coating, 5 ns , Intelligate
DH320T-18U-C3	1024x255 CCD, Ø18 mm, Gen 3 Nir + UV coating, 2 ns , Intelligate
DH320T-18F-E3	1024x255 CCD, Ø18 mm, Gen 2 UV, 5 ns , Intelligate
DH320T-18U-E3	1024x255 CCD, Ø18 mm, Gen 2 UV, 2 ns , Intelligate
DH320T-25F-03	1024x255 CCD, Ø25 mm, Gen 2 Broad, 3 ns , Intelligate
DH320T-25U-03	1024x255 CCD, Ø25 mm, Gen 2 Broad, 7 ns , Intelligate

Cameras cont.

DH334T-18F-03	1024x1024 CCD, Ø18 mm, Gen 2 Broad, 5 ns, Intelligate
DH334T-18U-03	1024x1024 CCD, Ø18 mm, Gen 2 Broad, 2 ns , Intelligate
DH334T-18F-04	1024x1024 CCD, Ø18 mm, Gen 2 Broad, 5 ns, P46 , Intelligate
DH334T-18U-04	1024x1024 CCD, Ø18 mm, Gen 2 Broad, 2 ns, P46 , Intelligate
DH334T-18F-05	1024x1024 CCD, Ø18 mm, Gen 2 Broad, 10 ns, MgF2 , Intelligate
DH334T-18U-05	1024x1024 CCD, Ø18 mm, Gen 2 Broad, 5 ns, MgF2 , Intelligate
DH334T-18H-13	1024x1024 CCD, Ø18 mm, Gen 2 Red, 50ns , Intelligate
DH334T-18F-63	1024x1024 CCD, Ø18 mm, Gen 3 Vis, 5 ns , Intelligate
DH334T-18U-63	1024x1024 CCD, Ø18 mm, Gen 3 Vis, 2 ns , Intelligate
DH334T-18F-73	1024x1024 CCD, Ø18 mm, Gen 3 Nir, 5 ns , Intelligate
DH334T-18U-73	1024x1024 CCD, Ø18 mm, Gen 3 Nir, 2 ns , Intelligate
DH334T-18H-83	1024x1024 CCD, Ø18 mm, Gen 2 UV, 100 ns , Intelligate
DH334T-18F-93	1024x1024 CCD, Ø18 mm, Gen 3 InGaAs, 5 ns , Intelligate
DH334T-18U-93	1024x1024 CCD, Ø18 mm, Gen 3 InGaAs, 2 ns , Intelligate
DH334T-18F-A3	1024x1024 CCD, Ø18 mm, Gen 3 Vis-Nir, 5 ns , Intelligate
DH334T-18U-A3	1024x1024 CCD, Ø18 mm, Gen 3 Vis-Nir, 2 ns , Intelligate
DH334T-18F-C3	1024x1024 CCD, Ø18 mm, Gen 3 Nir + UV coating, 5 ns , Intelligate
DH334T-18U-C3	1024x1024 CCD, Ø18 mm, Gen 3 Nir + UV coating, 2 ns , Intelligate
DH334T-18F-E3	1024x1024 CCD, Ø18 mm, Gen 2 UV, 5 ns , Intelligate
DH334T-18U-E3	1024x1024 CCD, Ø18 mm, Gen 2 UV, 2 ns , Intelligate
DH334T-25F-03	1024x1024 CCD, Ø25 mm, Gen 2 Broad, 3 ns , Intelligate
DH334T-25U-03	1024x1024 CCD, Ø25 mm, Gen 2 Broad, 7 ns , Intelligate
DH340T-18F-03	2048x512 CCD, Ø18 mm, Gen 2 Broad, 5 ns, Intelligate
DH340T-18U-03	2048x512 CCD, Ø18 mm, Gen 2 Broad, 2 ns , Intelligate
DH340T-18F-04	2048x512 CCD, Ø18 mm, Gen 2 Broad, 5 ns, P46 , Intelligate
DH340T-18U-04	2048x512 CCD, Ø18 mm, Gen 2 Broad, 2 ns, P46 , Intelligate
DH340T-18F-05	2048x512 CCD, Ø18 mm, Gen 2 Broad, 10 ns, MgF2 , Intelligate
DH340T-18U-05	2048x512 CCD, Ø18 mm, Gen 2 Broad, 5 ns, MgF2 , Intelligate
DH340T-18H-13	2048x512 CCD, Ø18 mm, Gen 2 Red, 50ns , Intelligate

DH340T-18F-63	2048x512 CCD, Ø18 mm, Gen 3 Vis, 5 ns , Intelligate
DH340T-18U-63	2048x512 CCD, Ø18 mm, Gen 3 Vis, 2 ns , Intelligate
DH340T-18F-73	2048x512 CCD, Ø18 mm, Gen 3 Nir, 5 ns , Intelligate
DH340T-18U-73	2048x512 CCD, Ø18 mm, Gen 3 Nir, 2 ns , Intelligate
DH340T-18H-83	2048x512 CCD, Ø18 mm, Gen 2 UV, 100 ns , Intelligate
DH340T-18F-93	2048x512 CCD, Ø18 mm, Gen 3 InGaAs, 5 ns , Intelligate
DH340T-18U-93	2048x512 CCD, Ø18 mm, Gen 3 InGaAs, 3 ns , Intelligate
DH340T-18F-A3	2048x512 CCD, Ø18 mm, Gen 3 Vis-Nir, 5 ns , Intelligate
DH340T-18U-A3	2048x512 CCD, Ø18 mm, Gen 3 Vis-Nir, 2 ns , Intelligate
DH340T-18F-C3	2048x512 CCD, Ø18 mm, Gen 3 Nir + UV coating, 5 ns , Intelligate
DH340T-18U-C3	2048x512 CCD, Ø18 mm, Gen 3 Nir + UV coating, 2 ns , Intelligate
DH340T-18F-E3	2048x512 CCD, Ø18 mm, Gen 2 UV, 5 ns , Intelligate
DH340T-18U-E3	2048x512 CCD, Ø18 mm, Gen 2 UV, 2 ns , Intelligate
DH340T-25F-03	2048x512 CCD, Ø25 mm, Gen 2 Broad, 3 ns , Intelligate
DH340T-25U-03	2048x512 CCD, Ø25 mm, Gen 2 Broad, 7 ns , Intelligate

Cameras cont.

iXon3

DU-888E-C00-#BV	EM, 1024x1024, 13 µm, BI + Vis AR coating, 10 MHz, -100°C
DU-888E-C00-UVB	EM, 1024x1024, 13 µm, BI + UV coating, 10 MHz, -100°C
DU-897E-C00-#BV	EM, 512x512, 16 µm, BI + Vis AR coating, 10 MHz, -100°C
DU-897E-C00-UVB	EM, 512x512, 16 µm, BI + UV coating, 10 MHz, -100°C
DU-897E-C00-BVF	EM, 512x512, 16 µm, BI + Vis AR coating, 10 MHz, -100°C, FS
DU-897E-C00-#EX	EM, 512x512, 16 µm, Broadband Dual-AR, 10 MHz, -100°C
DU-897E-C00-EXF	EM, 512x512, 16 µm, Broadband Dual-AR, 10 MHz, -100°C, FS

iXon Ultra

DU-897U-C00-#BV	EM, 512x512, 16 µm, BI + Vis AR coating, 10 MHz, -100°C
DU-897U-C00-UVB	EM, 512x512, 16 µm, BI + UV coating, 10 MHz, -100°C
DU-897U-C00-BVF	EM, 512x512, 16 µm, BI + Vis AR coating, 10 MHz, -100°C, FS
DU-897U-C00-#EX	EM, 512x512, 16 µm, Broadband Dual-AR, 10 MHz, -100°C
DU-897U-C00-EXF	EM, 512x512, 16 µm, Broadband Dual-AR, 10 MHz, -100°C, FS

Newton and Newton^{EM}

DU920P-BEX2-DD	1024x256, 26 µm, BI Deep Depletion Broadband Dual-AR, 100 kHz, -100°C, FS
DU920P-BR-DD	1024x256, 26 µm, BI Deep Depletion, 3 MHz, -100°C, FS
DU920P-BU	1024x255, 26 µm, BI 350 nm-optimized, 3 MHz, -100°C
DU920P-BU2	1024x255, 26 µm, BI 250 nm-optimized, 3 MHz, -100°C
DU920P-BV	1024x255, 26 µm, BI + Vis AR coating, 3 MHz, -100°C
DU920P-BVF	1024x255, 26 µm, BI + Vis AR coating, 3 MHz, -100°C, FS
DU920P-OE	1024x255, 26 µm, Open Electrode, 3 MHz, -100°C
DU920P-UVB	1024x255, 26 µm, BI + UV coating, 3 MHz, -100°C
DU940P-BU	2048x512, 13.5 µm, BI 350 nm-optimized, 3 MHz, -100°C
DU940P-BU2	2048x512, 13.5 µm, BI 250 nm-optimized, 3 MHz, -100°C
DU940P-BV	2048x512, 13.5 µm, BI + Vis AR coating, 3 MHz, -100°C
DU940P-FI	2048x512, 13.5 µm, Front-Illuminated, 3 MHz, -100°C
DU940P-UV	2048x512, 13.5 µm, FI + UV coating, 3 MHz, -100°C
DU970P-BV	EM, 1600x200, 16 µm, BI + Vis-AR coating, 3 MHz, -100°C
DU970P-BVF	EM, 1600x200, 16 µm, BI + Vis-AR coating, 3 MHz, -100°C, FS
DU970P-FI	EM, 1600x200, 16 µm, Front-Illuminated, 3 MHz, -100°C
DU970P-UV	EM, 1600x200, 16 µm, FI + UV coating, 3 MHz, -100°C
DU970P-UVB	EM, 1600x200, 16 µm, BI + UV coating, 3 MHz, -100°C
DU971P-BV	EM, 1600x400, 16 µm, BI + Vis AR coating, 3 MHz, -100°C
DU971P-FI	EM, 1600x400, 16 µm, Front-Illuminated, 3 MHz, -100°C
DU971P-UV	EM, 1600x400, 16 µm, FI + UV coating, 3 MHz, -100°C
DU971P-UVB	EM, 1600x400, 16 µm, BI + UV coating, 3 MHz, -100°C

Spectrographs

Mechelle and specific accessories

ME5000	Mechelle 5000 unit
ME-OPT-0007	UV-VIS-NIR collector-collimator
ME-SHT-9002	Shutter assembly
ME-SLT-10*50	10x50 µm slit
ME-SLT-100*50	100x50 µm slit
ME-SLT-200*50	200x50 µm slit
ME-SLT-25*25	25x25 µm slit
ME-SLT-25*50	25x50 µm slit
ME-SLT-50*25	50x25 µm slit
ME-SLT-50*50	50x50 µm slit

Shamrock 163 and specific accessories

SR-163	Shamrock 163 base unit
SR1-ASM-0020	Manual adjustable input slit, 3 mm high
SR1-ASM-0020-EQ	Manual adjustable input slit, 6 mm high
SR1-ASM-0023	C-mount input adapter
SR1-ASM-7003	Ø1" filter holder
SR1-ASM-7004	Rectangular 1" filter holder
SR1-ASM-8032	Fixed ferrule adapter
SR1-ASM-8035	Fixed SMA input adapter
SR1-ASM-8036	Fibre ferrule adapter (adjustable slit and shutter)
SR1-ASM-8038	Fixed slit holder
SR1-ASZ-8033	Fixed SMA input adapter (correction lens)
SR1-ASZ-8034	Fixed slit input adapter (correction lens)
SR1-ASZ-8044	InGaAs flange (correction lens)
SR1-GRT-0085-0130	Grating 85 l/mm, 130 nm blaze
SR1-GRT-0100-1600	Grating 100 l/mm, 1600 nm blaze
SR1-GRT-0150-0300	Grating 150 l/mm, 300 nm blaze
SR1-GRT-0150-0500	Grating 150 l/mm, 500 nm blaze
SR1-GRT-0150-0800	Grating 150 l/mm, 800 nm blaze

Spectrographs cont.

SR1-GRT-0150-1250	Grating 150 l/mm, 1250 nm blaze
SR1-GRT-0150-2000	Grating 150 l/mm, 2000 nm blaze
SR1-GRT-0200-0750	Grating 200 l/mm, 750 nm blaze
SR1-GRT-0200-1700	Grating 200 l/mm, 1700 nm blaze
SR1-GRT-0235-0750	Grating 200 l/mm, 1700 nm blaze
SR1-GRT-0300-0300	Grating 300 l/mm, 300 nm blaze
SR1-GRT-0300-0422	Grating 200 l/mm, 1700 nm blaze
SR1-GRT-0300-0500	Grating 300 l/mm, 500 nm blaze
SR1-GRT-0300-0760	Grating 300 l/mm, 760 nm blaze
SR1-GRT-0300-0860	Grating 300 l/mm, 860 nm blaze
SR1-GRT-0300-1000	Grating 300 l/mm, 1000 nm blaze
SR1-GRT-0300-1200	Grating 300 l/mm, 1200 nm blaze
SR1-GRT-0300-1700	Grating 300 l/mm, 1700 nm blaze
SR1-GRT-0400-0400	Grating 400 l/mm, 400 nm blaze
SR1-GRT-0400-0550	Grating 400 l/mm, 550 nm blaze
SR1-GRT-0500-0330	Grating 500 l/mm, 330nm blaze
SR1-GRT-0500-0560	Grating 500 l/mm, 560nm blaze
SR1-GRT-0600-0300	Grating 600 l/mm, 300 nm blaze
SR1-GRT-0600-0500	Grating 600 l/mm, 500 nm blaze
SR1-GRT-0600-0650	Grating 600 l/mm, 650 nm blaze
SR1-GRT-0600-0750	Grating 600 l/mm, 750 nm blaze
SR1-GRT-0600-1000	Grating 600 l/mm, 1000 nm blaze
SR1-GRT-0600-1200	Grating 600 l/mm, 1200 nm blaze
SR1-GRT-0600-1600	Grating 600 l/mm, 1600 nm blaze
SR1-GRT-0600-1900	Grating 600 l/mm, 1900nm blaze
SR1-GRT-1200-0300	Grating 1200 l/mm, 300 nm blaze
SR1-GRT-1200-0400	Grating 1200 l/mm, 400 nm blaze
SR1-GRT-1200-0500	Grating 1200 l/mm, 500 nm blaze
SR1-GRT-1200-0750	Grating 1200 l/mm, 750 nm blaze
SR1-GRT-1200-1080	Grating 1200 l/mm, 1080 nm blaze
SR1-GRT-1200-EH	Grating 1200 l/mm, Holographic, 400-1200 nm
SR1-GRT-1500-0250	Grating 1500 l/mm, 250 nm blaze
SR1-GRT-1800-0400	Grating 1800 l/mm, 400 nm blaze
SR1-GRT-1800-0500	Grating 1800 l/mm, 500 nm blaze
SR1-GRT-1800-DH	Grating 1800 l/mm, Holographic, 190-900 nm
SR1-GRT-1800-FH	Grating 1800 l/mm, Holographic, 350-900 nm
SR1-GRT-2400-0300	Grating 2400 l/mm, 300 nm blaze
SR1-GRT-2400-BH	Grating 2400 l/mm, Holographic, 190-800 nm
SR1-GRT-2400-GH	Grating 2400 l/mm, Holographic, 250-600 nm
SR1-SLT-9003	Shutter assembly (PCI)
SR1-SLT-9004	Shutter assembly (I²C)
SR1-SLH-0010-3	10 um x 3 mm slit for shutter
SR1-SLH-0025-3	25 um x 3 mm slit for shutter
SR1-SLH-0050-3	50 um x 3 mm slit for shutter
SR1-SLH-0075-3	75 um x 3 mm slit for shutter
SR1-SLH-0100-3	100um x 3 mm slit for shutter
SR1-SLH-0200-3	200 um x 3 mm slit for shutter
SR1-SLT-0010-3	10 um x 3 mm slit
SR1-SLT-0025-3	25 um x 3 mm slit
SR1-SLT-0050-3	50 um x 3 mm slit
SR1-SLT-0075-3	75 um x 3 mm slit
SR1-SLT-0100-3	100 um x 3 mm slit
SR1-SLT-0200-3	200 um x 3 mm slit

Shamrock 303i and specific accessories

SR-303I-A	Shamrock 303i base unit, single output port
SR-303I-B	Shamrock 303i base unit, double output port
MFL-SR303I-888	iXon3 mounting flange kit DU888
MFL-SR303I-INTER	Intermediate plane CCD mounting flange (Imaging)
MFL-SR303I-IXON	iXon3 mounting flange kit (Not 888)
SR-ASM-0003	Additionnal blank grating turret
SR-ASM-0022	Adjustable feet set (4off)
SR-ASZ-0005	Slit assembly for second exit port
SR-ASZ-0034	Wide-aperture entrance slit
SR-SHT-9001	Entrance shutter for SR-303i
SR3-GRT-0050-0600	Grating 50 l/mm, 600 nm blaze
SR3-GRT-0060-0750	Grating 60 l/mm, 750 nm blaze
SR3-GRT-0120-0330	Grating 120 l/mm, 330nm blaze
SR3-GRT-0150-0300	Grating 150 l/mm, 300 nm blaze
SR3-GRT-0150-0500	Grating 150 l/mm, 500 nm blaze
SR3-GRT-0150-0800	Grating 150 l/mm, 800nm blaze
SR3-GRT-0150-1250	Grating 150 l/mm, 1250 nm blaze
SR3-GRT-0150-2000	Grating 150 l/mm, 2000 nm blaze
SR3-GRT-0235-0750	Grating 235 l/mm, 750 nm blaze
SR3-GRT-0300-0300	Grating 300 l/mm, 300 nm blaze

Spectrographs cont.

SR3-GRT-0300-0500	Grating 300 l/mm, 500 nm blaze
SR3-GRT-0300-0760	Grating 300 l/mm, 760 nm blaze
SR3-GRT-0300-1000	Grating 300 l/mm, 1000 nm blaze
SR3-GRT-0300-1200	Grating 300 l/mm, 1200 nm blaze
SR3-GRT-0300-1700	Grating 300 l/mm, 1700 nm blaze
SR3-GRT-0300-2000	Grating 300 l/mm, 2000 nm blaze
SR3-GRT-0300-3000	Grating 300 l/mm, 3000 nm blaze
SR3-GRT-0400-0850	Grating 400 l/mm, 850 nm blaze
SR3-GRT-0500-0230	Grating 500 l/mm, 230 nm blaze
SR3-GRT-0600-0300	Grating 600 l/mm, 300 nm blaze
SR3-GRT-0600-0400	Grating 600 l/mm, 400 nm blaze
SR3-GRT-0600-0500	Grating 600 l/mm, 500 nm blaze
SR3-GRT-0600-0650	Grating 600 l/mm, 650 nm blaze
SR3-GRT-0600-0750	Grating 600 l/mm, 750 nm blaze
SR3-GRT-0600-1000	Grating 600 l/mm, 1000 nm blaze
SR3-GRT-0600-1200	Grating 600 l/mm, 1200 nm blaze
SR3-GRT-0900-0550	Grating 900 l/mm, 550 nm blaze
SR3-GRT-1000-0250	Grating 1000 l/mm, 250 nm blaze
SR3-GRT-1000-1300	Grating 1000 l/mm, 1300 nm blaze
SR3-GRT-1200-0300	Grating 1200 l/mm, 300 nm blaze
SR3-GRT-1200-0350	Grating 1200 l/mm, 350 nm blaze
SR3-GRT-1200-0400	Grating 1200 l/mm, 400 nm blaze
SR3-GRT-1200-0500	Grating 1200 l/mm, 500 nm blaze
SR3-GRT-1200-0600	Grating 1200 l/mm, 600 nm blaze
SR3-GRT-1200-0750	Grating 1200 l/mm, 750 nm blaze
SR3-GRT-1200-1000	Grating 1200 l/mm, 1000 nm blaze
SR3-GRT-1200-1100	Grating 1200 l/mm, 1100 nm blaze
SR3-GRT-1200-EH	Grating 1200 l/mm, Holographic, 400-1200 nm
SR3-GRT-1800-0500	Grating 1800 l/mm, 500 nm blaze
SR3-GRT-1800-DH	Grating 1800 l/mm, Holographic, 190-900 nm
SR3-GRT-1800-FH	Grating 1800 l/mm, Holographic, 350-900 nm
SR3-GRT-2400-0300	Grating 2400 l/mm, 300 nm blaze
SR3-GRT-2400-BH	Grating 2400 l/mm, Holographic, 190-800 nm
SR3-GRT-2400-GH	Grating 2400 l/mm, Holographic, 250-600 nm
SR3-GRT-MR-AL+MGF2	Shamrock 303i flat mirror for grating turret, Al+MgF_2 coating

Shamrock 500i/750 and specific accessories

SR-500I-A	SR500i base, single entrance slit, CCD exit port
SR-500I- B1	SR500i base, single entrance and exit slit, CCD exit port
SR-500I-B2	SR500i base, single entrance slit, dual CCD exit ports
SR-500I-C	SR500i base, double entrance slit, CCD exit port
SR-500I-D1	SR500i base, double entrance slit, CCD exit port and exit slit
SR-500I-D2	SR500i base, double entrance slit, dual CCD exit port
SR-750-A	SR750 base, single entrance slit, CCD exit port
SR-750-B1	SR750 base, single entrance and exit slit, CCD exit port
SR-750-B2	SR750 base, single entrance slit, dual CCD exit ports
SR-750-C	SR750 base, double entrance slit, CCD exit port
SR-750-D1	SR750 base, double entrance slit, CCD exit port and exit slit
SR-750-D2	SR750 base, double entrance slit, dual CCD exit port
MFL-SR500	CCD mounting flange kit
MFL-SR500-IXON	iXon mounting flange kit
SR-ASM-0025	Manual slit assembly baffle, 6W x 4H
SR-ASM-0026	Manual slit assembly baffle, 6W x 6H
SR-ASM-0027	Manual slit assembly baffle, 6W x 8H
SR-ASM-0028	Manual slit assembly baffle, 6W x 10H
SR-ASM-0029	Manual slit assembly baffle, 6W x 14H
SR-ASM-0085	Additionnal blank grating turret
SR-ASM-0062	Exit port slit adapter for CCD flange
SR-ASZ-0030	Manual exit port slit
SR-ASZ-0032	Motorized entrance slit (front port)
SR-ASZ-0033	SR750 InGaAs camera flange
SR-ASZ-0035	Motorized entrance slit (side port)
SR-ASZ-0036	Motorized slit for second exit port
SR-ASZ-7005	Motorized filter wheel
SR-SHT-9002	Shutter for entrance ports
SR5-GRT-0075-12000	Grating, 75 l/mm blazed at 12000 nm
SR5-GRT-0085-1350	Grating, 85 l/mm blazed at 1350 nm
SR5-GRT-0150-0300	Grating, 150 l/mm blazed at 300 nm
SR5-GRT-0150-0500	Grating, 150 l/mm blazed at 500 nm
SR5-GRT-0150-0800	Grating, 150 l/mm blazed at 800 nm
SR5-GRT-0150-1250	Grating, 150 l/mm blazed at 1250 nm
SR5-GRT-0150-2000	Grating, 150 l/mm blazed at 2000 nm
SR5-GRT-0150-8000	Grating, 150 l/mm blazed at 8000 nm
SR5-GRT-0300-0300	Grating, 300 l/mm blazed at 300 nm

Spectrographs cont.

SR5-GRT-0300-0500	Grating, 300 l/mm blazed at 500 nm
SR5-GRT-0300-0760	Grating, 300 l/mm blazed at 760 nm
SR5-GRT-0300-1000	Grating, 300 l/mm blazed at 1000 nm
SR5-GRT-0300-1200	Grating, 300 l/mm blazed at 1200 nm
SR5-GRT-0300-1700	Grating, 300 l/mm blazed at 1700 nm
SR5-GRT-0300-2000	Grating, 300 l/mm blazed at 2000 nm
SR5-GRT-0300-3000	Grating, 300 l/mm blazed at 3000 nm
SR5-GRT-0300-4800	Grating, 300 l/mm blazed at 4800 nm
SR5-GRT-0600-0300	Grating, 600 l/mm blazed at 300 nm
SR5-GRT-0600-0500	Grating, 600 l/mm blazed at 500 nm
SR5-GRT-0600-0750	Grating, 600 l/mm blazed at 750 nm
SR5-GRT-0600-1000	Grating, 600 l/mm blazed at 1000 nm
SR5-GRT-0600-1200	Grating, 600 l/mm blazed at 1200 nm
SR5-GRT-0600-1600	Grating, 600 l/mm blazed at 1600 nm
SR5-GRT-0600-1900	Grating, 600 l/mm blazed at 1900 nm
SR5-GRT-0600-2500	Grating, 600 l/mm blazed at 2500 nm
SR5-GRT-0720-2000	Grating, 720 l/mm blazed at 2000 nm
SR5-GRT-0830-1200	Grating, 830 l/mm blazed at 1200 nm
SR5-GRT-0900-0550	Grating, 900 l/mm blazed at 550 nm
SR5-GRT-1000-1310	Grating, 1000 l/mm blazed at 1310 nm
SR5-GRT-1200-0300	Grating, 1200 l/mm blazed at 300 nm
SR5-GRT-1200-0500	Grating, 1200 l/mm blazed at 500 nm
SR5-GRT-1200-0750	Grating, 1200 l/mm blazed at 750 nm
SR5-GRT-1200-1000	Grating, 1200 l/mm blazed at 1000 nm
SR5-GRT-1200-EH	Grating 1200 l/mm, Holographic, 400-1200 nm
SR5-GRT-1800-0500	Grating, 1800 l/mm blazed at 500 nm
SR5-GRT-1800-DH	Grating 1800 l/mm, Holographic, 190-900 nm
SR5-GRT-1800-FH	Grating 1800 l/mm, Holographic, 350-900 nm
SR5-GRT-2400-0240	Grating, 2400 l/mm blazed at 240 nm
SR5-GRT-2400-0300	Grating, 2400 l/mm blazed at 300 nm
SR5-GRT-2400-BH	Grating 2400 l/mm, Holographic, 190-800 nm
SR5-GRT-2400-GH	Grating 2400 l/mm, Holographic, 250-600 nm
SR5-GRT-MR-Al+MGF2	Shamrock 500i/750 flat mirror for grating turret AR and MgF_2 coating

Shamrock 303i, 500i and 750 generic accessories

ACC-SR-ASZ-0056	Sample chamber
SR-ASM-0002	Oriel 1.5" flange adapter
SR-ASM-0010	Motorized slit baffle - 6x8 mm (WxH)
SR-ASM-0011	Motorized slit baffle - 6x14 mm (WxH)
SR-ASM-0013	Nikon lens F-mount input adapter
SR-ASM-0014	Pen ray lamp mount for entrance slit
SR-ASM-0015	Motorized slit baffle - Ø15 mm
SR-ASM-0016	Motorized slit baffle - 6x4 mm (WxH)
SR-ASM-0017	Motorized slit baffle - 6x6 mm (WxH)
SR-ASM-0021	C-mount input adapter
SR-ASM-0038	F/Matcher for 303i, 11 mm ferrule input
SR-ASM-0039	F/Matcher for 500i, ferrule input
SR-ASM-0040	F/Matcher for 750, ferrule input
SR-ASM-0041	SMA adaptor for F/matcher
SR-ASM-0065	Cage system adapter
SR-ASM-8006	X-adjustable fibre ferrule adapter
SR-ASM-8010	XY adjustable fibre ferrule adapter
SR-ASM-8040	Purge plug for Shamrock
SR-ASM-8053	XY adjustable FC adapter, upgradable (direct)
SR-ASM-8055	XY adjustable FC-APC adapter, upgradable (direct)
SR-ASM-8054	XY adjustable SMA adapter, upgradable (direct)
SR-ASM-8057	XY adjustable ferrule adapter (direct)
SR-ASM-8056	XY adjustable FC adapter, upgradable (with slit)
SR-ASM-8052	XY adjustable SMA adapter, upgradable (with slit)
SR-ASM-8069	XY adjustable Ferrule adapter, upgradable (with slit)
ACC-FC-SLIT-APT	FC upgrade for XY adjustable adapters (with slit)
ACC-SMA-SLIT-APT	SMA upgrade for XY adjustable adapters (with slit)
ACC-FERRULE-SLIT-APT	Ferrule upgrade for XY adjustable adapters (with slit)
ACC-FC-DIRECT-APT	FC upgrade for XY adjustable adapters (direct)
ACC-FCAPC-DIRECT-APT	FC/APC upgrade for XY adjustable adapters (direct)
ACC-SMA-DIRECT-APT	SMA upgrade for XY adjustable adapters (direct)

Spectrographs cont.

Holospec Base Units

HOLOSPEC-F/1.8-VIS	Holospec spectro base, F/1.8 VIS
HOLOSPEC-F/1.8-NIR	Holospec spectro base, F/1.8 NIR
HOLOSPEC-F/1.8i-VIS	Holospec spectro base, F/1.8 VIS + Notch compartment
HOLOSPEC-F/1.8i-NIR	Holospec spectro base, F/1.8 NIR + Notch compartment

Holospec Notch filters

HS-HSPF-514.5	Holospec Notch filter 514.5 nm
HS-HSPF-532.0	Holospec Notch filter 532 nm
HS-HSPF-632.8	Holospec Notch filter 632.8 nm
HS-HSPF-785.0	Holospec Notch filter 785 nm

Holospec input and intermediate slits

HS-SLT-INPUT-0025	Holospec input slit 25 µm	HS-SLT-INTER-0025	Holospec intermediate slit 25 µm
HS-SLT-INPUT-0050	Holospec input slit 50 µm	HS-SLT-INTER-0050	Holospec intermediate slit 50 µm
HS-SLT-INPUT-0083	Holospec input slit 83 µm	HS-SLT-INTER-0083	Holospec intermediate slit 83 µm
HS-SLT-INPUT-0100	Holospec input slit 100 µm	HS-SLT-INTER-0100	Holospec intermediate slit 100 µm
HS-SLT-INPUT-0167	Holospec input slit 167 µm	HS-SLT-INTER-0167	Holospec intermediate slit 167 µm
HS-SLT-INPUT-0250	Holospec input slit 250 µm	HS-SLT-INTER-0250	Holospec intermediate slit 250 µm
HS-SLT-INPUT-0416	Holospec input slit 416 µm	HS-SLT-INTER-0416	Holospec intermediate slit 416 µm
HS-SLT-INPUT-0500	Holospec input slit 500 µm	HS-SLT-INTER-0500	Holospec intermediate slit 500 µm
HS-SLT-INPUT-0833	Holospec input slit 833 µm	HS-SLT-INTER-0833	Holospec intermediate slit 833 µm
HS-SLT-INPUT-1000	Holospec input slit 1000µm	HS-SLT-INTER-1000	Holospec intermediate slit 1000 µm
HS-SLT-INPUT-1670	Holospec input slit 1670 µm	HS-SLT-INTER-1670	Holospec intermediate slit 1670 µm
HS-SLT-INPUT-2000	Holospec input slit 2000 µm	HS-SLT-INTER-2000	Holospec intermediate slit 2000 µm
HS-SLT-INPUT-4000	Holospec input slit 4000 µm	HS-SLT-INTER-4000	Holospec intermediate slit 4000 µm

Holospec gratings

HS-HFG-539.5	Holospec grating broadband center wavelength 539.5 nm	HS-HSG-632.8-SA	Holospec grating Stokes/Anti Stokes 632.8 nm
HS-HFG-550	Holospec grating broadband center wave 550 nm	HS-HSG-632.8-LF	Holospec grating low frequency 632.8 nm
HS-HFG-600	Holospec grating broadband center wave 600 nm	HS-HSG-632.8-HF	Holospec grating high frequency 632.8 nm
HS-HFG-650	Holospec grating broadband center wave 650 nm	HS-HSG-647-SA	Holospec grating Stokes/Anti Stokes 647 nm
HS-HFG-730.8	Holospec grating broadband center wave 730.8 nm	HS-HSG-647-LF	Holospec grating low frequency 647 nm
HS-HFG-750	Holospec grating broadband center wave 750 nm	HS-HSG-647-HF	Holospec grating high frequency 647 nm
HS-HFG-850	Holospec grating broadband center wave 850 nm	HS-HSG-752-SA	Holospec grating Stokes/Anti Stokes 752 nm
HS-HVG-590	Holospec grating broadband center wave 590 nm	HS-HSG-752-LF	Holospec grating low frequency 752 nm
HS-HVG-800	Holospec grating broadband center wave 800 nm	HS-HSG-752-HF	Holospec grating high frequency 752 nm
HS-HVG-821	Holospec grating broadband center wave 821 nm	HS-HSG-785-SA	Holospec grating Stokes/Anti Stokes 785 nm
HS-HSG-514.5-SA	Holospec grating Stokes/Anti Stokes 514.5 nm	HS-HSG-785-LF	Holospec grating low frequency 785 nm
HS-HSG-514.5-LF	Holospec grating low frequency 514.5 nm	HS-HSG-785-HF	Holospec grating high frequency 785 nm
HS-HSG-514.5-HF	Holospec grating high frequency 514.5 nm	HS-HDG-785	Holospec grating high dispersion Stokes/Anti Stokes 785 nm
HS-HSG-532-SA	Holospec grating Stokes/Anti Stokes 532 nm	HS-HSG-830-SA	Holospec grating Stokes/Anti Stokes 830 nm
HS-HSG-532-LF	Holospec grating low frequency 532 nm	HS-HSG-830-LF	Holospec grating low frequency 830 nm
HS-HSG-532-HF	Holospec grating high frequency 532 nm	HS-HSG-830-HF	Holospec grating high frequency 830 nm
HS-HDG-532	Holospec grating high dispersion Stokes/Anti Stokes 532 nm		

Spectrographs cont.

Holospec input accessories

HS-FOI-FC	Holospec FC input adapter
HS-FOI-SMA	Holospec SMA input adapter

Holospec output accessories

HS-FLG-CCD	Holospec spectro CCD flange kit
HS-FLG-CMOUNT	Holospec C-mount flange kit

Software

ANDOR-SDK-CCD	Software Development Kit - CCD and EMCCD
ANDOR-SDK-ICCD	Software Development Kit - ICCD
ANDOR-SR-STANDALONE	Shamrock standalone GUI interface
SOLIS (S)	Solis Spectroscopy Software
SOLIS (SC)	Solis Scanning monochromator Software

Andor Customer Support

Andor products are regularly used in critical applications and we can provide a variety of customer support services to maximise the return on your investment and ensure that your product continues to operate at its optimum performance.

Andor has customer support teams located across North America, Asia and Europe, allowing us to provide local technical assistance and advice. Requests for support can be made at any time by contacting our technical support team at andor.com/support.

Andor offers a variety of support under the following format:

- On-site product specialists can assist you with the installation and commissioning of your chosen product.
- Training services can be provided on-site or remotely via the Internet.
- A testing service to confirm the integrity and optimize the performance of existing equipment in the field is also available on request.

A range of extended warranty packages are available for Andor products, giving you the flexibility to choose one appropriate for your needs. These warranties allow you to obtain additional levels of service and include both on-site and remote support options. Warranties may be purchased on a multi-year basis allowing users to fix their support costs over the operating life cycle of the products.

Head Office
7 Millennium Way
Springvale Business Park
Belfast BT12 7AL
Northern Ireland
Tel: +44 (0)28 9023 7126
Fax: +44 (0)28 9031 0792

North America
425 Sullivan Avenue
Suite 3
South Windsor, CT 06074
USA
Tel: +1 860-290-9211
Fax: +1 860-290-9566

Japan
4F NE Sarugakucho Building
2-7-6 Sarugaku-Cho
Chiyoda-Ku
Tokyo 101-0064
Japan
Tel: +81 (0)3-3518-6488
Fax: +81 (0)3-3518-6489

China
Room 1213, Building B
Luo Ke Time Square
No. 103 Huizhongli
Chaoyang District
Beijing 100101
China
Tel: +86 (0)10-5129-4977
Fax: +86 (0)10-6445-5401

Find us on